ANALYTICAL AND SIMULATION MODELING OF THE TERAHERTZ PHOTOCONDUCTIVE ANTENNAS

A

Thesis submitted

in Partial Fulfilment of the Requirements

for the Degree of

Doctor of Philosophy

by

Jitendra Prajapati

Department of Electronics and Electrical Engineering
Indian Institute of Technology Guwahati
Guwahati - 781039, Assam, India
October 2018


भारतीय प्रौद्योगिकी संस्थान गुवाहाटी
Indian Institute of Technology Guwahati

To

The Memories of My grandparents

स्व. श्रीमती पार्वती देवी & स्व. श्री रामनारायन प्रजापति

स्व. श्रीमती ननकी देवी & स्व. श्री धनीराम प्रजापति

My Parents

श्रीमती शान्ती देवी & श्री जवाहर लाल प्रजापति

and

My Little Gems

गर्वेश & जान्हवी & मिहिर

Certificate

This is to certify that the thesis entitled "**Analytical and Simulation Modeling of the Terahertz Photoconductive Antennas**", submitted by **Jitendra Prajapati** (126102030), a research scholar in the *Department of Electronics and Electrical Engineering, Indian Institute of Technology Guwahati*, for the award of the degree of **Doctor of Philosophy**, is a record of an original research work carried out by him under our supervision and guidance. The thesis has fulfilled all requirements as per the regulations of the institute and in our opinion has reached the standard needed for submission. The results embodied in this thesis have not been submitted to any other University or Institute for the award of any degree or diploma.

Date:
Place: Guwahati

Prof. Ratnajit Bhattacharjee
Dept. of Electronics and Electrical Engg.,
Indian Institute of Technology Guwahati,
Guwahati - 781 039, Assam, India.

Date:
Place: Guwahati

Dr. Amitabh Chatterjee
Former Visiting Assistant Professor,
Dept. of Electronics and Electrical Engg.,
Indian Institute of Technology Guwahati,
Guwahati - 781 039, Assam, India.

भारतीय प्रौद्योगिकी संस्थान गुवाहाटी
Indian Institute of Technology Guwahati

Acknowledgements

First and foremost, I feel it as a great privilege in expressing my deepest and most sincere gratitude to my supervisors Prof. Ratnajit Bhattacharjee and Dr. Amitabh Chatterjee, for their excellent guidance throughout my study. Their kindness, dedication, hard work and attention to detail have been a great inspiration to me. My heartfelt thanks to them for the unlimited support and patience shown to me. I sincerely thank them for the pain they undertook in scrutinizing every manuscript I presented to them and offering critical comments.

I am also very thankful to my doctoral committee members Prof. Anup Kumar Gogoi, Dr. Kshetrimayum Rakhesh Singh, Dr. Ramesh Kumar Sonkar and Dr. Gagan Kumar for sparing their precious time out of their busy schedule to evaluate my progress and enrich this work with their invaluable suggestions and feedbacks.

I would also like to thank the Head of the Department and other faculty members for their kind help in carrying out this work. I am also grateful to all the members of the research and technical staff of the department, specially Mukut sir, Late Mr. Uday Shankar Uzir, and Dasharath sir, without whose help I could not have completed this thesis. My special thanks to Sanjib Das sir for maintaining an excellent computing facility and various resources used for the research work.

Thanks go out to all my lab mates, friends, and seniors, Mrinmoy, Dibyajyoti, Dr. Anand Agrawal, Himangshu, Dr. Kukil Khanikar, Niladri, Darpan, Manoranjan, Rajan, Abhishek, Suman, Dr. Dhiraj Sinha, Satyabrata, Brijesh, Manish, Ashim, Trusna, and Kamakshi. They have always been around to provide useful suggestions, companionship and created a fun-filled research environment. They all contributed directly or indirectly to this thesis, be it academic help, proofreading and volunteering to be a test subject (Guinea pig for Dibyajyoti Das's cooking).

I have no words to express my thanks to some important friends of our morning badminton group especially, Uddipana (Chimp), Ganji, Gargi (Baa), Vivek, Wing Commander Thiyagasundaram, Dr. Charudatt Kadolkar, Dr. M K Bhuyan, and Dr. S K Nayak. They helped me a lot in releasing the work pressure and channelizing it into a positive direction. My work in this place, far away from home, definitely would have been painful without their love and care that helped me to enjoy my life at IIT Guwahati.

My special thanks goes to Dr. Udit Narayan Pal, senior scientist, CSIR-Central Electronics Engineering Research Institute, for his unwavering support and mentorship throughout this research period.

My deepest gratitude goes to my family especially my brother and sister-in-law (Mr. Ghanshyam Prajapati & Mrs. Savita Devi), my sister and brother-in-law (Mrs. Pushpa Devi & Mr. Amit Kumar Prajapati), for supporting me throughout this journey and bearing all the pain that may have ensued due to my prolonged distraction. I am also very grateful to them for letting me free from all the responsibilities throughout my studies. The opportunities that they have given me and their immense sacrifices are the reasons where I am and what I have accomplished so far.

(Jitendra Prajapati)

Abstract

This research deals with the various aspects of the modeling of the Photoconductive Antennas (PCAs). The PCAs are used to radiate the Terahertz (THz) waves. This research work presents the simulation and the theoretical modeling of the PCAs. The simulation studies have been performed using Technology Computer Aided Design (TCAD). For this purpose, Sentaurus from Synopsys has been used. The simulation based modeling of the current pulse in a PCA has been done taking into account the underlying semiconductor device physics as well as the carrier transport dependencies on the different parameters such as the applied electric field, the defect concentrations, and their energy levels.

An improved equivalent electrical circuit model of the PCA working as the THz source has been proposed incorporating the basic semiconductor physics. In this work, a novel approach has been adopted to develop an equation for estimating the capacitance of the PCA. The presented circuit model is capable in predicting the effect of the different physical parameters on the performance of the PCA. The proposed model has been validated by simulation studies and available experimental results. Furthermore, a novel equivalent electrical circuit model of the PCA working as the THz receiver is also proposed. To compute the values of the circuit parameters, the same computation strategies have been adopted as proposed in the PCA source modeling.

This thesis also examines extensively the effect of the radiated near-zone fields on the PCA performance, an issue which was not adequately addressed in the earlier literature. Moreover, this thesis proposes a novel method for improving the radiated

power from a PCA through the use of an external magnetic field. Furthermore, the analytical formulation of the radiated fields relating different PCA parameters is another topic which literature does not address adequately and in this thesis an attempt has been made to bridge this gap with the help of an improved semiconductor carrier dynamics.

Contents

List of Figures

List of Tables

List of Acronyms

PCAs	Photoconductive Antennas
CW	Continuous Wave
THz	Terahertz
BWO	Backward Wave Oscillator
TWTs	Traveling Wave Tubes
RTDs	Resonant Tunneling Diodes
fs	Femtosecond
QCLs	Quantum Cascade Lasers
DFG	Difference Frequency Generation
TCAD	Technology Computer Aided Design
PMAs	Photomixing Antennas
ps	Picosecond
IF	Intermediate Frequency
HEBs	Hot Electron Bolometers
SIS	Superconductor-insulator-Superconductor
LT-GaAs	Low-Temperature grown Gallium Arsenide
FDTD	Finite Difference Time Domain
EO	Electro-Optic
SI	Semi Insulating
SRH	Shockley-Read-Hall

SDE	Sentaurus Device Editor
GUI	Graphical User Interface
SNMESH	Sentaurus Mesh
MBE	Molecular Beam Epitaxy
As	Arsenic
As_{Ga}	Arsenic antisite
As_i	Arsenic Interstitial
V_{Ga}	Gallium Vacancy Point Defect
FDM	Finite Difference Method
LAPCA	Large Aperture Photoconductive Antenna

List of Symbols

$G(t)$	Time varying conductance
V_{sc}	Screening voltage
$P(t)$	Time varying polarization
I	Total circuit current
$\beta(t)V_c(t)$	Time dependent voltage source due to space charge
V_{bias}	Bias voltage
ε	Semiconductor permittivity
n	Electron density
N_D	Ionized donor density
ρ_{trap}	Trap charge density
J_n	Current density due to holes
R_p	Recombination rate of holes
G_p	Holes generation rate
μ_p	Holes mobility
D_p	Diffusion coefficient for holes
E_t	Trap energy level
k_B	Boltzman's constant
τ_n	Electrons lifetime
N_t	Trap density
σ_n	Electron capture cross-section
$V_{Th,n}$	Electron thermal velocity
Z_a	Radiation resistance of Antenna
$Z_p(t)$	Time varying resistance
$C(t)$	Time varying gap Capacitance
$R_s(t)$	Time varying resistance
I_{rad}	Current through radiation resistance
ϕ	Electrostatic potential
q	Electronic charge of electron
p	Hole density
N_A	Ionized acceptors density
J_n	Current density due to electrons
R_n	Recombination rate of electrons
G_n	Electrons generation rate
μ_n	Electrons mobility
D_n	Diffusion coefficient for electrons
$n_{i,eff}$	Intrinsic carrier density
E_{fi}	Intrinsic fermi level
T	Temperature
τ_p	Holes lifetime
E	Electric field
σ_p	Hole capture cross-section
$V_{Th,p}$	Hole thermal velocity

List of Symbols

m_n^*	Effective mass of electrons	m_p^*	Effective mass of holes
C_n	Electrons capture rate	C_p	Holes capture rate
α	Power absorption coefficient	λ	Laser wavelength
K	Extinction coefficient	P_0	Peak optical power
h	Plank's constant	f	Laser frequency
σ_x	Standard deviation in x axis	σ_y	Standard deviation in y axis
σ_t	Time standard deviation	ϕ_{bias}	Applied voltage
n_0	Equilibrium electron density	p_0	Equilibrium hole density
μ_{dop}	Doping dependent mobility	μ_{min}	Minimum mobility
μ_d	Difference in mobility	μ_{elec}	Electric field dependent mobility
μ_{low}	Low field mobility	v_{sat}	Saturation velocity
L	Gap length	W	Gap width
τ_c	Carrier lifetime	v_n	Electrons velocity
v_p	Holes velocity	E_{net}	Net electric field
V_{bias}	Bias voltage	P	Laser average power
τ_l	Laser pulse width	r_l	Laser spot radius
E_{bias}	Bias electric field	P_s	Carriers polarization
V_s	Screening voltage	G_p	Gap conductance
C_p	Gap capacitance	R_s	Dark resistance of substrate
C_s	Gap capacitance in dark condition	R_{sh}	Sheath resistance
C_{sh}	Sheath capacitance	R_p	Plasma resistance
L_p	Plasma inductance	I_d	Dark current
I_A	Current through the gap	I_G	Conductance current
I_c	Capacitance current	V_c	Voltage across capacitance
V_r	Radiation voltage	$n(t)$	Time dependent electron density
$g(t)$	Time dependent generation rate	$P_l(t,r)$	Total power within radius r
ω_0	Laser beam waist radius	η	Quantum efficiency

R	Power reflection coefficient	d	Laser skin depth
ν_{opt}	Laser frequency	$\rho(t)$	Time dependent resistivity
μ_e	Average mobility	n_{av}	Average electron density
$Q(t)$	Change in the charge density	Δt	Time step
$J(t)$	Time dependent current density	τ_r	Carrier recombination time
K	Screening factor	ε_r	Relative permittivity
f_{rep}	Laser repetition frequency	η_e	Optical-to-electrical efficiency
η_m	Matching efficiency	η_r	Electrical-to-THz efficiency
η_t	Total efficiency	P_{THz}	Radiated THz power
G_r	Receiver gap conductance	C_r	Receiver gap capacitance
Z_{in}	Receiver antenna impedance	V_{THz}	Induced THz voltage
V_{gr}	Receiver gap voltage	I_r	Total current in receiver
I_{cr}	Current in receiver capacitance	n_{rav}	Carrier density in receiver
ω_{0r}	Beam waist radius in receiver	W_r	Receiver gap width
L_r	Receiver gap length	μ_{er}	Carrier's mobility in receiver
E_{rnet}	Receiver gap net electric field	r_d	Measurement point distance
J_s	Surface current density	E_{r1}	Near electric field in medium 1
E_{r2}	Near electric field in medium 2	H_{r1}	Near magnetic field in medium 1
H_{r2}	Near magnetic field in medium 2	n_1	Wave direction in medium 1
n_2	Wave direction in medium 2	H	Magnetic field
η_0	Wave impedance in air	$p(t)$	Time dependent total hole density
p_{av}	Average hole density	l_n	Diffusion length of electrons
l_p	Diffusion length of holes	τ_{sn}	Electrons Moment relaxation time
τ_{sp}	Moment relaxation time of holes	H_{ext}	External magnetic field intensity
B_{ext}	External magnetic flux density	v_{nz}	Electrons velocity along z axis
v_{pz}	Holes velocity along z axis	l_{nz}	Distance covered by electrons
l_{pz}	Distance covered by holes a	z_d	Distance along z axis
A	Gap area	ρ_p	Bound charge density

J_p	Polarization current	D	Electric flux density
μ_0	Free space permeability	ε_0	Free space permittivity
E_{far}	Far zone electric field intensity	H_{far}	Far zone magnetic field intensity
y_d	Distance along y axis	H_{THz}	THz magnetic field intensity
ρ	Material density	c_p	Material specific heat capacity
k	Material thermal conductivity	N_{fr}	Density of unfilled traps
N_{fi}	Density of filled traps	m_0	Electron rest mass

List of Publications

Journal Publications

1. **Jitendra Prajapati**, Mrinmoy Bhradwaj, Amitabh Chatterjee and Ratnajit Bhattacharjee, “Radiation Field Analysis of Photoconductive Antenna Using an Improved Carrier Dynamics”, accepted in *Semiconductor Science and Technology*.
2. **Jitendra Prajapati**, Mrinmoy Bhradwaj, Amitabh Chatterjee and Ratnajit Bhattacharjee, “Magnetic Field Assisted Radiation Enhancement from a Large Aperture Photoconductive Antenna”, *IEEE Transactions on Microwave Theory and Techniques*, 66(2), 2018.
3. **Jitendra Prajapati**, Mrinmoy Bhradwaj, Amitabh Chatterjee and Ratnajit Bhattacharjee, “Circuit Modeling and Performance Analysis of Photoconductive Antenna”, *Optics Communications*, 394, 69-79, 2017.
4. **Jitendra Prajapati**, Vinay Kumar boini, Mrinmoy Bharadwaj and Ratnajit Bhattacharjee, “ Comments on “Theoretical Modeling of a Photoconductive Antenna in a Terahertz Pulsed System”, *IEEE Transactions on Antennas and Propagation*, 64(6), 2016.

Conference Publications

1. **Jitendra Prajapati**, Mrinmoy Bhradwaj, Amitabh Chatterjee and Ratnajit Bhattacharjee, “Effect of Near Fields on Radiation from Photoconductive Antenna”, *IEEE MTT-S International Conference on Numerical Electromagnetic and Multiphysics Modeling and Optimization for RF, Microwave, and Terahertz Applications*, Seville, Spain, 2017.

2. **Jitendra Prajapati**, Mrinmoy Bhradwaj, Amitabh Chatterjee and Ratnajit Bhattacharjee, "Equivalent Electrical Circuit Model of Terahertz Photoconductive Antenna Receiver in a Pulsed System", *International Conference on Innovations in Electronics, Signal Processing and Communication (IESC-2017)*, Shillong, India, 2017.
3. **Jitendra Prajapati**, Mrinmoy Bhradwaj, Amitabh Chatterjee and Ratnajit Bhattacharjee, "Time Dependent Capacitance in Photoconductive Antenna", *2015 IEEE Applied Electromagnetics Conference (AEMC)*, Guwahati, India, 2015.
4. **Jitendra Prajapati**, Mrinmoy Bhradwaj, Amitabh Chatterjee and Ratnajit Bhattacharjee, "A Parametric Study of Photo Carrier Generation in Photoconductive Antenna ", *6th International Conference on Computers and Devices for Communication (CODEC)*, Kolkata, India, 2015.

1

Introduction to the Terahertz Waves

Contents

1.1 THz Frequency Spectrum

The THz frequency band is situated between the upper microwave and the lower infrared frequency bands, ranges from 100 GHz to 10 THz having corresponding wavelengths of 3000-30 μm as shown in Fig. 1.1 [1, 2]. It is also known as sub-millimeter, far infrared, and near millimeter waves. Despite being situated between the two developed frequency regions, the THz frequency band was one of the least tapped and underdeveloped frequency region before last few decades. The reason behind this could be attributed to the non-availability of the practical, efficient, and room-temperature operating THz radiation sources. Until recently, the THz waves were used only in the high-resolution spectroscopy and the remote sensing applications [3]. From last few decades, the THz frequency band is receiving a lot of attention due to its unique properties which are suitable for the different applications. Some of the most important properties and related applications of the THz radiation are given as:

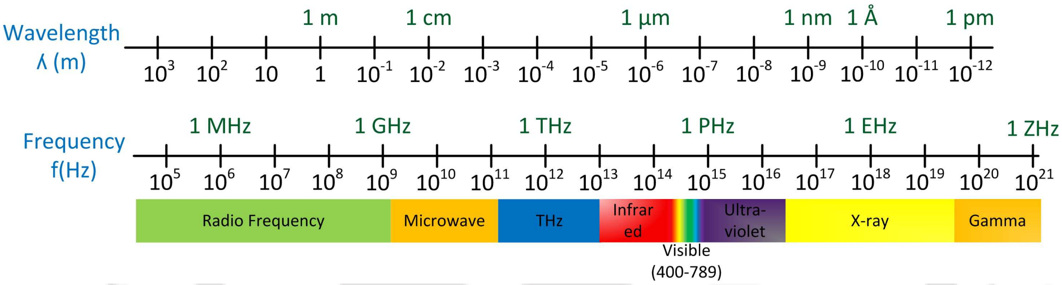

Fig. 1.1: The electromagnetic frequency spectrum

- The wavelengths of the THz radiation are longer than that of visible and infrared radiation. Thus, these are suited for the imaging and the sensing applications [4]. Moreover, most of the dielectric materials such as clothes, paper, wood, and plastic are transparent to the THz radiation [5].
- The low photon energies of the THz frequencies cause THz waves to be of a non-ionizing nature, e.g., at 1 THz, the radiated signal has a photon energy of 4.14 meV. This property is beneficial in the imaging of the biological tissues by THz radiation in contrast to the X-ray radiation [6].
- Many molecules have spectral absorption signatures at the THz frequencies. This prop-

erty of the materials is advantageous in the material spectroscopy using the THz radiation [7].

- The THz radiation is strongly absorbed by the water molecules, which is useful in distinguishing materials with varying water content [8].

1.2 Challenges in the THz Radiation Sources

Although the THz frequency spectrum offers many benefits, challenges remain in developing an efficient and compact THz source. The technologies in the microwave and the infrared frequency bands are well developed and working with high efficiencies, but adopting these techniques for the THz radiation are not feasible without a significant reduction in the power and the efficiency of the devices. The maximum operating frequency of the solid-state electronics based microwave frequency sources depends on the transit time effect of the carriers, the channel length, and the active region size. Scaling these devices for the THz generation will lead to the breakdown of the devices as the channel length decreases which increase the electric field beyond the electrical breakdown of the materials. Similarly, the infrared frequency generation techniques are based on the semiconductor band gap energy. The generation of the THz radiation by down-scaling of these techniques requires a small band gap material which is not feasible at the room temperature [9, 10].

1.3 THz Sources

In the early stage of the research in the THz area, fabrication of the THz sources had been considered very difficult [3]. With the development of the nano-engineering technologies, it became possible to fabricate different types of the THz radiation sources. These sources are either separately based on the microwave and the optical frequency generation techniques or combination of both of the techniques [11]. Several THz radiation sources are commercially available and can be divided into the three broad categories: Electronics sources, Optical sources, and Optoelectronic sources. The electronic sources are purely based on the microwave techniques while the optical sources are based on the optical technologies. The optoelectronic sources use the principle of both of the techniques; the microwave and the optical techniques. In the following subsections, these sources have been discussed in brief.

1.3.1 Electronic Sources

The electronic sources for the THz radiation include vacuum electronic and solid state electronic sources [12]. The working principle of the vacuum electronic sources is based on the interaction between the electron beam and the electromagnetic fields. These sources include backward wave-oscillators (BWOs) [13], extended-interaction klystron [14], gyrotron [15], synchrotrons [16], and travelling wave-tubes (TWTs) [17]. These sources radiate high-power THz waves and the radiated frequency is well below 1 THz [18]. Although these sources can produce high power at the lower THz frequencies compared to the other THz sources, they are usually bulky comparatively and require a strong magnetic field with a very high input power.

The solid state electronic sources include diodes and multipliers. The diodes use the negative differential resistance principle to generate the THz radiation, while the frequency multipliers use a chain of diodes to multiply the frequency to the THz range. The sources include Gunn diodes [19], high frequency transistor [20],frequency multipliers [21], resonant tunneling diodes (RTDs) [22], and IMPATT diodes [23]. However, the output power of these sources decreases at the high frequencies.

1.3.2 Optical Sources

The THz optical sources are divided into the lasers based and the nonlinear crystals based THz sources. The THz lasers have been built using the semiconductor materials such as Germanium and Silicon. These lasers are based on the population inversion under the conditions of the optical pumping of the defects. The main advantage of these type of lasers is the tunability over the wide range of the wavelengths. The THz waves can also be generated by focusing the femtosecond (fs) laser beam on the gas medium generating gas plasma [24, 25] where the radiated frequency depends on the spectral line of the gas. Use of the Quantum Cascade Lasers (QCLs) is another method to generate the THz radiation by using intraband transitions [26]. Moreover, these lasers can be used for the generation of the pulsed as well as the continuous wave THz radiation. The operating frequency of these lasers can be adjusted by changing the design of the quantum well or engineering the bandgap of the materials which facilitates distinct wavelengths generation from the same materials [27].

The THz generation using nonlinear crystals is one of the general methods in which the crystals having a large second-order susceptibility are used to down-convert the optical power of the lasers. The coherent THz waves can also be generated by using the THz parametric processes such as the parametric generation and the difference frequency generation (DFG) [28]. A phase matched THz parametric process can produce widely tunable, coherent and high-power THz waves. To generate a wideband THz radiation from the nonlinear crystals, the optical rectification is one of the most widely used technique [29]. In the optical rectification method, all the possible difference frequencies of spectrally broad pulses are produced. It requires an excitation by the fs laser source, and the output power depends on the optical damage threshold of the material and the degree of the phase matching.

1.3.3 Optoelectronic Sources

The optoelectronic sources are made by combining the microwave and the optical frequency generation techniques. These sources are mainly based on the photo-conductivity principle in the semiconductor materials. An optoelectronic source consist of a voltage biased antenna structure printed on the photoconductive semiconductor material as shown in Fig. 1.2. The fs lasers are used as an excitation source for the antenna structure by generating an ultrafast changing current pulse with the help of the bias voltage. The rapidly changing current pulse excite the antenna to radiate the THz waves. On the basis of the laser excitation, these sources can be divided into two categories:

- Continuous wave (CW) THz source (narrowband): Photomixing Antenna (PMA)
- Pulsed THz source (broadband): Photoconductive Antenna (PCA)

The same system can be used for both of the THz sources: PMA and PCA, with the difference in the number and type of the laser excitation. The PCA system requires a single fs pulsed laser source to generate the THz radiation, whereas the PMA system requires two CW lasers having a slight difference in the operating optical frequency (the difference should be in THz frequency

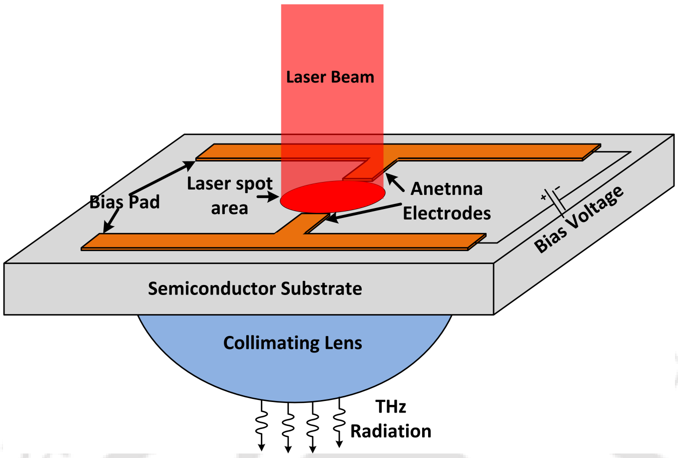

Fig. 1.2: Basic schematic diagram of the optoelectronic system as an emitter

range) [2, 12].

The list of some of the THz sources with their output powers and operating frequencies/bandwidth is presented in Table 1.1.

Table 1.1: List of the THz Sources

THz Source	Power	Frequency	Reference
InP Gunn Diode	45-40 μW	400-425 GHz	[30]
InP IMPATT Diode	27 mW	500 GHz	[31]
GaAs Planar Schottky Diode	40 μW	1.5 THz	[32]
GaAs Diode Mixer	-	2.5 THz	[33]
Schottky Mixer	-	2.5 THz	[34]
GaAs Schottky Diode	$< 10\mu$W	2.7 THz	[35]
GaN IMPATT	200 mW	1 THz	[36]
Resonant Tunneling Diode	<0.5 mW	1.92 THz	[37]
Graphene based FET	-	648 GHz	[38]
InP HEMT	-	1 THz	[39]
BWO	625 mW	617-990 GHz	[40]
Gyrotron	19.2 kW	0.42 THz	[41]
Klystron	60 W	342 GHz	[42]
TWT	20 W	400 GHz	[43]
QCL	100 mW	1-5 THz	[44]
DFG	1.66 μW	0.21-3 THz	[45]
Optical Rectification	0.37 mW	10 THz	[46]
PMA	28-3.5 μW	0.35-1.6 THz	[47]
PCA	300 μW	0.1-5 THz	[48]

1.4 THz Detectors

The technological development in the area of the THz detection was faster than the sources of the THz radiation [3]. Several THz detectors are commercially available, which can measure both the broadband as well as the narrowband signals. The key issue in the detection of the THz radiation is the photon energies in this band of the frequencies, which varies from 0.41 meV to 41 meV and are comparable to the thermal noise energy of 26 meV at the room temperature. Therefore, cryogenic cooling and the long signal integration methods have been adopted for the accurate measurements to overcome the issues due to the background thermal noise.

The THz detectors have been broadly divided into two groups: coherent and incoherent detection techniques [49].

- Coherent THz Detection: can detect the amplitude as well as the phase.
- Incoherent THz Detection: can only detect the amplitude.

1.4.1 Coherent THz Detection

The coherent detection system uses a heterodyne circuit for the detection of the THz frequencies. The incoming THz signals are down-converted to the Intermediate Frequency (IF) signals without losing the phase and the amplitude information. A schematic block diagram of the coherent detection system for detecting the THz signals is shown in Fig. 1.3. The incoming THz signal gets mixed with the local signal using a mixer, generating a copy of the combination of both the signals. The high-frequency signals get filtered out and only IF frequency remains at the output retaining the phase and the amplitude of the incoming signal [49]. The conversion of the THz frequency to IF frequency is known as heterodyne conversion and this method of

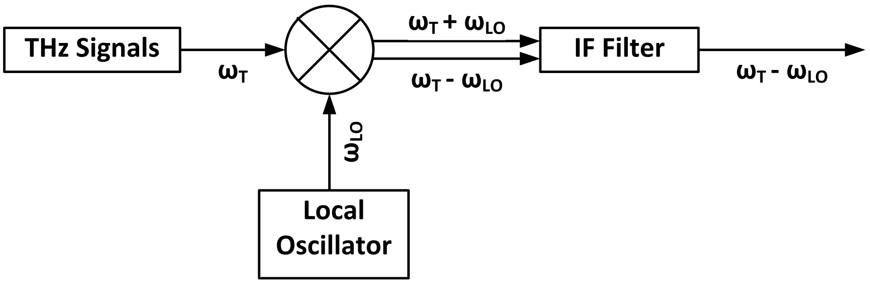

Fig. 1.3: THz coherent detection system block diagram

the detection is also known as the coherent heterodyne detection system. For the mixer, several nonlinear devices are used such as Schottky diodes [50], Tunnel diodes [51], semiconductor and super-conducting Hot Electron Bolometers (HEBs) [52], and superconductor-insulator-superconductor (SIS) tunnel junctions [53]. To increase the sensitivity of the detection systems, heterodyne systems operate at cryogenic temperatures.

1.4.2 Incoherent THz Detection

The incoherent THz detection or direct detection is the broadband signal detection scheme. In this, the incoming signal is focused on the detector by using focusing optics such as lenses and mirrors. An optical filter is employed frequently to remove the unwanted signals other than the detected wavelength. The detected signal is then amplified for further processing [49]. A block diagram of the system is shown in Fig. 1.4. Golay cell, pyroelectric detectors, bolometers are the example of the direct detectors. These detectors can be used at room temperature with an extended response time. Different types of cooled semiconductor detectors such as Se, Ge bolometers, etc., can be employed for the THz detection with a lower response timings.

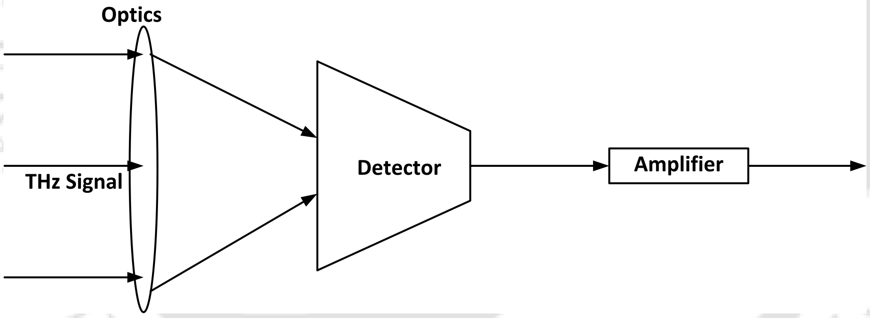

Fig. 1.4: THz direct detection system block diagram

1.4.3 Optoelectronic THz Detectors

The optoelectronic systems; PMAs and PCAs, can also be used to detect the THz signals. These detectors come under coherent THz detector category. The basic schematic diagram of an optoelectronic detector is shown in Fig. 1.5. The main difference between an optoelectronic system working as a source and as a detector lies in the biasing of the electrodes. In the detection system, the antenna is not biased whereas a bias voltage is required in the source system. The

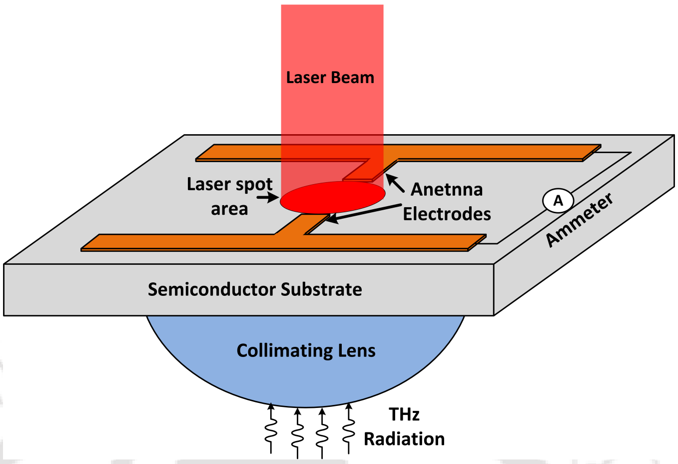

Fig. 1.5: Optoelectronic system as a detector

incoming THz signals create an electric field across the gap region of the antenna electrodes in the optoelectronic detector. The photo-carriers generated through the fs laser get accelerated and induced a photo-current. The generated current then can be analyzed further by taking Fourier transform of it [54].

1.4.4 Free Space Electro-Optic Sampling Technique

This technique of the THz wave detection uses the linear electro-optic (EO) effect also know as the Pockel effect in an EO crystal (nonlinear crystal). The Pockel effect generates birefringence in the nonlinear crystals which is directly proportional to the electric field of the incoming THz signal. The birefringence produces a change in the polarization of the probe beam and by measuring it the amplitude of the THz signals are determined [2, 55]. The block diagram of the system is shown in Fig. 1.6. This type of THz detection comes under the category of the coherent detection.

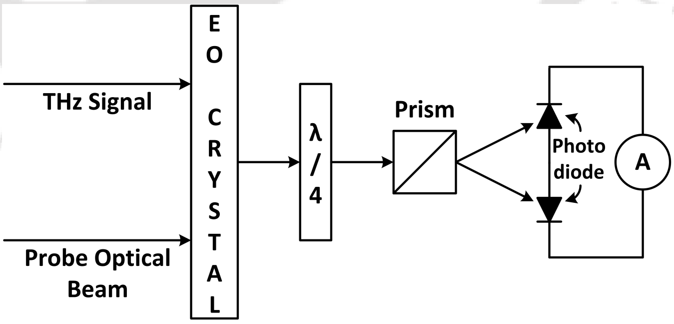

Fig. 1.6: Block diagram of free space EO sampling technique

1.5 Applications of THz Waves

The development of the practical THz sources has attracted interest in the different areas of the applications due to its unique properties which are useful for these areas. Some of the area specific applications of the THz waves are as follows:

1.5.1 Bio-medical Applications

The THz waves are non-ionizing in nature due to the low photon energies. This property is advantageous in analyzing the biological tissues. Also, the THz wave can penetrate up to a few hundred micrometers inside the biological tissues which can be utilized in the imaging and the spectroscopy of the tissues [6]. Since most of the low-frequency bio-molecular motions, such as vibrations and rotations, lies in the THz range of frequencies, therefore various molecules can be recognized and characterized by using their unique spectral responses at the THz frequencies [56]. The THz waves exhibit strong absorption in the water molecules, which can be utilized in the detection of the normal and different types of the cancer cells, as they have the different percentage of the water content [6]. The THz imaging is also used in the dental [6], the digestive system [57], recognizing disease or tumor [58], blood cells analysis [59], and bone analysis [60].

1.5.2 Pharmaceutical Applications

The THz imaging and spectroscopy are beneficial for the pharmaceutical industries. The different medicines/drugs have a unique response or spectral signature at the THz frequencies which can be used in the detection and the characterization of the drugs [61]. The THz imaging and spectroscopy are also useful in the measurement of the coating thickness of medicines, monitoring the coating process [62,63], the measurement of the tablet density and hardness [64], the dissolution profile [65], and the chemical mapping [66] of the medicines.

1.5.3 Security Applications

The wavelengths of the THz radiation are larger than that of the visible and the infrared radiation which makes it very useful for the security applications. The THz waves can penetrate through the materials such as fabrics and plastics, making it useful for the security applications such as scanning, surveillance, and security screening for hidden objects. Moreover, It can also provide the details of the hidden objects such as shape, size, and material used [67].

1.5.4 Polymer Industry Applications

Since the THz radiation can penetrate through the plastic material, it is beneficial for the measurement and the characterization of the polymers. The THz spectroscopy provides the information about the compounding process during the manufacturing of the polymers [68]. The THz systems also provide the quality controlling of the polymers [69]. The physical and the mechanical properties of the polymers strongly depend on the water concentration which is monitored by using the THz spectroscopy.

1.5.5 Communication Applications

As per the needs of the growing applications, the demands of the increased capacity and speed is becoming a huge problem day by day in the present communication systems. The THz communication can provide the solution for these challenges by rendering the massive bandwidth with the high-speed communication band. The atmospheric attenuation of the THz waves is very high due to the presence of the water vapors, so a long distance communication is challenging using the THz waves. Depending on the link characteristics, the THz communication can be used in the femtocells communication, the wireless local area networks in the smart offices, the wireless personal area networks in the smart home systems, the near-field communications such as kiosk downloading, the wireless connections in data centers, and the device-to-device communications [70, 71].

1.6 Working Principle of the THz PCA as an Emitter

The THz photoconductive antenna, sometimes also referred as Auston switch, came into existence in the late 1980s when David Auston [72, 73] and Daniel Grischkowsky [74, 75] with their teams demonstrated the THz waves generated from the co-planar strip lines using the laser beams. The concept of THz waves generation is illustrated in Fig. 1.7. PCA is a photoconductivity principle based THz generation and detection device. A PCA consists a printed antenna

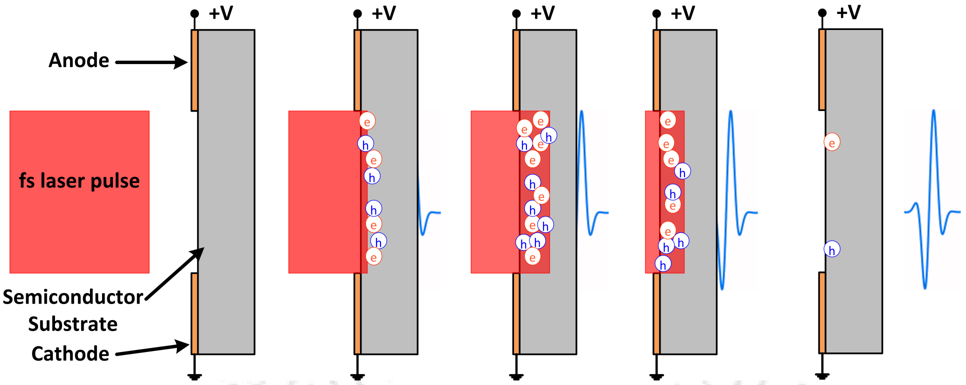

Fig. 1.7: Illustration of the THz generation from the PCA

structure on the photoconductive semiconductor substrate. The metal electrodes are biased with a DC voltage and separated with a gap sometimes referred as the active region or photoconductive gap. A pulsed laser beam is illuminated at the electrodes gap which propagates into

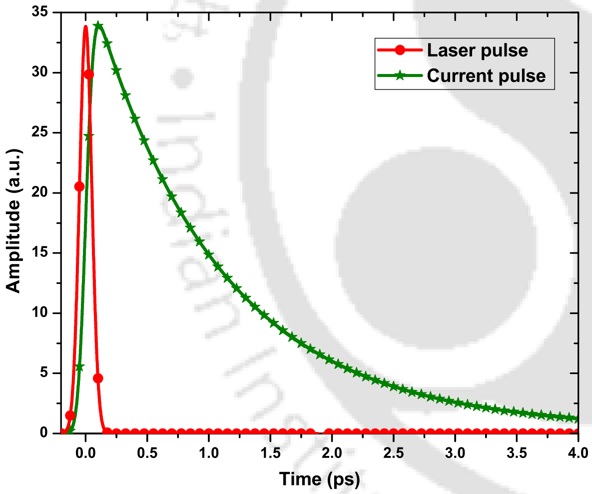

Fig. 1.8: Temporal behavior of the laser pulse and the current pulse

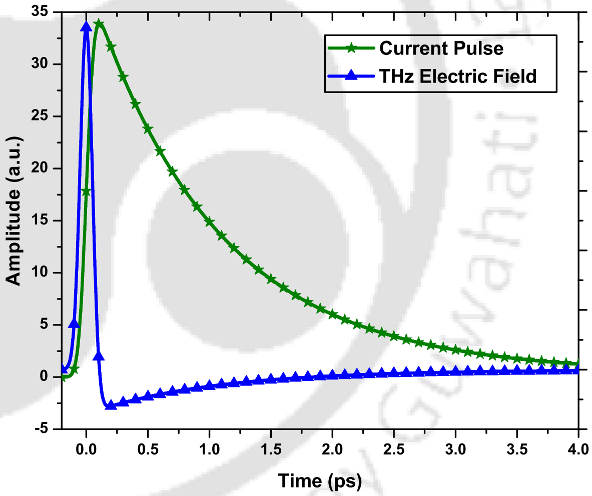

Fig. 1.9: Temporal behavior of the current pulse and the radiated THz electric field

the semiconductor substrate and generates electron-hole pairs. The generated photo-carriers get accelerated towards the respective electrodes by the electric field due to the bias voltage. The transitions in the carrier concentrations and their movement; acceleration and deceleration, produces a transient current pulse which drives the antenna structure to radiate the THz waves. The temporal behaviors of the laser pulse, the current pulse, and the radiated THz electric field are shown in the Figs. 1.8 and 1.9.

The carrier generation rate in the semiconductor material depends on the laser pulse characteristics such as amplitude, rise time, and decay time. The rise time of the current pulse is proportional to same of the laser pulse as shown in Fig. 1.8. While the decay time of the current pulse depends on the different parameters of the semiconductor material, the electric field at the gap, and the antenna geometry.

1.7 Research Motivation and the Problem Formulation

The PCA sources are very popular because of several advantages over other THz sources. These can operate at room temperature, are compact, and can be employed both as the source and the detector. They have several applications in the different areas as mentioned in the section 1.5. These applications require an efficient PCA source with high radiation power. Though several experimental, simulation and theoretical studies have been performed over the PCAs to improve its output characteristics; low efficiency and low output power are the major hurdles in the development of the efficient systems based on the PCAs. The primary motivation behind this study on the PCA is to understand the various issues related to its behavior and to propose an efficient way to enhance its performance.

A proper insight into the effects of the various parameters related to the device plays a crucial role in attempting to improve its performance. As discussed in the previous section, very few theoretical studies have been reported in the literature which can accurately predict the transient behavior of the PCA parameters. Based on the literature, details of which are presented in Chapter 2, following problems have been identified for the further investigation:

- The performance of the PCA mainly depends on the current pulse generated in it which in turn depends on several other parameters related to the semiconductor substrate, the antenna geometry, and the laser source. The reported simulation studies on the PCAs were mainly based on the FDTD method without including the semiconductor physics adequately. Similarly, the reported circuit models of the PCAs have not given due consideration to some of the phenomenon associated with its operation. Therefore, the scope of further investigation and improvement exist in these fronts and the same have been attempted in this thesis.

- There are several factors which limit the efficiency and the radiated power from the PCA. To enhance the efficiency of a PCA, a thorough analysis of these limiting factors is important. So, an analysis is carried out to identify the efficiency limiting factors and different approaches to mitigate their effects is another topic which has been undertaken in this thesis for further investigation.
- Very few studies have been published dealing with the theoretical analysis of the radiated fields from the PCA. The proposed study neglects the effect of the semiconductor substrate on the radiation from the PCAs. So, scopes exist in the improvement of the analytical formulation for the radiated fields from the PCAs with the inclusion of the semiconductor substrate effect.

As a summary, the following are the objectives of this thesis:

(i) To perform a simulation modeling of the current pulse generated in the PCA.

(ii) To develop an improved equivalent electrical circuit model of the PCA by incorporating the physical phenomenon involved in its operation.

(iii) To carry out analysis to identify the factors limiting the radiated power and the efficiency of the PCA.

(iv) To propose a new method for enhancing the efficiency and the radiated power from the PCA.

(v) To derive an analytical expression for the radiated fields from the PCA incorporating the semiconductor substrate effect.

1.8 Thesis Contribution

This thesis has endeavored to provide a circuit models for the PCA working as the source as well as a detector and present the simulation studies considering the different device physics issues involved in the functioning of the PCA. Also the presented theoretical studies helps in the enhancement of the radiation performance of the PCAs. Furthermore, the theoretical study proposed in this thesis helps in calculating the radiated far fields from the PCA. In particular, the following are the main contributions of the work reported in this thesis. This thesis

1. performs the simulation modeling of the current pulse in the PCA using the semiconductor simulation software, Sentaurus TCAD. In the simulation study trap based semiconductor carrier dynamics has been used to evaluate the effect of the different device parameters on the current pulse. The presented study analyzes the effect of the laser power, the laser pulse width, the bias voltage, and the trap density (carrier lifetime) on the generated current pulse in the PCA. It also analyses the effect of the traps energy levels on the current pulse.

2. makes an in depth study of some of the existing circuit models of PCA and proposes an improved equivalent electrical circuit model of it working as the THz source by incorporating the underlying semiconductor physics in its operation. The calculations of the different parameters such as the conductance, the screening voltage, and the polarization have been presented. Also, a novel approach to estimate the transient capacitance has been proposed. Furthermore, the same modeling strategies have also been adopted to propose a novel equivalent electrical circuit model of the PCA working as the THz detector.
3. examines the effect of the radiated near-zone fields on the performance of the large aperture PCA. The proposed theoretical model utilizes the electromagnetic boundary conditions as well as the semiconductor carrier dynamics to assess the effect of the radiated near-zone fields.
4. proposes a novel technique to enhance the efficiency and the radiated power from the large aperture PCA. The proposed method utilizes an external DC magnetic field to improve the radiation performance of the PCA.
5. derives the formulae for the radiated fields from the PCA. It utilizes the electromagnetic relations as well as the effect of the semiconductor substrate material on the radiated fields. Moreover, an improved semiconductor carrier dynamics has been employed to evaluate the radiated fields from the PCA. The proposed carrier dynamics incorporates the transient temperature analysis of the substrate, bandgap narrowing effect due to ultrafast carrier generation, transient carrier lifetimes, transient mobilities, radiated near-zone field effect, and carrier polarization.

1.9 Thesis Overview

A structural organization of the thesis is shown in Fig. 1.10. The organization of this thesis is as follows:

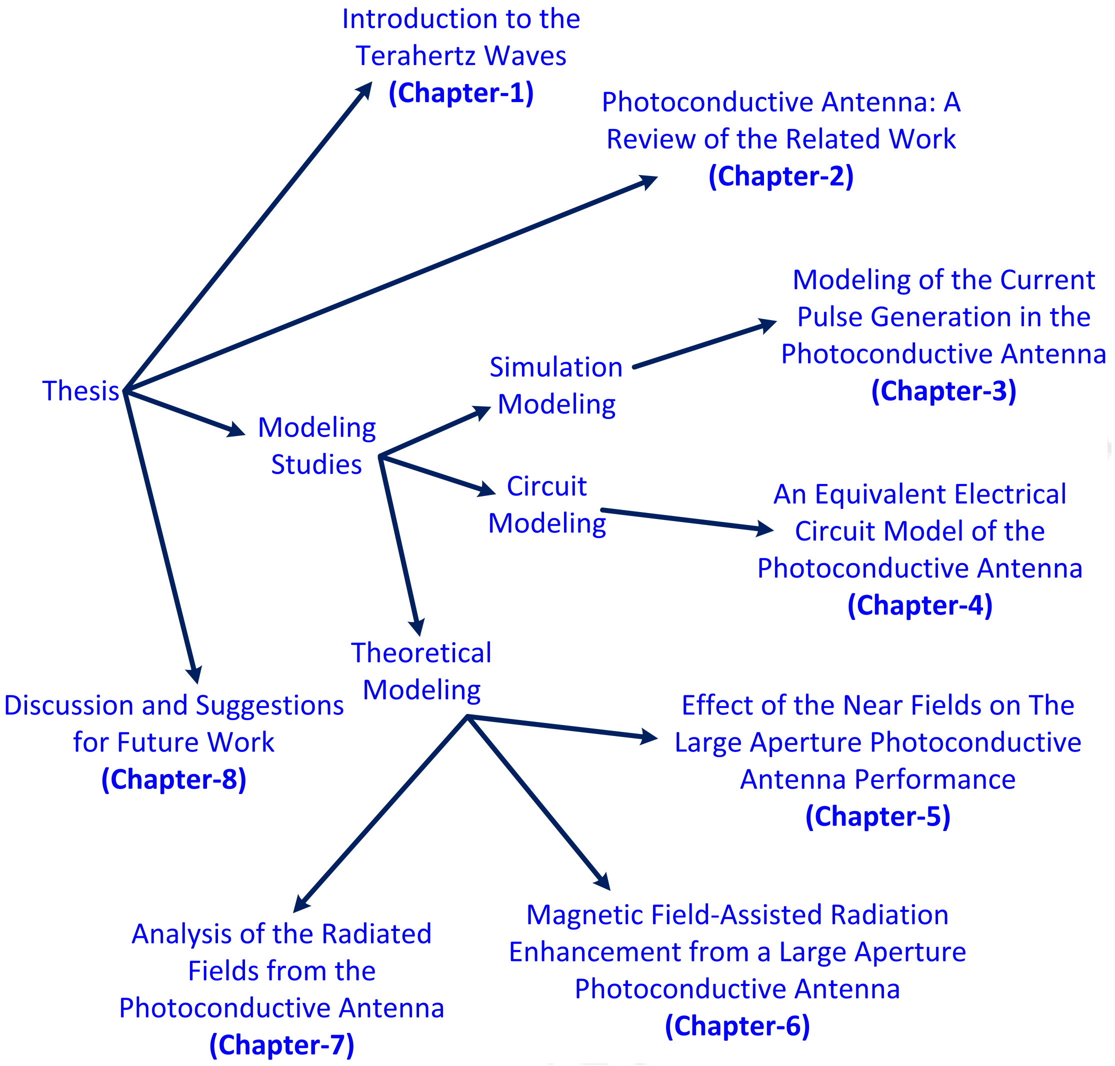

Fig. 1.10: Thesis organization

✍ **Chapter 1** gives a general introduction of the THz waves, sources, detectors and their applications in the different areas. A brief introduction of the working principle of the PCA as a THz source has been presented here. This chapter describes the problem statement and the motivation behind the work. Moreover, it also summarizes the thesis contribution and presents a brief outline of the thesis organization.

- ✍ **Chapter 2** starts with a brief introduction to the main components of the PCA. This chapter discusses the studies reported in the area related to the simulation modeling, the circuit modeling and the performance enhancement studies presented in the literature. Furthermore, It also elaborates the issues related to these studies.
- ✍ **Chapter 3** presents the details of the simulation modeling of the current pulse generated in the PCA. The effect of the gap dimensions, the laser power, and the bias voltage on the current pulse have been examined. Furthermore, the effect of the trap density and their energy levels, variation in the laser spot position and its size on the current pulse behavior have been presented. Effect of different parameters on the current pulse has been summarized
- ✍ **Chapter 4** proposes an improved equivalent electrical circuit model of the PCA working as a source. The calculations of the different parameters of the circuit such as the conductance, voltages, and currents have been discussed. Additionally, a novel approach for the calculation of the transient capacitance has been presented. The effect of the parameters related to substrate material, laser and antenna geometry on the PCA performance have been analyzed. Furthermore, a novel equivalent electrical circuit of the PCA working as the detector have been proposed. The computation strategies proposed for the PCA source have been adopted for the estimation of the different parameters of the receiver circuit model.
- ✍ **Chapter 5** theoretically, analyzes the effect of the near-zone fields on the output characteristics of the large aperture PCA. The transient behavior of the different parameters has been calculated by using the semiconductor carrier dynamics as well as the electromagnetic boundary conditions. A comparative study of the PCA performance with and without the effect of the near-zone fields has been presented.
- ✍ **Chapter 6** proposes a novel method to enhance the radiated power from the large aperture PCA. In this chapter, a theoretical study of the magnetic field assisted efficiency enhancement of the PCA has been proposed. The proposed study uses the electromagnetic boundary conditions as well as the semiconductor carrier dynamics to analyze the

effect of the external magnetic field on the radiated fields.

- **Chapter 7** presents a theoretical study to develop the formulae for the radiated fields from the PCA with the help of the electromagnetic theory and an improved semiconductor carrier dynamics. The effect of the various parameters on the temporal behavior of the radiated fields has been analyzed using the proposed semiconductor carrier dynamics. The proposed carrier dynamics includes the effect of the transient temperature and its effect of the semiconductor material parameters, transient mobilities, transient carrier lifetime, and carrier polarization.
- **Chapter 8** presents the conclusive remark based on the work presented in the previous chapters. All the objectives have been reviewed, and the finding/achievements have been highlighted. Further, the future tracts for extending the research reported in this have been outlined.

2

Photoconductive Antenna: A Review of the Related Work

Contents

2.1 Introduction

In the last few decades, after the introduction of first PCA, tremendous growth in the THz generation using the PCA can be witnessed. Different applications in several areas using the PCA THz source are becoming ubiquitous. The primary requirement of these applications is an efficient THz source having high output power. Several studies have been reported and techniques have been utilized to improve the performance of the PCA but the radiation power and efficiency still remain very small. This leaves scopes for better understating of the physics involved in the operation of a PCA.

Very few studies have been reported in the literature which deals with the analysis of the PCA by using the simulation, the circuit, and the theoretical modeling approaches. This chapter gives a brief review on the main components of the PCA followed by the discussions on the several studies reported in the literature and their limitations.

2.2 Main Components of a PCA

A PCA has three main components; the photoconductive semiconductor substrate, the antenna and the laser source as shown in Fig. 2.1. The details and essential characteristics of these components are discussed as follows:

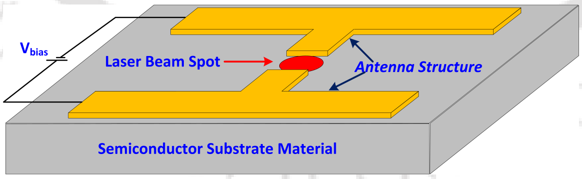

Fig. 2.1: A basic structure of a PCA

2.2.1 Photoconductive Semiconductor Substrate

The photoconductive semiconductor substrate is the central part of a PCA. As there is no material naturally occur which can fulfill the desired properties, several studies have been made to fabricate suitable materials for the PCA. The carriers are generated using the laser illumination on the semiconductor substrate which further produces the current pulse which acts as the excitation source for the antenna printed on it. To support the THz generation from the PCA, the semiconductor substrate material must satisfy some critical requirements. The desirable properties which are required for a semiconductor material to be the used as the substrate in the PCA are as follows:

- **Dark Resistance**: Semiconductor material should have a high value of the dark resistance to limit the dark current in the PCA.
- **Carrier Lifetime**: The carrier lifetime in the semiconductors should be ultra-short (< 1 ps).
- **Carrier Mobility**: The mobility of the carriers should be as high as possible to provide a fast-changing transient pulse.

The intrinsic semiconductor material properties are not suitable for the PCAs, so the different fabrication techniques; implantation, irradiation, and low-temperature-growth, are used to fabricate the photoconductive materials [76–78]. In each of the fabrication methods, the main goal is to reduce the carrier lifetime. This may be achieved by introducing additional energy levels in the bandgap through the different types of defect/trap sites. These trap sites provide an alternate recombination path by trapping the electrons at these intermediate energy levels. Increasing the trap concentrations reduces the lifetime of the carriers which is an essential requirement for the photoconductive material [79]. On the other hand, it also decreases the mobility of the carriers as the scattering of the carriers becomes more frequent due to the reduction of the mean free path [80]. This consequence of increasing trap density in undesirable, thus the primary challenge is to fabricate a material which has ultrashort carrier lifetime, large carrier mobility and very high value of the dark resistance simultaneously. In spite of that, the priority is given to the smaller carrier lifetime by introducing more defects in the semiconductor materials. In order to analyze the THz generation process from the PCAs, many photoconductive semiconductor materials such as silicon on sapphire [81], low-temperature grown Gallium Arsenide (LT-GaAs), Semi-Insulated (SI) GaAs, Implanted GaAs [76, 77], InP [82, 83], InGaAs [78], GaN [84], InGaAsP [85], multi-layered InGaAs-InAlAs [86], and GaAsBi [87] have been used in the experimental studies reported in the literature.

2.2.1.1 Low-Temperature Grown-Gallium Arsenide (LT-GaAs)

LT-GaAs has been used as a substrate material for all the studies presented in this thesis. This section provides brief details about the properties of LT-GaAs relevant to the studies presented in the subsequent chapters.

(i) **Growth of LT-GaAs:** Generally the GaAs material by Molecular Beam Epitaxy (MBE) is grown at a substrate temperature of 600°C [88], whereas, the LT-GaAs film growth varies from the conventional standard through its low growth temperature between 160-300°C [89]. Studies have shown that LT-GaAs is a very non-stoichiometric material, despite it, LT-GaAs can be grown as high-quality mono crystal [90, 91]. During the growth process, excess Arsenic (As) concentration incorporation leads to the formation of a relatively high density of the point defects with density values ranges from 10^{17}-10^{20} cm^{-3} [90]. These point defects include Arsenic antisites (As_{Ga}), Arsenic interstitial (AS_i), and Gallium vacancy(V_{Ga}) [89,90,92]. The amount of excess As is controlled by the substrate temperature during the MBE process and the defect density decreases exponentially with the growth temperature (T_g) in the range of 250-300°C. The excess As concentration can be as high as 2% during the MBE process [89–91]. A high As pressure during the MBE process results in a high As related defect density. Studies show that As rich LT-GaAs possesses a relatively low dark resistivity [93]. The need for a high dark resistivity for the substrate material for the THz sources led to the further treatment of the material following the growth process. In the study [94], it has been found that if the LT-GaAs material goes under the post-growth annealing process at high temperatures (600-800°C) the crystallinity of the epi-layers improves substantially. Also, annealing at high temperatures reduces the structural distortions, hence, relaxes the strain in the lattice induced by the excess As antisites. A material fabrication study presented in [95] found that the annealing process facilitates the As_{Ga} defects diffusion via site exchange with V_{Ga}. At high annealing temperature, more defects in the sample get thermally activated and the diffusion of the defects increases. Thus, samples annealed at high temperatures have comparatively smaller defect densities.

(ii) **Band Structure and Carrier Lifetime of LT-GaAs:** The study presented in [96] show that in the non-annealed samples of LT-GaAs, the As_{Ga} defects act as a double donor. It can be present in a neutral charge state As^{0}_{Ga} and in single positive charge state As^{+}_{Ga}. At the growth temperature (T_g) of 200°C, the concentrations of As^{0}_{Ga} and As^{+}_{Ga} are approximately in the range of 10^{20} cm^{-3} and 10^{19} cm^{-3}, respectively. The As_{Ga} create a partially ionized deep donor level situated at 0.4-0.57 eV below the conduction band edge [97–100] as shown in Fig. 2.2. It is assumed that As^{+}_{Ga} defects act as traps for the electrons since its properties are similar to the EL2 defects which are well known as electron traps. The As^{+}_{Ga} are compensated by the acceptors V_{Ga}. The V_{Ga} are located at the lower half of the bandgap with a lower concentration compared to As^{+}_{Ga} [101] and create a fully ionized deep acceptor level placed 0.3-34 eV above the valence band [102].

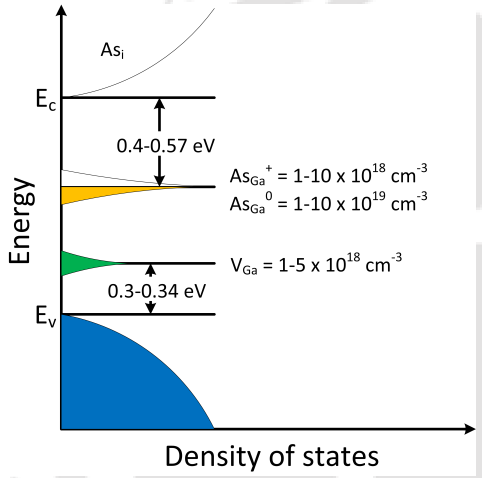

Fig. 2.2: Point defect energies distribution as a function of density of states in non-annealed LT-GaAs [90]

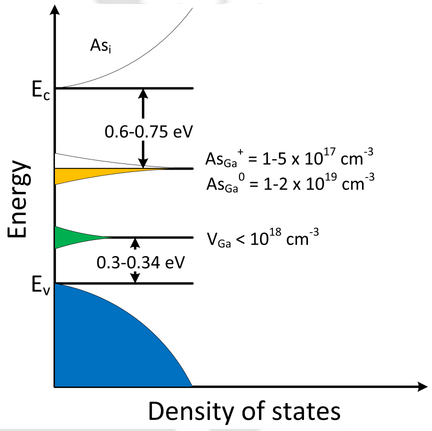

Fig. 2.3: Point defect energies distribution as a function of density of states in annealed LT-GaAs [90]

The annealing process produces a level shift of the deep donors towards the middle of the band gap (roughly around 0.65-0.75 eV) while reducing their concentrations. Studies in [103] and [104] reports a strong dependence of the defect concentration on the annealing temperature. Increasing the annealing temperature from 200-600°C, decreases As^{0}_{Ga} concentration from 3×10^{19} to 10^{18}cm^{-3} and As^{+}_{Ga} from 3×10^{18} to 2×10^{17}cm^{-3} as shown in Fig. 2.3.

A very small carrier lifetime/relaxation time in the LT-GaAs is a favorable characteristic for the THz generation from it. For the first time study reported in [105] investigates the carrier relaxation time and reported a carrier lifetime of 0.4 ps for a material grown at 200°C and annealed at 600°C. In several other studies [79, 105–110] for optimized growth and annealing temperatures, carrier lifetimes between 100-400 fs for the non-annealed and 300-500 fs for the annealed samples have been reported.

(iii) **Electrical Properties of LT-GaAs:** One of the properties that make LT-GaAs a very suitable material for THz sources is its large dark resistivity. LT-GaAs grown at 200°C, without annealing, offers a low resistivity $\rho \sim 10$ Ωcm [98, 111, 112]. Increasing the growth temperature from 200 to 400°C, increases the resistivity from 10 to 10^5 Ωcm [93, 111, 113]. The studies revealed two types of conduction mechanism in LT-GaAs, at temperatures > 300°C the transport is through nearest-neighbour hopping taking place in deep donor band. The second conduction is through the holes excited from the valence band to a nearby neutral donor state.

For LT-GaAs the carrier mobility has been investigated using various methods such as Hall measurements [112], the time-integrated efficiency of photoconductive switches, and THz spectroscopy [108, 114, 115]. For a non-annealed sample, the reported carrier mobility was below 1 $\mathrm{cm^2V^{-1}s^{-1}}$ [98, 112, 116]. At high annealing temperatures, the carrier mobility increases and reaches between 200-400 $\mathrm{cm^2V^{-1}s^{-1}}$. The carrier mobility in LT-GaAs strongly depends on the growth temperatures. The carrier mobility increases from 2000 to 4000 $\mathrm{cm^2V^{-1}s^{-1}}$ when the growth temperature changes from 225 to 350°C [117].

2.2.2 Antenna Geometry

The antenna geometry printed on the semiconductor substrate provides the interface to convert the electrical energy to the electromagnetic radiation energy. The gap size and the electrodes geometry facilitate the collection of the photo-carriers. Several antenna structures with the different gap geometries have been used in the literature to the study the dependence of the PCA behavior on it. Some of the antenna geometries used in the studies are Co-planar stripline [76], Hertzian Dipole [76, 118], Bow-tie Antenna [76, 119], Plasmonic photoconductive grating [120], Comb structure Hertzian dipole [121], and Interdigitated electrode PCA [122] as

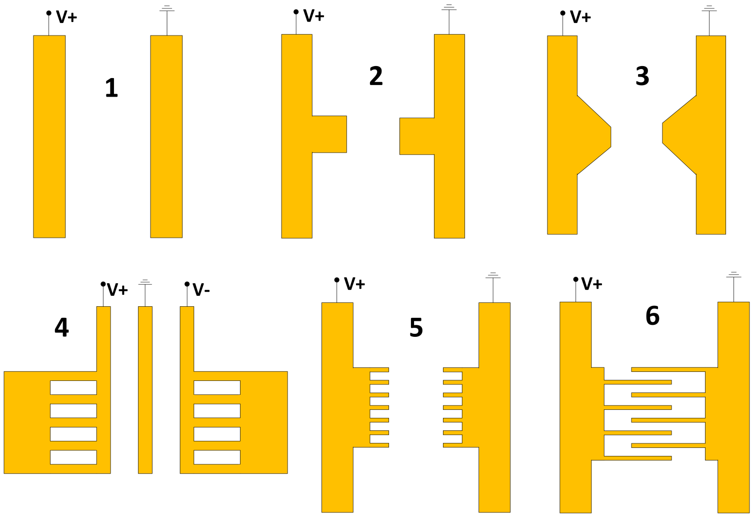

Fig. 2.4: Different PCA Structures 1. Co-planar strip-line 2. Hertzian Dipole 3. Bow-tie Antenna 4. Plasmonic photoconductive grating 5. Comb structure hertzian dipole 6. Interdigitated PCA

shown in Fig. 2.4. In the literature, the PCAs have been divided into three categories based on the gap dimensions: small aperture PCAs (5∼ 50 μm), semi-large aperture PCAs (50∼ 100 μm) and large aperture PCAs (0.1∼ 5 mm) [123].

2.2.3 Laser Source

The THz waves generated from PCAs strongly depend on the laser source. In a PCA, a pulse laser source is used to generate a large bandwidth radiation. The laser power, the wavelength, the pulse width and the pulse repetition frequency define the characteristics of the laser source. The energy of the photon coming from the laser source should be greater than that of the band gap energy of the substrate material to ensure the generation of electron-hole pairs in the material. This implies that the wavelength of the laser source should be carefully decided considering the bandgap of semiconductor material used in the PCA. The pulse width of the source should be as small as possible, preferably less than 100 fs, to support the generation of the ultrafast changing current pulse and to achieve high bandwith radiation. The repetition frequency of the laser source decides the amount of delivered energy into the semiconductor substrate. A high repetition frequency ensures high pulse energy supply to the semiconductor substrate. Several fs laser sources have been used in the literature to study the performance of a PCA, some of them are; femtosecond dye oscillator-amplifier [82], mode-locked Ti:sapphire laser [76], mode-locked laser based on Er-doped fiber oscillator [124], erbium fiber (Er:fiber) laser [78], fiber ring laser [86].

2.3 Literature Survey

The literature survey presented here is carried out for PCA and divided according to studies reported on the simulation modeling, the circuit modeling, the radiated near-zone field effect, the performance enhancement, and the radiated field formulation. The studies reported in the literature considering categories as mentioned above are as follows:

2.3.1 Literature Review of the Simulation Studies

In order to analyze the carrier dynamics in the photoconductive material of PCA, few simulations studies have been reported in the literature. These studies provide a comprehensive knowledge about the transient behavior of the radiation from the PCA and are as follows:

- Hughes *et al.* [125] have applied a three-dimensional FDTD numerical method to analyze the radiation pattern of an H-shaped Hertzian dipole PCA at different radiation frequencies and also computed the transient behavior of the radiated near and far-zone electric fields. The proposed analysis uses the continuity equation to estimate the carrier generation rate which is further used to compute the drift current in the PCA. Although this study reports the behavior of the radiation pattern at different frequencies, non-inclusion of the underlying semiconductor carrier dynamics in the calculation reduces its accuracy.
- Castro *et al.* [126] have presented a semi-classical Monte Carlo simulation study and predicted the effect of the bias voltage and the laser pulse width on the performance of a PCA. The different scattering mechanisms of the carriers in Γ and L valleys, and phonon scattering have been included in the presented semiconductor carrier dynamics. It also calculates the screening effect on the net electric field at the gap due to the carriers accumulation near the electrodes. This study includes transient velocities of the carriers, however, the dependence on the carrier lifetime, the carrier recombination mechanism, the trap density, and their energy levels have not been incorporated in the study.
- Kirawanich *et al.* [127] have presented an FDTD based simulation of PCA having H-

shaped and interdigitated electrode antenna geometries. Simulation includes the drift-diffusion model of carrier dynamics with the field dependent mobilities of the carriers and Shockley Read Hall (SRH) recombination model to account for the carrier recombination. However, the effect of the different scattering mechanism, dependence on the trap density, trap energy levels, the effect of the voltage screening and the carrier polarization have not been included in the presented carrier dynamics.

- Moreno *et al.* [128] have reported a numerical simulation study of the PCA using three-dimensional FDTD including the Drift-Diffusion solver for the semiconductor physics. The authors have included the field dependent mobility of the carriers with the spatial distribution of the doping and the photo-generated carriers in the simulation study. However, no information has been provided about the effect of the voltage screening, carrier polarization, traps densities and their energy levels.
- Emadi *et al.* [129] have presented a hybrid simulation technique by using the semiconductor simulation software Silvaco TCAD along with the electromagnetic simulation software CST Microwave Studio. In this work, the authors have compared the performance of the co-planar stripline, the interdigitated and the comb-shaped PCAs. This study reports the effect of the carrier lifetime, the carrier mobility, and the antenna length on the anode current and radiation bandwidth. However, the presented simulation studies do not include the effect of the trap density and their energy levels on the carrier mobility, the carrier lifetime, and the carrier recombination mechanism.

Although above-reported studies are able to predict the behavior of the different parameters of the PCAs; the accuracy remains a matter of concern. Therefore, a study including the physics, not covered already, is required to analyze the behavior of the PCA and its dependency on the different parameters of the PCA. A summary of the simulation studies discussed in this section is given in Table 2.1.

Table 2.1: Summary of the simulation studies

Reference	Addressed Issues	Unaddressed Issues
Hughes *et al.* [125]	• Photo-carrier densities . • Drift current. • Single carrier based calculations. • Radiated fields calculation.	• Semiconductor carrier transport. • Recombination mechanism. • Voltage screening effect. • Effect of the trap properties.
Castro *et al.* [126]	• Far field approximation. • Drift current. • Effect of carrier scattering. • Voltage screening effect.	• Recombination mechanism. • Transient movement of the carriers. • Carrier lifetime effect. • Effect of the trap properties.
Kirawanich *et al.* [127]	• Photo-generated current density. • Field dependent mobility. • SRH recombination model. • Radiated fields calculation.	• Carrier's scattering effect. • Voltage screening effect. • Effect of the trap properties.
Moreno *et al.* [128]	• Photo-generated current density. • Field dependent mobility. • Recombination mechanism. • Radiated fields calculation.	• Carrier's scattering effect. • Voltage screening effect. • Effect of the trap properties.
Emadi *et al.* [129]	• Laser-semiconductor interaction. • Semiconductor carrier dynamics. • Radiated fields calculation.	• Effect of the trap properties. • Recombination mechanism.

2.3.2 Literature Review of the Circuit Modeling Studies

Analysis of PCA performance by developing its equivalent circuit has been reported in several studies. The details about some of these studies are presented below:

- Loata *et al.* [130] have presented a basic equivalent electrical circuit of the PCA as shown in Fig. 2.5. The gap region between the electrodes is modeled as the series combination of the time-varying resistance ($Z_p(t) = G^{-1}(t)$) and screening voltage (V_{sc}). V_{sc} is calculated from the screening field (E_{sc}) of the carrier polarization ($P(t)$) arising from the separation of the carriers by the net electric field at the gap. In order to reduce the complexity in the calculations, a fixed value of the carrier mobility has been assumed. Although this model can predict the transient behavior of the net electric field, different circuital voltages, and the radiated THz electric field, the accuracy of these results is debatable as this model does not include the effect of the charge accumulation in the gap, effect of the electric field on the carrier mobility, and different other semiconductor physics.

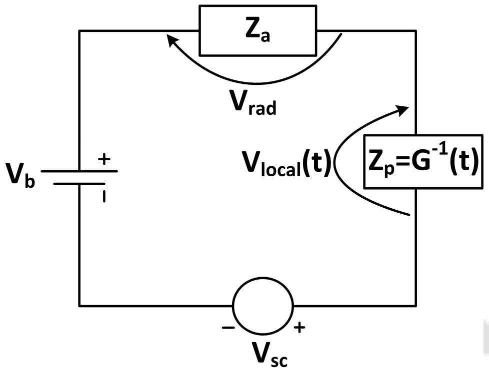

Fig. 2.5: First proposed Electrical Equivalent circuit of the PCA [130]

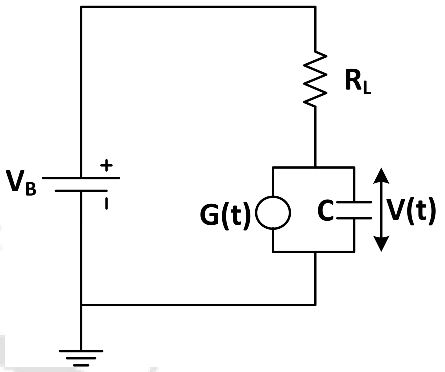

Fig. 2.6: Second proposed Electrical Equivalent circuit of the PCA [131]

- Suen *et al.* [131] have presented a new electrical equivalent circuit model for the PCA by modeling the gap as a parallel combination of the time-varying conductance ($G(t)$) and a static capacitance (C) as shown in Fig. 2.6. However, authors have not provided the details about how the equivalent circuit component values are calculated. Moreover, the presented circuit model does not include the screening effect of the carriers.

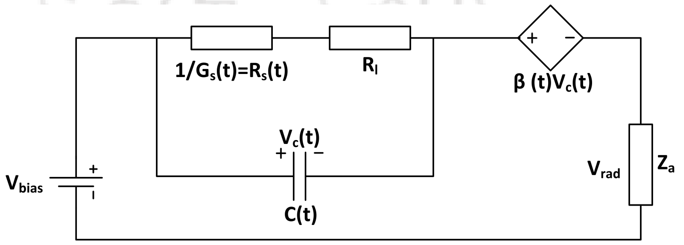

Fig. 2.7: Third proposed Electrical Equivalent circuit of the PCA [132]

- Khiabani *et al.* [132] have presented an equivalent circuit model of PCA by modeling the gap as a series combination of the dependent voltage source ($\beta(t)V_c(t)$) arising due to space charge screening with the parallel combination of the time-varying resistance

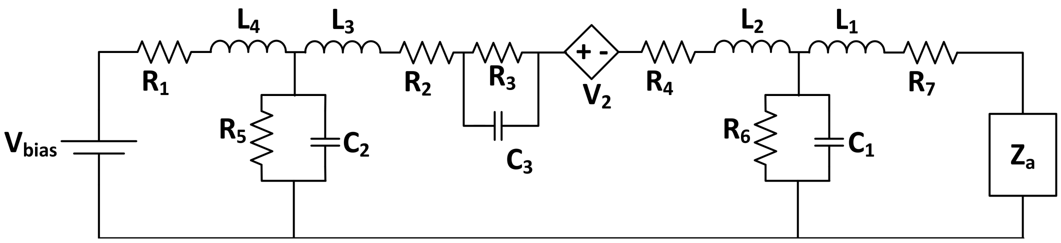

Fig. 2.8: Fourth proposed Electrical Equivalent circuit of the PCA [133]

($R_s(t)$) and the time-varying capacitance ($C(t)$) as shown in Fig. 2.7. The calculation strategies used in this study appear to have several conceptual and numerical issues which are given below:

1. The total circuit current (I) given in (2.1) in [132] as:

$$I(t) = V_c(t)G_s(t) + C(t)\frac{dV_c(t)}{dt} + \frac{dC(t)}{dt}V_c(t) \tag{2.1}$$

should be equal to the current passing through the radiation resistance (I_{rad}) calculated from (2.2) of [132] as:

$$I_{rad} = \frac{V_{rad}}{Z_a} = \frac{e\mu_e n(t)V_c(t)S}{L} \tag{2.2}$$

However, computing it numerically, it has been found that the amplitude of these currents are not equal as shown in Fig. 2.9.

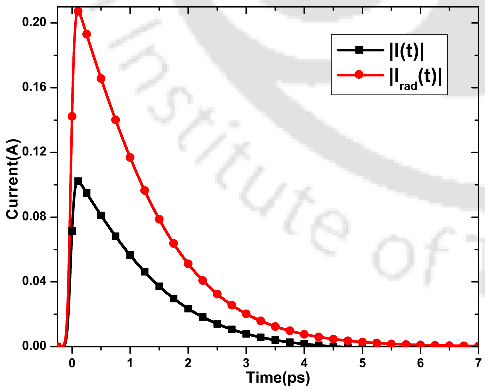

Fig. 2.9: Comparison of the total circuit current at P_{in}=10 mW

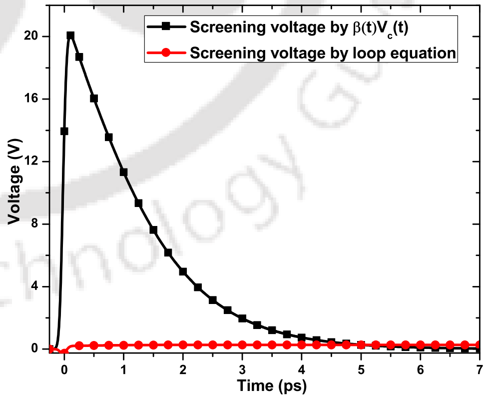

Fig. 2.10: Comparison of the screening voltage at P_{in}=10 mW

2. V_{sc} can be calculated from $\beta(t)V_c(t)$ or from the equation given as:

$$V_{sc}(t) = V_{bias} - V_c(t) - V_{rad}(t) \tag{2.3}$$

Comparing these two values of V_{sc}, a mismatch between them can be observed as shown in Fig. 2.10.

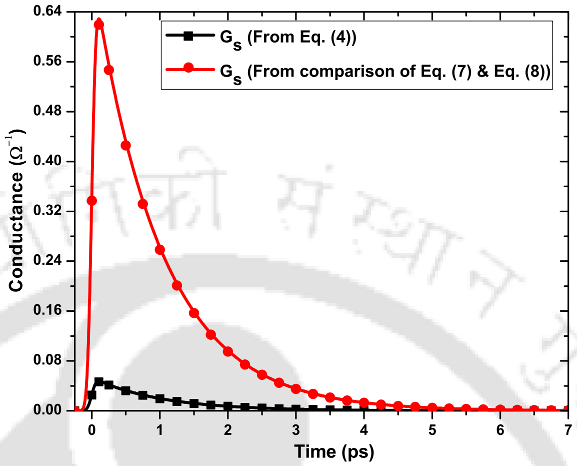

Fig. 2.11: Comparison of the conductance values

3. The value of $C(t)$ and $\beta(t)$ are obtained by equating (7) and (8) [132] term by term, which also gives the value of the conductance. Comparing the conductance value obtained from comparison mentioned above and from (4) [132], a mismatch can be found between the values as shown in Fig. 2.11.

4. Moreover, to calculate the value of the different circuit components, the equation of the circuit presented in Fig. 2.7 is compared with the same of the circuit shown in Fig. 2.5. However, it can be seen from the figures that a direct comparison between these two circuital equations is not valid.

✪ Malhotra *et al.* [133] have proposed an extended circuit model of the PCA by including the bias pads equivalent electrical circuit combining with the circuit model presented in [132]. This study presents the effect of the gap length over the different properties of the PCA. It also presents the simulation study of the antenna radiation pattern using electromagnetic solver HFSS. However, the presented analysis uses the same calculation strategies as presented in [132] and have the same conceptual and numerical issues.

The PCA can also be used as the THz receiver. To analyze its performance as a receiver, the circuit modeling study can be used. However, to the best of the knowledge of the author, no equivalent electrical circuit model has been proposed in the literature for the PCA working as a

THz receiver.

The summary of the circuit modeling studies discussed in this section is given in Table 2.2.

Table 2.2: Summary of the circuit models of the PCA source

Reference	**Physics Incorporated**	**Unaddressed Issues**	**Remarks**
Loata *et al.* [130]	• Carrier generation. • Voltage screening. • Constant mobility.	• Charge accumulation. • Fields and doping dependent mobilities.	• Semiconductor carrier dynamics has not been included adequately.
Suen *et al.* [131]	• Carrier generation. • Constant capacitance.	• Voltage screening.	• No calculation strategy to evaluate the value of the circuit components.
Khiabani *et al.* [132]	• Carrier generation. • Charge accumulation. • Voltage screening.	• Fields and doping dependent mobilities.	• Several conceptual and numerical inconsistencies.
Malhotra *et al.* [133]	• Uses same calculations strategies as in [132] • Antenna losses. • Radiation pattern study.	• Fields and doping dependent mobilities.	• Several conceptual and numerical inconsistencies as in [132].

2.3.3 Literature Review of the Near Fields Effect on the Performance of the PCA

The radiation efficiency and the radiated power from the PCA depend on several factors such as the voltage screening, the mobility reduction due to carrier scattering, and the radiated near-zone fields; which limit its performance. Darrow *et al.* [134] have reported the saturation properties of a large aperture PCA due to the effect of the radiated near-zone fields. Moreover, the proposed study also reported an approximate relation between the near and far-zone electric fields, radiated from the large aperture PCA. However, the reported study does not include the effect of the radiated near-zone fields on the performance of the large aperture PCA. Also, the presented study concentrates mainly on the electromagnetic principles while neglects the effect of the semiconductor material and its parameters in the analysis.

2.3.4 Literature Review of Performance Enhancement Studies

The low output power from the PCA is an issue of concern in the development of the systems based on it. The output power from it depends on the several parameters related to the semiconductor material, the antenna geometry, and the laser source. Various studies have been reported in the literature dealing with the performance analysis and enhancement of the PCA. The radiated power from it can be enhanced by increasing the bias voltage, and the laser power as reported in several studies [135]. In order to improve the radiation characteristics of the PCAs, several other methods have also been employed such as using the different photoconductive semiconductor materials [76, 77, 82, 124], the various antenna geometries [76, 121, 122, 136–138], and by shaping the laser pulse [139, 140] etc. Although studies mentioned above improve the radiated power from the PCA, the improvement achieved still remains quite small.

2.3.5 Literature Review of the Theoretical Analysis of the Radiated Fields

The intensity of the radiated THz electric field can be measured experimentally, or determined through the simulation studies, or calculated analytically. Although the literature is considerably rich in experimental and simulation studies for the radiated fields from the PCA, very limited works are reported on theoretical analysis of radiated fields. To the best of the author's knowledge, only Benicewicz *et al.* [82] have presented an analytical study to derive the formulae for the radiated fields from a PCA. However, the approach presented in [82] uses electromagnetic relations only, while the effect of the semiconductor material, polarization of the carriers, and voltage screening on the radiated fields has not been given due consideration.

2.4 Summary

This chapter summarizes the works reported in the literature associated with the simulation studies, the circuit modeling, the performance enhancement studies, and derivation of the formulae for the radiated fields from the PCAs. Furthermore, the issues related to these studies are emphasized and discussed as well as the requirement of the new research in the respective areas are identified. Moreover, the discussions provided in this chapter also set the primary motivation for the analysis that are carried out in the subsequent chapters.

3

Modeling of the Current Pulse Generation in the Photoconductive Antenna

Contents

3.1 Introduction

Technology Computer Aided Design (TCAD) software provides workbench to investigate the advance device performance. Several commercial software such as Silvaco TCAD, Sentaturus TCAD, Visual TCAD etc., are available for the design and development of the semiconductor devices. The study presented in this chapter uses Sentaurus TCAD to analyze the current pulse generation process in a PCA. The Sentaurus device simulator is a widely used multi-dimensional numerical device simulator designed for the simulation of the electrical, the optical and the thermal characteristics of the Silicon-based devices. However, it is also capable of analyzing the some of the compound semiconductor materials such as GaAs. In the device simulations using Sentaurus TCAD, one can selectively include the numerical model functions.

Prior to this study, all the simulation studies, as reported in section 2.3.1, were mainly based on the basic semiconductor physics where the effects of some of the issues such as the carrier dynamics dependence on the carrier-to-carrier collision, temperature, traps energy level, traps density, as well as the different recombination mechanism are not addressed adequately. Also, these studies have not included the transient changes in the behaviour of the carriers. Based on these drawbacks, the study presented in this chapter tries to incorporate most of the underlying semiconductor physics in the operation of a PCA which were not included in the previously presented studies. This study includes different semiconductor physics such as carrier-to-carrier scattering, transient mobilities, transient velocities, transient carrier lifetime, the effect of the trap density, traps energy level, recombination effect etc.

The total efficiency of a PCA depends on the optical-to-electrical and the electrical-to-THz conversion efficiencies. The primary focus of the presented study in this chapter is to analyze and optimize the optical-to-electrical conversion efficiency. This efficiency mainly depends on the interaction of the laser beam with the photoconductive substrate which results in the formation of a current pulse. This chapter analyses the current pulse generation investigates the effect of various parameters on it using simulation studies in the Sentaurus TCAD. Before discussing the simulation study on the PCA, basic semiconductor carrier dynamics, different physical models, generation-recombination models, and the contact details are outlined in section 3.2.

3.2 Semiconductor Physics

In order to reduce the carrier lifetime in the semiconductor substrate, the trap densities are introduced by the different fabrication techniques. So, to solve the behavior of the PCA, the carrier dynamics must include the effect of the trap densities present in the semiconductor material. In order to analyze the device behavior, the simulation study uses set of equations which are presented in following subsections:

3.2.1 Electrostatic Potential

The solution of the Poisson's equation gives the potential distribution over the solution domain. It is given as [141]:

$$\nabla \cdot \varepsilon \nabla \phi = -q(p - n + N_D - N_A) - \rho_{trap} \tag{3.1}$$

where ϕ is the electrostatic potential, ε is the electrical permittivity of the semiconductor material, q is the elementary electronic charge, n and p are the electrons and the holes densities, N_D and N_A are the densities of the ionized donors and the ionized acceptors, and ρ_{trap} is the charge density contributed by the traps.

3.2.2 Continuity Equation

The time-dependent carrier densities in the substrate material are evaluated by using the continuity equation. The change in the total carriers concentration must be equal to the changes due to the drift, the diffusion, the recombination and the generation processes and is given as [141, 142]:

$$\frac{\partial n}{\partial t} = \frac{1}{q}\nabla \cdot \vec{J}_n - R_n + G_n \tag{3.2}$$

$$\frac{\partial p}{\partial t} = -\frac{1}{q}\nabla \cdot \vec{J}_p - R_p + G_p \tag{3.3}$$

where $\vec{J}_n$ and $\vec{J}_p$ are the current densities due to the electrons and the holes, respectively, R_n and R_p are the net recombination rates of the electrons and the holes, respectively, G_n and G_p are the generation rates of the electrons and the holes, respectively.

The current densities include the drift and the diffusion currents and must satisfy the following equations [141, 142]:

$$\vec{J}_n = q\mu_n n\vec{E} + qD_n\nabla n \tag{3.4}$$

$$\vec{J}_p = q\mu_p p\vec{E} - qD_p\nabla p \tag{3.5}$$

where μ_n and μ_p are the mobilities of the electrons and the holes, respectively, E is the electric field, D_n and D_p are the diffusion coefficients for the electrons and the holes, respectively.

The total current density is given as:

$$\vec{J} = \vec{J}_n + \vec{J}_p \tag{3.6}$$

3.2.3 Recombination Process

The carriers recombination process is an important process in the analysis of the PCA. Several models have been proposed in the literature to model the recombination processes. In the PCA analysis, the Shockley Read Hall (SRH) and the three carriers based Auger recombination models are used to analyze the trap-assisted recombination processes.

3.2.3.1 SRH Recombination Model

The SRH recombination process is shown in Fig. 3.1 and has following sub-processes [143]:

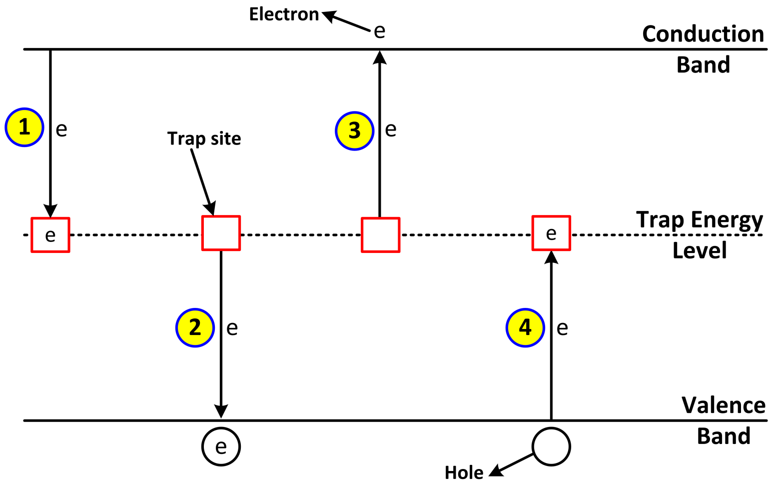

Fig. 3.1: Illustration of SRH recombination process

- **Electron Capture:** An electron from the conduction band is captured by the empty trap at the trap energy level as shown process 1.
- **Hole Capture:** The trapped electron from the trap energy level moves to the valence band and recombines with the holes as shown process 2.
- **Electron Emission:** The trapped electron from the trap energy level moves to the conduction band after gaining energy as shown process 3.
- **Hole Emission:** An electron from the valence band moves to the trap energy level leaving the hole in the valence band as shown process 4.

The net recombination rate in the SRH recombination process is given as [141, 143]:

$$R^{SRH} = \frac{np - n_{i,eff}^2}{\tau_p(n + n_1) + \tau_n(p + p_1)} \tag{3.7}$$

with,

$$n_1 = n_{i,eff} \exp\left(\frac{E_{trap}}{k_B T}\right); \qquad p_1 = n_{i,eff} \exp\left(-\frac{E_{trap}}{k_B T}\right); \qquad E_{trap} = E_t - E_{fi} \tag{3.8}$$

where $n_{i,eff}$ is the intrinsic carrier density, E_t is the trap energy level, E_{fi} is the intrinsic Fermi level, k_B is Boltzmann constant, T is the temperature, τ_n and τ_p are the lifetimes of the electrons and the holes expressed as [141, 144]:

$$\tau_n = \frac{1}{N_t \sigma_n v_{th,n}}; \qquad \tau_p = \frac{1}{N_t \sigma_p v_{th,p}} \tag{3.9}$$

where N_t is the trap density, σ_n and σ_p are the capture cross-sections for the electrons and the holes, respectively, $v_{th,n}$ and $v_{th,p}$ are the thermal velocities of the electrons and the holes, respectively given as; $v_{th,n,p} = \sqrt{\frac{3k_B T}{m^*_{n,p}}}$, and $m^*_{n,p}$ are the effective mass of the electrons and the holes, respectively.

3.2.3.2 Auger Recombination Model

The band to band Auger recombination rate is given as [141]:

$$R^A = \left(C_n n + C_p p\right)\left(np - n_{i,eff}^2\right) \tag{3.10}$$

where C_n and C_p are the capture rates, given as:

$$C_n(T) = \left(A_n + B_n\left(\frac{T}{T_0}\right) + C_n\left(\frac{T}{T_0}\right)^2\right)\left[1 + H_n \exp\left(-\frac{n}{N_{0,n}}\right)\right] \tag{3.11}$$

$$C_p(T) = \left(A_p + B_p\left(\frac{T}{T_0}\right) + C_p\left(\frac{T}{T_0}\right)^2\right)\left[1 + H_p \exp\left(-\frac{p}{N_{0,p}}\right)\right] \tag{3.12}$$

where $T_0 = 300K$ and the values of different constants used for LT-GaAs is given in Table 3.1.

Table 3.1: Coefficients values for the Auger recombination model

Parameter Name	$A(cm^6 s^{-1})$	$B(cm^6 s^{-1})$	$C(cm^6 s^{-1})$	H	$N_0 cm^{-3}$
Electrons	1×10^{-30}	0	0	0	1×10^{13}
Holes	1×10^{-30}	0	0	0	1×10^{13}

3.2.4 Optical Generation

The steady state generation rate of the carriers is given by:

$$G_l(x, y, z, t) = G_0 \times e^{[-\alpha(z-z_0)]} \times e^{\left[-\frac{(x-x_0)^2}{\sigma_x^2} - \frac{(y-y_0)^2}{\sigma_y^2}\right]} \times e^{\left\{\frac{\left[t - t_0 - (z-z_0)\sqrt{\varepsilon}/c\right]^2}{\sigma_t^2}\right\}} \tag{3.13}$$

with

$$G_0 = \frac{\alpha P_0}{hf}; \qquad \alpha = \frac{4\pi k}{\lambda} \tag{3.14}$$

where P_0 is the peak optical power, h is Plank's constant, f is the laser frequency, σ_x and σ_y are the spot size standard deviations, σ_t is the time standard deviation, λ is the laser wavelength, and k is the extinction coefficient.

3.2.5 Metal-Semiconductor Interface

The ohmic contacts are used at the metal-semiconductor interface. The Dirichlet boundary conditions are applied at the ohmic contacts and given as [141]:

$$\phi = \phi_{bias} + \frac{kT}{q} asinh\left(\frac{N_D - N_A}{2n_{i,eff}}\right) \tag{3.15}$$

$$n_0 = \sqrt{\left(\frac{N_D - N_A}{2}\right)^2 + n_{i,eff}^2} + \left(\frac{N_D - N_A}{2}\right)^2 \tag{3.16}$$

$$p_0 = \sqrt{\left(\frac{N_D - N_A}{2}\right)^2 + n_{i,eff}^2} - \left(\frac{N_D - N_A}{2}\right)^2 \tag{3.17}$$

where ϕ_{bias} is the applied voltage, n_0 and p_0 are the electrons and the holes equilibrium concentrations.

3.2.6 Mobility Models

The mobility models are originated from the moment relaxation time of the carriers in the lattice. Therefore, the mobilities of the carriers depend on various scattering mechanisms such as the lattice scattering, the carrier-to-carrier scattering, and the defect scattering. It also depends on the energy of the carriers, the impurities concentrations, and the lattice defects [145]. In the analysis of the PCA, the doping and the field dependent mobility models have been utilized to study the characteristics of the generated current pulse.

3.2.6.1 Arora Mobility Model

The doping dependency of the carrier mobility is modeled by using the Arora mobility model, which is given as [141, 146]:

$$\mu_{dop} = \mu_{min} + \frac{\mu_d}{1 + \left(\frac{N_A + N_D}{N_0}\right)^{A^*}} \tag{3.18}$$

$$\mu_{min} = A_{min}\left(\frac{T}{300}\right)^{\alpha_m}; \qquad \mu_d = A_d\left(\frac{T}{300}\right)^{\alpha_d} \tag{3.19}$$

$$N_0 = A_N\left(\frac{T}{300}\right)^{\alpha_N}; \qquad A^* = A_a\left(\frac{T}{300}\right)^{\alpha_a} \tag{3.20}$$

The values of the different parameters of LT-GaAs material used in the simulation study is provided in Table 3.2.

Table 3.2: Coefficients values of the Arora mobility model for LT-GaAs

Parameter Name	A_{min} $(cm^2V^{-1}s^{-1})$	α_m	A_d $(cm^2V^{-1}s^{-1})$	α_d	A_N (cm^{-3})	α_N	A_a	α_a
Electrons	200	-0.7457	8300	-2.687	10^{14}	3.535	0.6273	-0.1441
Holes	40	-1.124	360	-2.366	10^{15}	3.69	0.8057	0

3.2.6.2 Caughey-Thomas Mobility Model

The field dependency of the carrier mobility is modeled by the Caughey-Thomas model and is given as [141, 145]:

$$\mu_{elec,n} = \mu_{low,n}\left[1+\left(\frac{\mu_{low,n}E}{v_{sat,n}}\right)^2\right]^{-1/2} \tag{3.21}$$

$$\mu_{elec,p} = \mu_{low,p}\left[1+\left(\frac{\mu_{low,p}E}{v_{sat,p}}\right)^2\right]^{-1/2} \tag{3.22}$$

where $\mu_{low,n}$ and $\mu_{low,p}$ are the low field mobilities of the electrons and the holes, respectively, $v_{sat,n}$ and $v_{sat,p}$ are the saturation velocities of the electrons and the holes, respectively, and E is the applied electric field.

3.3 Simulation Steps in Sentaurus TCAD

The simulation study in the Sentaurus TCAD involves several steps and modules. A brief introduction of these modules are as follows:

- **Step 1 (Sentaurus Device Editor):** The Sentaurus Device Editor (SDE) is used to create the PCA geometry. The geometries can be created in 1-D, 2-D, and 3-D by using a user-defined script or by using the graphical user interface (GUI). The region-wise material definitions, the doping profiles, the electrical contacts, and the meshing criterion are defined in it.
- **Step 2 (Sentaurus Mesh):** The Sentaurus Mesh (SNMESH) uses the file generated from the SDE and generate the TDR grid and data files for device simulation. The output files contain the material identifiers and doping information at each node of the mesh.
- **Step 3 (Sdevice):** The Sdevice module solves the device using numerical methods and models as defined in the user-defined script. The user-defined script contains the different device physics, models, parameter files, and parameters descriptions to be calculated.

3.4 LT-GaAs Material Characteristics

LT-GaAs is the most widely used material for the THz generation from the PCA. A high-quality GaAs is grown by the Molecular Beam Epitaxy (MBE) at different low growth temperatures ($200-300°C$) and annealed at high temperatures ($400-600°C$). However, after annealing at higher temperatures, GaAs becomes highly resistive. Because of low growth temperature, LT-GaAs is highly non-stoichiometric and the excess concentration of Arsenic (As) creates a high concentration of As related deep level defects. The arsenic concentration depends on the growth temperature and As pressure during the material deposition. The excess As generates several point defects in GaAs such as arsenic antisites (As_{Ga}), arsenic interstitials (As_i), Gallium vacancy point defects (V_{Ga}), etc. Depending on the growth temperature, the defects densities varies from 10^{17} – 10^{20} cm^{-3}. The concentration of the ionized donor As^{+} are responsible for the fast trapping of the electrons. Increasing the defect densities in GaAs decreases the lifetime of the carriers as well as their mobilities. A high-temperature post-growth annealing increases the mobilities of the carriers by decreasing the defect concentrations. Due to the high defect concentration, the carrier lifetime comes down to few ps. For example, at growth temperature $200°C$ and annealing at $600°C$, the carrier mobility and carrier lifetime in LT-GaAs is measured to be 120 – $150 cm^{2}V^{-1}s^{-1}$ and 0.4 ps, respectively [90, 105, 106, 108, 109].

3.5 Simulation Setup in the Sentaurus TCAD

A 3-D simulation of the PCA is performed in the Sentaurus TCAD. As the current generation mainly depends on the carrier dynamics in the gap region between the electrodes, only the gap region has been considered in the simulation studies. A typical structure of the PCA geometry used in the simulations is shown in Fig. 3.2. The length and the width of the gap region are

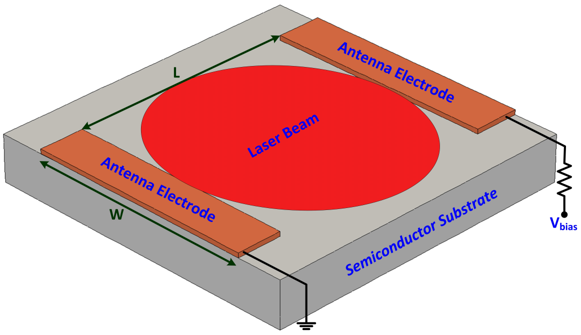

Fig. 3.2: Simulation geometry of PCA

shown by L and W, respectively. The resistance connected to one of the electrodes represents the radiation resistance of the antenna structure which accounts for the power loss due to the radiation from the PCA. A voltage bias is applied to the same electrode while the other electrode is connected to the ground. LT-GaAs for the semiconductor substrate and Copper for the electrodes are used in the simulation studies. The LT-GaAs material is not available in the Sentaurus TCAD material library, so the GaAs material properties have been modified according to the information available in the literature of the LT-GaAs. For example, to achieve the short carrier lifetime, GaAs is uniformly doped with the different doping concentrations such as As^{+}, V_{Ga}, and As_i. The trap-assisted recombination mechanism of the carriers plays a major role in reducing the carrier lifetime. In the simulation study, a carrier lifetime (τ_c) of $\approx$ 1 ps and $\approx$ 9 ps have been obtained for the As^{+} doping concentrations of 5×10^{19} cm^{-3} and 1×10^{19} cm^{-3}, respectively, while keeping the doping densities of V_{Ga}, and As_i in the range of 10^{18} cm^{-3}. The traps are placed near to the mid-energy level of GaAs material. The generation of the carriers by the laser illumination is solved using the ray tracing optical solver. The simulation flow of the PCA in the Sentaurus TCAD is shown in Fig. 3.3. Several geometries such as conventional dipole, interdigitated, and comb structured electrodes with the different antenna gap lengths and widths have been analyzed to understand the effect of the various parameters on the generated current pulse. In the simulation studies, the gap geometries L = 10 μm, W = 10 μm with the laser spot radius of 5 μm and $L = 5$ μm, W = 5 μm with the laser radius of 3 μm have been used to obtain the current pulse behavior.

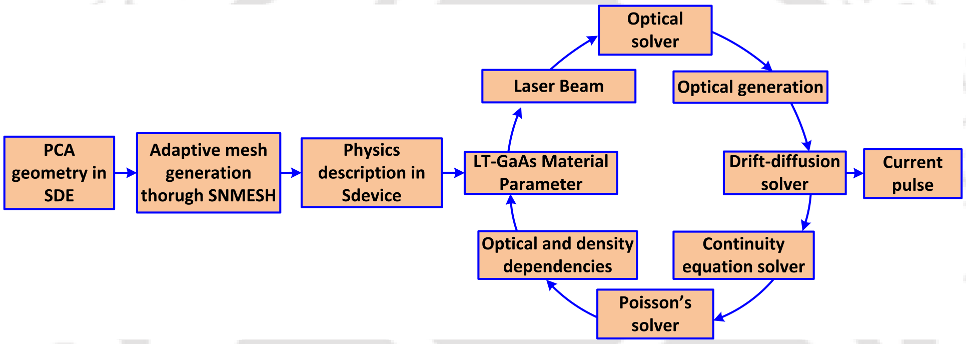

Fig. 3.3: Simulation flow for the PCA in Sentaurus TCAD

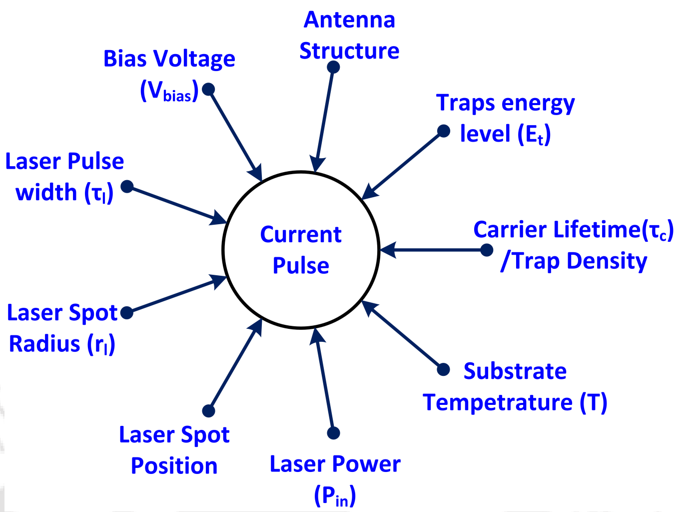

Fig. 3.4: Parameters affecting the behavior of the current pulse generated in the PCA

3.6 Results and Discussions

In the simulation study of the PCA the effect of several parameters, as shown in Fig. 3.4, on the generated current pulse, have been analyzed and discussed in the following subsections:

3.6.1 Effect of the Bias Voltage

The applied bias voltage at the electrodes set up an electric field across the gap region which facilitates the movement of the carriers towards the respective electrodes (the electrons towards the anode and the holes towards the cathode). The carrier velocities strongly depend on the electric field and are related as:

$$v_{n,p} = \mu_{n,p} E_{net} \tag{3.23}$$

where E_{net} is the net electric field at the point of calculation in the simulation domain.

The net electric field at the gap varies with the bias voltage. Increasing the bias voltage increases the net electric field, which results in a high amplitude current pulse due to the large number of the carriers collection at the electrodes. The same behavior can be observed in Fig. 3.5.

3.6.2 Effect of the Laser Power

The role of the laser source is to generate the electron-hole pairs in the semiconductor substrate material which will further form a current pulse with the help of bias voltage. The photo-

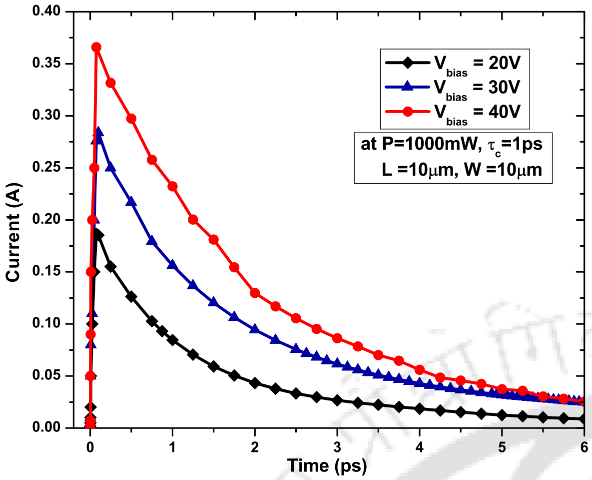

Fig. 3.5: Effect of the bias voltage on the current pulse

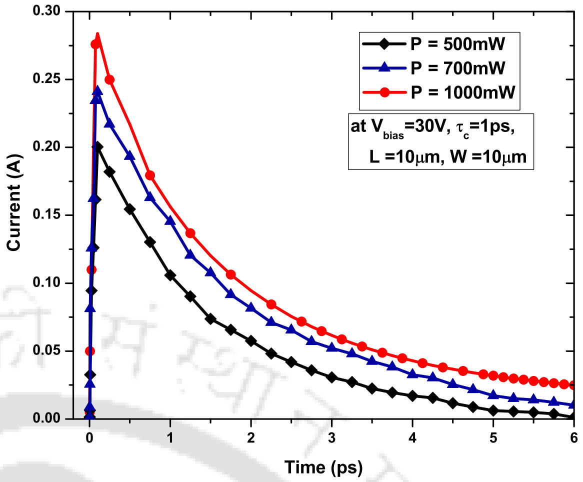

Fig. 3.6: Effect of the laser power on the current pulse

generated carrier density depends on the laser beam power (P). Increasing the laser power increases the the photo-carriers in the gap region as well as the collected carriers at the electrodes resulting in a high amplitude current pulse generation. The same behavior can be seen in Fig. 3.6.

3.6.3 Effect of the Laser Pulse Width

The peak power of a laser beam and the laser pulse width (τ_l) are inversely proportional. The photo-generated carriers decrease with an increase in the laser pulse width due to reduced laser peak power. As the densities of the photo-generated carriers at the gap decline, the amplitude of the current pulse also falls off as shown in Fig. 3.7.

3.6.4 Effect of the Laser Spot Radius

The change in the laser spot radius (r_l), while keeping the laser power constant, changes the amplitude of the generated current pulse. The generation of the photo-carriers is centered in and around the laser spot position. If the distance between the generation point and the nearby electrode is considerable large and the transit time of the carriers to reach the electrode is greater than its lifetime, less number of the carriers get collected at the electrode due to the recombination of the carriers with the traps/defects before reaching the electrode. The similar behavior of the laser spot radius effect on the current pulse is shown in Fig. 3.8, while keeping the laser focused at the center of the gap region.

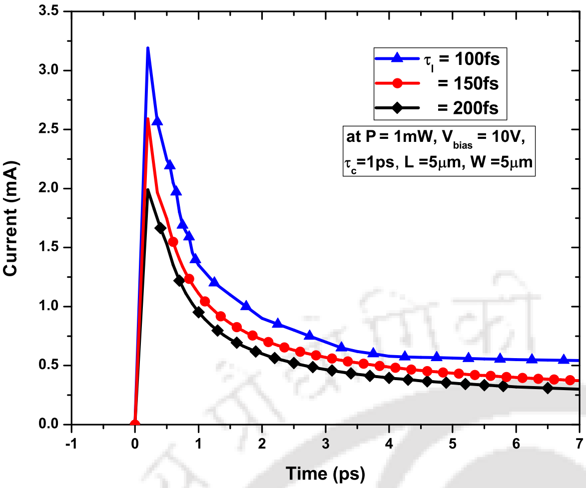

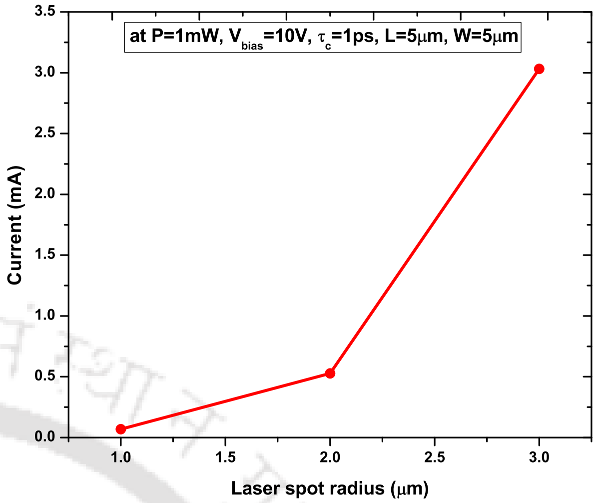

Fig. 3.7: Effect of the laser pulse width on the current pulse

Fig. 3.8: Effect of the laser spot radius on the current pulse

3.6.5 Effect of the Laser Spot Position

The laser beam spot position is also an important parameter in deciding the behavior of the current pulse. A stiff focusing of the laser beam near the anode facilitates a high amplitude current pulse as a large number of the carriers get collected at the electrode in a very small duration. While moving the laser spot away from the anode decreases the amplitude of the current pulse because of the fewer carriers collection at the electrode. The same dependency of the current pulse amplitude on the laser spot position is shown in Fig. 3.9.

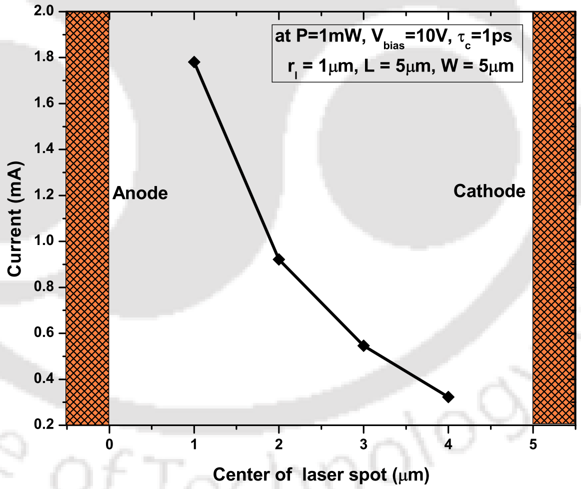

Fig. 3.9: Effect of the laser spot position on the current pulse

3.6.6 Effect of the Antenna Geometry

The carrier velocities depend on the electric field distribution at the gap region. The amplitude of the electric field depends on the bias voltage applied to the electrodes. while the distribution profile of the voltage depends on the electrodes structure in the gap region. Changing the electrodes geometry changes the voltage distribution in the gap as shown in Figs. 3.10, 3.11 and 3.12.

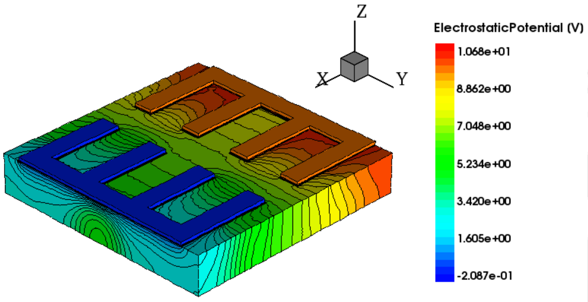

Fig. 3.10: Voltage distribution profile in the comb structured PCA

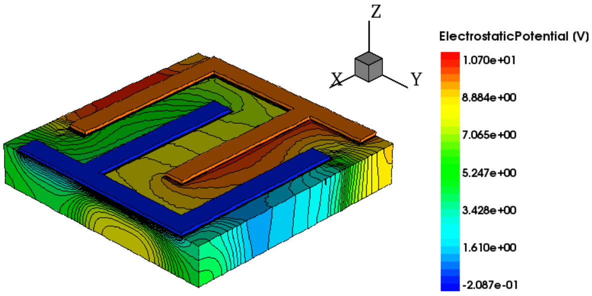

Fig. 3.11: Voltage distribution profile in the interdigitated structured PCA

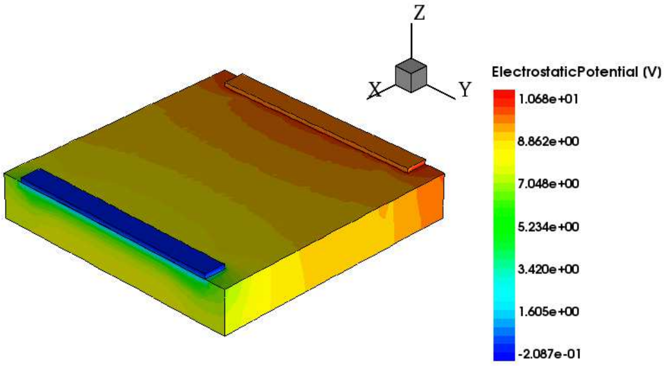

Fig. 3.12: Voltage distribution profile in the Hertzian dipole PCA

The change in the voltage distribution profile at the gap alter the carrier's movement which in turn affect the current pulse characteristics. To show the effect of the antenna geometry on the current pulse, the hertzian dipole, the comb, and the interdigitated electrode structured PCAs as shown in Fig. 3.13 and 3.14, respectively, are used in the simulation study. The simulation studies are performed for the different values of g for both geometries; comb and interdigitated structured PCAs, where g is the shortest distance between the anode and the cathode. The

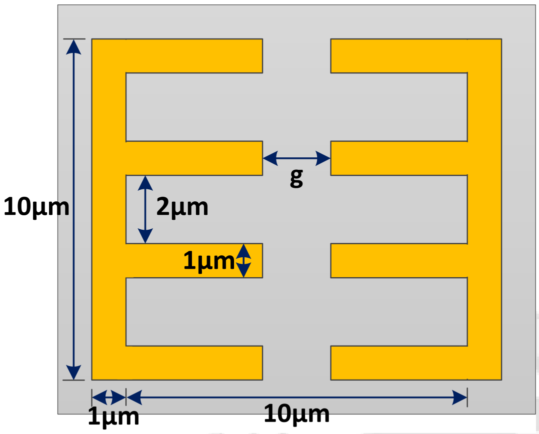

Fig. 3.13: Comb structured PCA gap

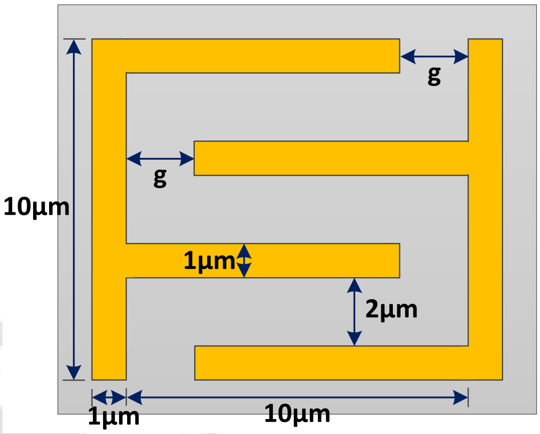

Fig. 3.14: Interdigitated structured PCA gap

effect of g on the current pulse is shown in Fig. 3.15 and 3.16. Increasing the value of g decreases the net electric field at the gap which affects the carrier velocities and results in a low amplitude current pulse. The reduction in the amplitude of the current pulse for $g = 1\mu m$ in the interdigitated electrodes may be attributed to the dominating voltage screening effect due to the charge accumulation near the electrodes. However, for the large values of g, the voltage screening does not affect much and the large gap between electrodes decreases the net electric field which results in a small current amplitude.

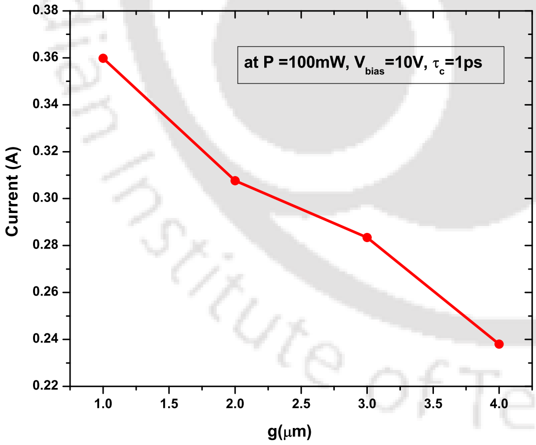

Fig. 3.15: Peak amplitude of the current pulse in the comb structured PCA

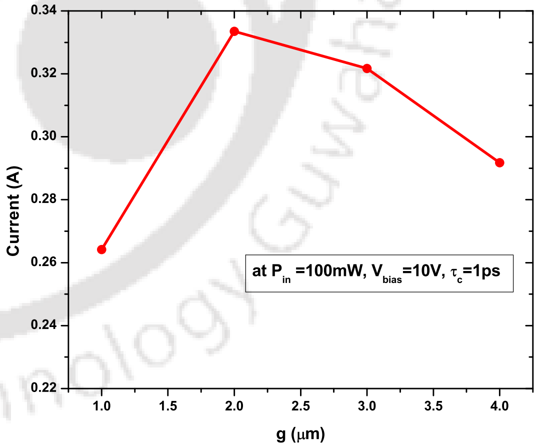

Fig. 3.16: Peak amplitude of the current pulse in the interdigitated structured PCA

3.6.7 Effect of the Carrier Lifetime

The carrier lifetime mainly depends on the concentration of the traps (defects), carrier's capture cross-section at the given energy level in the semiconductor material and are related as given in (3.9). Increasing the concentration of the traps decreases the carrier lifetime. A large carrier lifetime provides extended time to the carriers to be remain in the gap region or get collected by the electrodes before recombining with the trap sites. Whereas, in case of short carrier lifetime, the probability of the recombination with the trap sites is very high and a large number of the carriers recombine before getting collected at the electrodes. So, increasing the carrier lifetime increases the number of carriers collected by the electrodes and results in a large amplitude current pulse, however, it also increases the width of the current pulse. The same behavior of the carrier lifetime effect on the current pulse can be seen in Fig. 3.17.

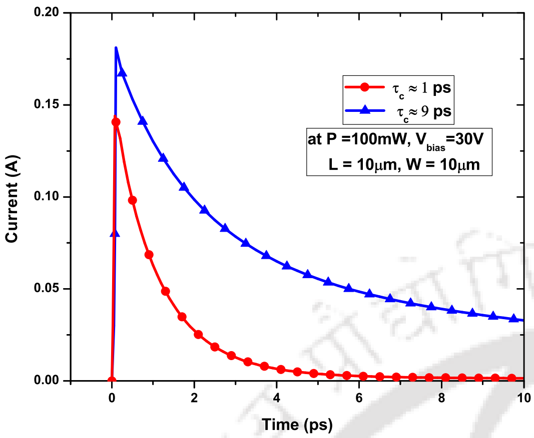

Fig. 3.17: Effect of the carrier lifetime on the current pulse

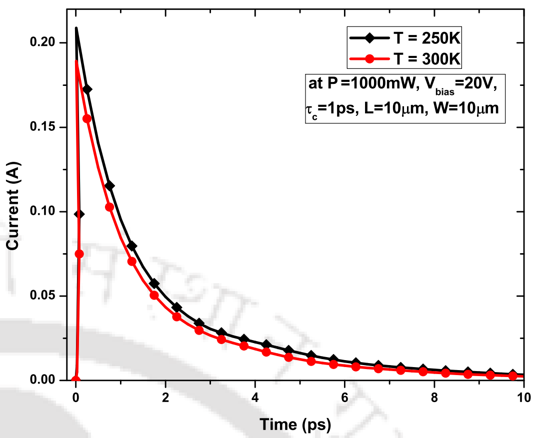

Fig. 3.18: Effect of the temperature on the current pulse

3.6.8 Effect of the Substrate Temperature

The different parameters such as the carrier mobility, the carrier lifetime, and the carrier recombination rates in the semiconductor substrate are temperature (T) dependent. The change in the substrate temperature changes the value of these parameters, thereby, modifying the current pulse characteristics. There can be several reasons behind the substrate temperature change such as the laser power dissipation, the power loss due to substrate resistance, and the carrier-to-carrier collisions. The effect of the substrate temperature on the current pulse is shown in the Fig. 3.18.

3.6.9 Effect of the Energy Level of the Traps

The energy level of the traps can be controlled by different ways such as by varying the annealing temperature, controlling pressure coefficient, etc. [147–149]. To analyze the effect of the energy level on the current pulse, traps have been placed at the different energy levels and the current pulse behavior is analyzed. The peak value of the current pulse at different energy level is plotted in Fig. 3.19.

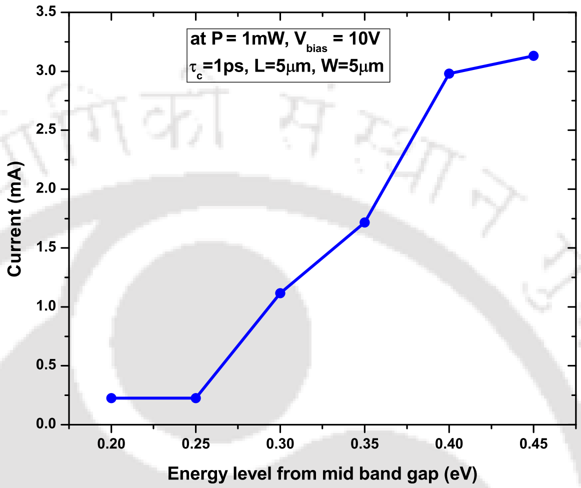

Fig. 3.19: Effect of the traps energy levels on the current pulse

3.7 Summary

Table 3.3: Summary of the simulation studies

Parameter	Value	Current pulse amplitude	Remark
Bias voltage	↑	↑	Limited by substrate electrical breakdown
Laser power	↑	↑	Limited by substrate thermal breakdown
Laser pulse width	↑	↓	-
Laser spot radius	↑	↑	Laser spot is centered at the meddle of the gap
Laser spot position	↑	↓	Moving the spot from anode to cathode
Antenna geometry	-	↑	Compared the plane, the comb and the interdigited structured electrodes PCA
Carrier lifetime	↑	↑	At the same time pulse width also increases
Substrate temperature	↑	↓	
Traps energy level	↑	↑	Moving towards the conduction band

In this chapter, a simulation study of current pulse generated in a PCA has been presented using the semiconductor simulator Sentaurus TCAD. The effect of the bias voltage, the laser power and its pulse width, the laser spot radius and its position, the antenna geometry, the carrier lifetime, the substrate temperature and the traps energy level on the generated current pulse has been analyzed. The results show that the amplitude of the current pulse can be enhanced by varying the properties of above-said parameters. A summary of the results is provided in Table 3.3.

4

An Equivalent Electrical Circuit Model of the Photoconductive Antenna

Contents

4.1 Introduction

The efficiency of the PCA as a source of THz radiation, affects the performance of the THz system based on it. Therefore, a detailed investigation of the PCA's perfromance is crucial. As discussed earlier in section 2.3.2, very few equivalent electrical circuit models of the PCAs are proposed in the literature [130–133]. However, due to certain limitations as discussed in section 2.3.2, these circuit models do not reflect the PCA behavior very accurately. Scopes still exist in developing circuit model of PCA which takes into account comprehensively the different phenomena involved in PCA operation.

In this chapter, an improved equivalent electrical circuit of the PCA working as a THz source is developed with the aim to overcome some of the limitations of the previously proposed circuit models. The circuit model proposed in this chapter is based on lumped element approach and includes the physical phenomenon involved in the device operation to make it comprehensive. Furthermore, using the developed circuit model, the effect of the different physical parameters on the characteristics of the PCA and transient behavior of various circuit components are analyzed. To validate the results computed using proposed circuit model, several results are compared with the simulation results presented in Chapter 3 and the experimental results reported in the literature.

In addition, this chapter also proposes a novel electrical equivalent circuit of the PCA working as a THz detector. The circuit model presented for the PCA detector uses the same methodologies, as proposed for the PCA source, to compute the value of the circuit parameters. Based on the developed circuit model, a comparative study of the PCA detector in noisy and noise free medium is carried out and the results are presented.

4.2 Generation of the THz Radiation from the PCA

A brief description of the THz wave generation from the PCA is discussed in section 1.6. Here, a more in-depth discussion of the working principle of the PCA is given to understand the various physics undergoing in it. The primary purpose of this is to relate the different components of the circuit with the physical phenomenon occurring in the PCA operation.

In a PCA, a laser beam illuminates the gap area or active region and generate photo-carriers. The electron-hole pair generation in the semiconductor material depends on the energy of the photon of the laser beam. If the energy of the incident photon is greater than the bandgap energy of the semiconductor substrate, it generates an electron-hole pair, or else the energy gets dissipated without the carrier generation. The applied bias voltage (V_{bias}) to the electrodes setup an electric field (E_{bias}) in the active region which accelerates the photo-carriers towards the respective electrodes, thereby producing a photo-current pulse through the antenna structure. It is imperative to note that, only a fraction of the generated carriers contribute towards the current pulse generation; remaining of them stay in the active region separated by the electric field. The separation of the carriers generates a polarization (P_s) effect which produces a reverse electric field and reduces the strength of the net electric field in the active region. The voltage associated with the polarization electric field is known as screening voltage (V_s). In PCA, the laser illumination period and the carrier lifetime are very short which facilitate the generation of an ultrafast changing current pulse and the THz radiation from the PCA.

The generation of photo-carriers in the semiconductor material increases the conductivity of in the gap. The conductance (G_p) at the gap increases with the material conductivity. The carrier polarization intensity depend on the amplitude of the net electric field in the active region. The reverse voltage (V_s) due to the polarization effect can be modeled as a voltage-dependent source which depends on the net voltage/electric field across the gap. Also, the accumulation of the charges generates a capacitance (C_p) in the gap region. The power loss due to the radiation from the PCA can be modeled as a loss across a radiation resistance (Z_a) of the antenna. Adding all the effects stated above, the PCA can be modeled as a combination of G_p, C_p, V_s and Z_a.

4.3 Proposed Equivalent Electrical Circuit Model of the PCA Working as the THz Source

In general, the electrodes gap dimensions are small compared to the radiated wavelength from the PCA. Therefore, it is possible to apply a lumped element approach in developing an equivalent circuit model of the PCA.

Under the dark condition, a PCA can be represented as a parallel combination of the substrate resistance (R_s) and the gap capacitance (C_s) across the antenna electrodes, as shown in Fig. 4.1. The resistance accounts for the flow of dark current through the substrate in the absence of the laser illumination. The semiconductor substrate resistance is of the order of $M\Omega$ [80, 150] which makes the dark current very small. Furthermore, the capacitance accounts for the voltage drop across the gap.

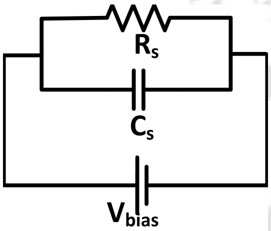

Fig. 4.1: An equivalent circuit of the PCA in dark condition

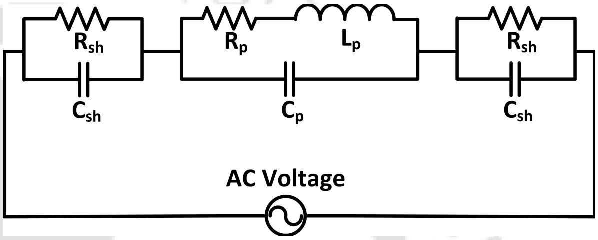

Fig. 4.2: An equivalent circuit of the parallel plate plasma

The laser illumination at the gap generates a high density of electron-hole pairs in and around the active volume in the semiconductor substrate, which can be modeled as the plasma medium. A typical equivalent electrical circuit of the plasma medium in a parallel plate circuit under an AC bias is shown in Fig. 4.2 [151]. R_{sh} and C_{sh} are related to the sheath created near to the electrode plates. R_p, L_p, and C_p are related to the plasma medium, where L_p is the kinetic inductance resulting from the electrons moment of inertia due to the AC voltage supply.

In case of a PCA, the circuit given in Fig. 4.2 is reduced to the parallel combination of R_p and C_p only. The sheath formation is neglected due to a minimal contact area with the plasma in the active region of the PCA. Also, since a DC voltage supply is used, L_p can be dropped out from the proposed model. The plasma generated at the active region is represented by

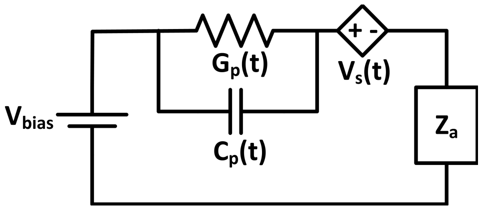

Fig. 4.3: An equivalent circuit of the PCA in transient illumination state

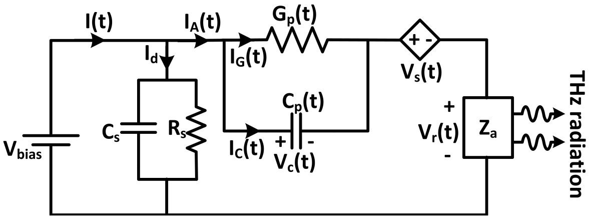

Fig. 4.4: Proposed equivalent electrical circuit of a PCA working as a THz source

the parallel combination of $G_p(t)$ and $C_p(t)$ as shown in Fig 4.3, where G_p is the conductance corresponding to R_p. The radiation resistance (Z_a) accounts for the loss of the power due to the radiation from the antenna. The time-dependent screening voltage ($V_s(t)$) is placed in the series with the parallel combination, as shown in Fig. 4.3.

Fig. 4.4 shows the proposed equivalent electrical circuit of a PCA, which is the combination of circuits under the dark and the illuminated conditions. The description of the different currents and voltages in the proposed circuit are as follows:

- $I(t)$ = Time dependent total circuit current.
- I_d = Current in the absence of the laser illumination.
- $I_A(t)$ = Time dependent total current through the gap.
- $I_G(t)$ = Time dependent current through the conductance.
- $I_c(t)$ = Time dependent capacitive current through the capacitance.
- $V_c(t)$ = Time dependent voltage across the capacitance.
- $V_s(t)$ = Time dependent screening voltage.
- $V_r(t)$ = Time dependent radiation voltage.

4.3.1 Calculations of the Circuit Parameters

In order to calculate the values of different parameters and their dependency on the other circuital parameters, some assumptions are considered in the modeling study and are as follows:

- The laser beam uniformly illuminates the gap region.
- A uniform electric field exists at the gap.
- The diffusion current through the dark capacitance (C_s) is very small and is neglected.
- The electrodes are very long compared to the gap dimension, and the performance of the antenna depends on the gap size only.
- The antenna losses are neglected and the radiation efficiency of the antenna is considered to be equal to 1.

The Fig. 4.5 shows the flow of analytical calculation of circuital parameters and their interdependencies.

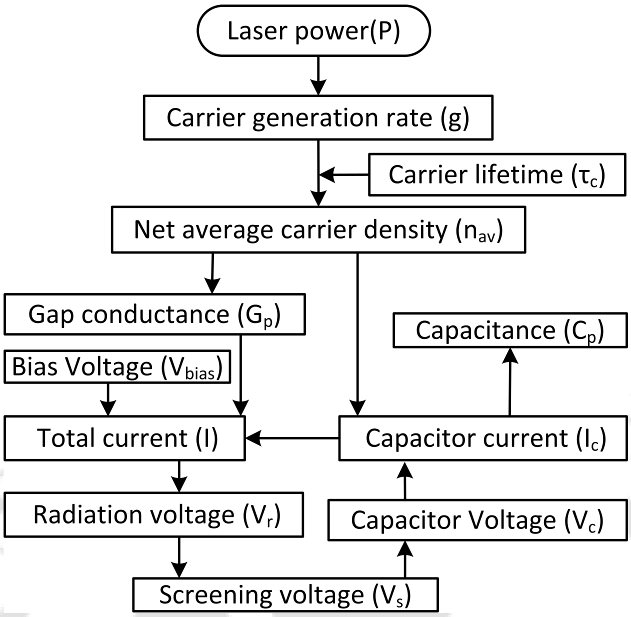

Fig. 4.5: Flow chart of the analytical calculations

4.3.1.1 Carrier Density

The time dependent carrier density ($n(t)$) in the active volume can be calculated by using the continuity equation given as [141, 142]:

$$\frac{dn(t)}{dt} = -\frac{n(t)}{\tau_c} + g(t) \tag{4.1}$$

where τ_c is the carrier lifetime and $g(t)$ is the time dependent generation rate of the carriers.

The carrier generation rate is calculated by considering a pulsed Gaussian laser beam with the power distribution given as [152]:

$$P_l(t, r) = P_0 \times e^{\left(-\frac{2r^2}{\omega_0^2}\right)} \times e^{\left(-\frac{2t^2}{\tau_l^2}\right)} \tag{4.2}$$

where P_0 is the laser peak power, ω_0 is the laser beam waist radius at $z = 0$ (at the air-semiconductor interface), and τ_l is the laser pulse width.

The power contained within the radius r is given as:

$$P(t, r) = P_0 \times \left[1 - e^{\left(-\frac{2r^2}{\omega_0^2}\right)}\right] \times e^{\left(-\frac{2t^2}{\tau_l^2}\right)} \tag{4.3}$$

The time dependent photo-generation rate ($g(t)$) using a Gaussian profile laser beam in the PCA is given as:

$$g(t) = \frac{2P(t,r)}{\pi\omega_0^2 h\nu_{opt}} \tag{4.4}$$

where h is Planck's constant, and ν_{opt} is the laser frequency.

The total number of the carriers in the active volume using (4.1) can be evaluated as:

$$n(t,r) = \frac{(1-R)\tau_l P_0 WL}{\sqrt{2\pi}h\nu_{opt}\omega_0^2}\left[1 - e^{\left(-\frac{2r^2}{\omega_0^2}\right)}\right]\left[1 - e^{(-\alpha d)}\right] e^{\left(\frac{\tau_l^2}{8\tau_c^2} - \frac{t}{\tau_c}\right)}\left[1 + \mathrm{erf}\left(\frac{\sqrt{2}t}{\tau_l} - \frac{\sqrt{2}\tau_l}{4\tau_c}\right)\right] \tag{4.5}$$

where α is the power absorption coefficient, and d is the laser skin depth in the semiconductor substrate material.

The average time dependent carrier density, $n_{av}(t)$, in the active volume can be written as:

$$n_{av}(t) = \frac{(1-R)\tau_l P_0}{\sqrt{2\pi}h\nu_{opt}\omega_0^2 d}\left[1 - e^{\left(-\frac{2r^2}{\omega_0^2}\right)}\right] \times \left[1 - e^{(-\alpha d)}\right] \times e^{\left(\frac{\tau_l^2}{8\tau_c^2} - \frac{t}{\tau_c}\right)}\left[1 + \mathrm{erf}\left(\frac{\sqrt{2}t}{\tau_l} - \frac{\sqrt{2}\tau_l}{4\tau_c}\right)\right] \tag{4.6}$$

where the active volume is L in length, W in width and d in depth.

4.3.1.2 Gap Conductance

The time-dependent gap conductance ($G_p(t)$) controls the behavior of the drift current in the active volume. The incremental gap conductance ($dG_p(t)$) for a small thickness dz in the active volume can be calculated as:

$$dG_p(t) = \left[\frac{\rho(t)L}{Wdz}\right]^{-1} \tag{4.7}$$

where $\rho(t)$ is the time-dependent resistivity, and L is the length of the active region.

The total gap conductance in the active volume can be written as:

$$G_p(t) = \frac{q\mu_e W n_{av}(t)d}{L} \tag{4.8}$$

where q is an electron charge, μ_e is the average mobility of the carriers, and W is the width of the active region.

The average mobility (μ_e) of the carriers is calculated by using Caughey-Thomas, and Arora mobility models as explained in section 3.2.6 and given as:

$$\frac{1}{\mu_e} = \frac{1}{\mu_{elec}} + \frac{1}{\mu_{dop}} \tag{4.9}$$

where μ_{elec} is the electric field dependent mobility of the carriers obtained from the Caughey-Thomas mobility model and μ_{dop} is the doping dependent mobility of the carriers obtained from the Arora mobility model.

4.3.1.3 Capacitive Current

The current through the capacitor is a diffusion current resulting due to the low carrier concentration region near the electrodes. The capacitor current can be evaluated by calculating the total number of carriers collected at the electrode within a very small time step Δt. The volume corresponding to the distance covered by the photo-carriers within Δt is approximated to be one-fourth of the cylindrical volume within the active region as shown in Fig. 4.6. So, the time-dependent capacitance current can be evaluated as:

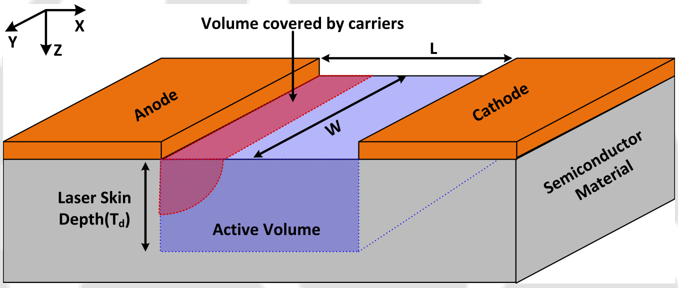

Fig. 4.6: 3D representation of the volume corresponding to the distance covered by the carriers in Δt time step

$$I_c(t) = \frac{\pi q \mu_e^2 \Delta t W n_{av}(t) V_c^2(t)}{4L^2} \tag{4.10}$$

4.3.1.4 Active Region Capacitance

The variation in the photo-carriers density in the quasi-neutral region with applied voltage yields a capacitance which is called diffusion capacitance. Using the small-signal analysis, this capacitance can be given as:

$$C_p(t) = \frac{dQ(t)}{dV_c(t)} \tag{4.11}$$

where $Q(t)$ is the change in the charge density in the active volume in Δt time.

The $Q(t)$ and $C_p(t)$ can be written as:

$$Q(t) = I_c(t)\Delta t \tag{4.12}$$

$$C_p(t) = \frac{\pi q \mu_e^2 \Delta t^2 W n_{av}(t) V_c(t)}{2L^2} \tag{4.13}$$

4.3.1.5 Screening Voltage

The carriers present in the active volume develope the screening voltage which opposes the effect of the bias voltage. The main reason behind the generation of the screening voltage is the polarization of the carriers due to the applied electric field. The time-dependent polarization ($P_s(t)$) can be written as [153]:

$$\frac{dP_s(t)}{dt} = -\frac{P_s(t)}{\tau_r} + J(t) \tag{4.14}$$

where τ_r is carrier recombination time, and $J(t)$ is current density.

The solution of the above equation can be written as:

$$P_s(t) = q\, e^{\left(-\frac{t}{\tau_r}\right)} \int_{-\infty}^{t} n_{av}(t')\, \upsilon_e(t')\, e^{\left(\frac{t'}{\tau_r}\right)} dt' \tag{4.15}$$

The voltage associated with P_s is ($V_s(t)$) and can be written as:

$$V_s(t) = \frac{q\mu_e}{K\varepsilon} e^{\left(-\frac{t}{\tau_r}\right)} \int_{-\infty}^{t} n_{av}(t')\, V_c(t')\, e^{\left(\frac{t'}{\tau_r}\right)} dt' \tag{4.16}$$

where K is the screening factor, and ε is the semiconductor material permittivity.

4.3.1.6 Total Circuit Current

Applying Kirchhoff's circuit law to the equivalent electrical circuit presented in Fig. 4.4, the total circuit current ($I(t)$) can be expressed as:

$$I(t) = I_A(t) + I_d = G_p(t)V_c(t) + I_c(t) + \frac{V_{bias}}{R_s} \tag{4.17}$$

The dark state resistance (R_S) of the material is very high (of the order of $M\Omega$). So, the contribution of the dark current $\left(\frac{V_{bias}}{R_s}\right)$ in the total circuit current is very small and is neglected in further calculations.

4.3.1.7 Voltage Across the Gap Capacitance

Applying Kirchhoff's voltage law, on the electrical circuit in Fig. 4.4, the voltage across the capacitor can be determined as:

$$V_c(t) = V_{bias} - V_r(t) - V_s(t) \tag{4.18}$$

where the time dependent radiation voltage ($V_r(t)$) can be given as:

$$V_r(t) = G_p(t)V_c(t)Z_a + I_c(t)Z_a \tag{4.19}$$

From (4.16)), (4.18) and (4.19):

$$V_c(t) = V_{bias} - G_p(t)V_c(t)Z_a - I_c(t)Z_a - \frac{q\mu_e}{K\varepsilon}e^{\left(-\frac{t}{\tau_r}\right)} \int_{-\infty}^{t} n_{av}(t')\ V_c(t')\ e^{\left(\frac{t'}{\tau_r}\right)}dt' \tag{4.20}$$

In order to solve the above equation, differentiating it with respect to time;

$$\begin{aligned}\frac{dV_c(t)}{dt} = -Z_a\left[G_p(t)\frac{dV_c(t)}{dt} + V_c(t)\frac{dG_p(t)}{dt} + \frac{dI_c(t)}{dt}\right] - \\ \frac{q\mu_e}{K\epsilon}\left[\frac{-1}{\tau_r}\left\{e^{\left(-\frac{t}{\tau_r}\right)} \int_{-\infty}^{t} n_{av}(t')\ V_c(t')\ e^{\left(\frac{t'}{\tau_r}\right)}dt'\right\} + n_{av}(t)V_c(t)\right]\end{aligned} \tag{4.21}$$

Substituting the value of integral from (4.20);

$$\begin{aligned}\frac{dV_c(t)}{dt} = \frac{1}{1 + \{G_p(t) + 2Cn_{av}(t)V_c(t)\}Z_a}\left[\frac{V_{bias}}{\tau_r} - V_c(t)\left(\frac{1 + G_p(t)Z_a}{\tau_r} + \frac{q\mu_e}{K\epsilon}n_{av}(t)\right.\right. \\ \left.\left. + BZ_a\frac{dn_{av}(t)}{dt}\right) - CZ_aV_c^2(t)\left(\frac{dn_{av}(t)}{dt} + \frac{n_{av}(t)}{\tau_r}\right)\right]\end{aligned} \tag{4.22}$$

where $B = \dfrac{e\mu_e Wd}{L}$ and $C = \dfrac{\pi e\mu_e^2 W\Delta t}{4L^2}$

The value of the different parameters can be evaluated by solving (4.3.1.7). The Finite Difference Method (FDM) is used to solve the above differential equation. The basic information about FDM is provided in Appendix A.1.

4.3.1.8 Effect of the Temperature

The laser beam transfers the energy to the substrate material in the form of heat and ionization energy. Heating of the substrate material increases the overall temperature of the PCA.

The increase in the temperature of the substrate material changes the values of the different parameters associated with it, which affects the PCA's performance.

The temperature dependence of the permittivity of the GaAs material is given as [154]:

$$\varepsilon_r(T) = \varepsilon_a(1 + \lambda T) \tag{4.23}$$

The temperature dependencey of the optical absorption coefficient of the GaAs is given as [155]:

$$\alpha(T) = \alpha_g e^{\left(\frac{h\nu_{opt} - E_G(T)}{E_0(T)}\right)} \tag{4.24}$$

$$E_G(T) = E_G(0) - S_v k\theta_v \left(\frac{T^2}{\theta_v^2 + \theta_v T}\right) \tag{4.25}$$

$$E_0(T) = S_0 k\theta_E \left(\frac{1 + X}{2} + \frac{1}{e^{(\theta_E/T)} - 1}\right) \tag{4.26}$$

The value of the different coefficient related to above equations are given in Table 4.1.

Table 4.1: Details of the parameters for the temperature analysis

Parameter	Value
ε_a [154]	12.166
λ [154]	$2.01 \times 10^{-4}/^\circ K$
α_g [155]	$7835\ cm^{-1}$
$E_G(0)$ [155]	$1.51914\ eV$
S_v [155]	6.30
k [155]	$8.617342 \times 10^{-5} eV/^\circ K$
θ_v [155]	$199.4^\circ K$
S_0 [155]	0.129
θ_E [155]	$270^\circ K$
X [155]	1.2

The temperature dependent power reflection coefficient (R) can be expressed as:

$$R(T) = \left|\frac{1 - \sqrt{\varepsilon_r(T)}}{1 + \sqrt{\varepsilon_r(T)}}\right|^2 \tag{4.27}$$

4.3.2 Results and Discussions

In order to investigate the behavior of the PCA using the proposed circuit model, values of the different parameters used in the calculations are given in Table 4.2 [76, 132].

Table 4.2: Parameters Details (at 300° K) for the circuit modeling

Parameter	**Value**
Optical absorption coefficient (α)	6000 cm^{-1}
Laser frequency (ν_{opt})	375 THz
Laser repetition frequency (f_{rep})	80 MHz
Laser pulse duration (τ_l)	100 fs
Carrier lifetime (τ_c)	1 ps
Carrier recombination time (τ_r)	100 ps
Screening factor (K)	900
Antenna gap length (L)	10 μm
Antenna gap width (W)	10 μm
Laser skin depth (d)	1 μm
Antenna resistance (Z_a)	65Ω
Relative Permittivity (ε_r)	12.9
Dark Resistance (R_s)	6.2 MΩ

Several applications of the PCA demand high radiated power and radiation efficiency. In the PCA, three different efficiencies exist, the optical-to-electrical conversion efficiency (η_e), the matching efficiency (η_m), and the electrical-to-THz conversion efficiency (η_r). η_e is the ratio of the electrical power generated in the PCA to the optical input power. Similarly, η_m is the ratio of the electrical power delivered to the antenna and the maximum available electrical power which can be delivered to the antenna under the impedance matched condition. Also, η_r is the ratio of the radiated power to the electrical power coupled to the antenna. In the present study, according to the assumption, η_r is 1. The total efficiency η_t of the PCA is the product of the three efficiencies mentioned above and can be written as:

$$\eta_t = \eta_e \times \eta_m \times \eta_r \tag{4.28}$$

$$\eta_t = \frac{P_{THz}(peak)}{P_0} \tag{4.29}$$

where P_0 is the peak optical input power and P_{THz} is the radiated power. Fig. 4.7 shows the effect of the laser power on η_e, η_m, and η_t. From (4.28), it is evident that the overall efficiency can be increased by improving η_e. Moreover, increasing the amplitude of the current pulse by using different methods such as increasing power coupling efficiency, modifying the antenna geometry to collect more carriers, and enhancing the carrier mobility, can provide a better η_e.

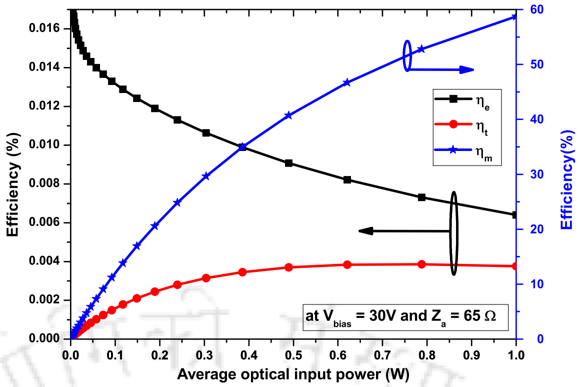

Fig. 4.7: Comparison of the optical-to-electrical (η_e), the matching (η_m), and the total (η_t) efficiency

4.3.2.1 Effect of the Laser Power and the Bias Voltage

A high laser input power generates high carrier density in the active volume resulting in an increased total current. Similarly, a large bias voltage facilitates fast acceleration, consequently, a large number of the carriers get collected at the electrodes and effectively generates a high amplitude current pulse. Fig. 4.8 & 4.9 show the effect of the laser input power and the bias voltage on the behavior of the current pulse in the PCA.

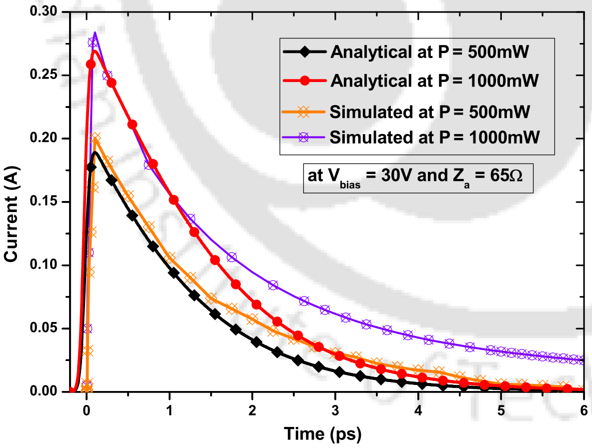

Fig. 4.8: Current pulse behavior at the different laser powers

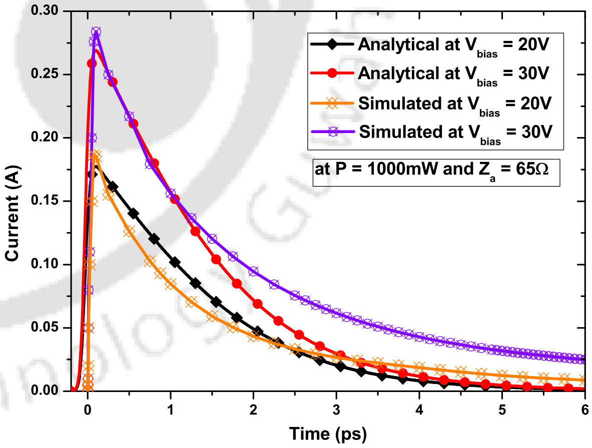

Fig. 4.9: Current pulse behavior at the different bias voltages

The current pulse behavior obtained from the circuit analysis is compared with the simulation results presented in the chapter 3. It may be observed that both of the results are in close agreement except for the falling edge of the current pulse, particularly for the high amplitude current pulse (resulting from high laser power with high bias voltage). The difference between the results may be attributed to some of the effects such as the band-to-band transition of the carriers, complex refractive index, and the different scattering mechanism, which are not included in the analytical calculations.

The radiated power from the PCA, P_{THz} is calculated as:

$$P_{THz}(t) = \frac{V_r^2(t)}{Z_a} = I^2(t)Z_a \tag{4.30}$$

Since P_{THz} and η_t are proportional to $I(t)$, they have the same dependency on the P and V_{bias} as shown in Figs. 4.10 & 4.11. However, P_{THz} and η_t are observed to be strongly dependent on the changes in the optical input power as compared to changes in the bias voltage. The maximum limit of the bias voltage and the optical input power which can be applied to the PCA are restricted by the electrical and the thermal breakdown limits of the substrate material. From Figs. 4.10 & 4.11, it can be observed that P_{THz} and η_t start saturating after certain optical power, which can be attributed to the saturation of the current amplitude at those values of the optical power at a fixed bias voltage.

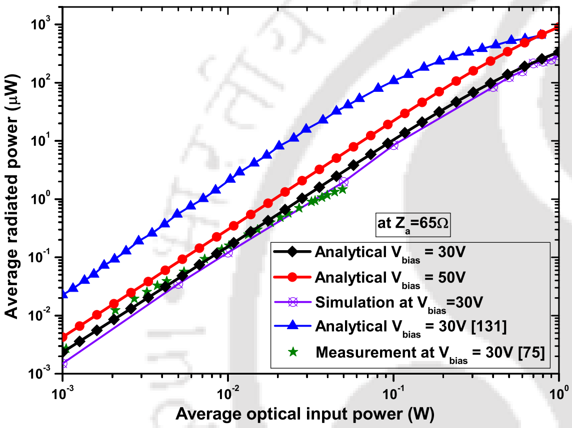

Fig. 4.10: The average radiated power at different V_{bias}

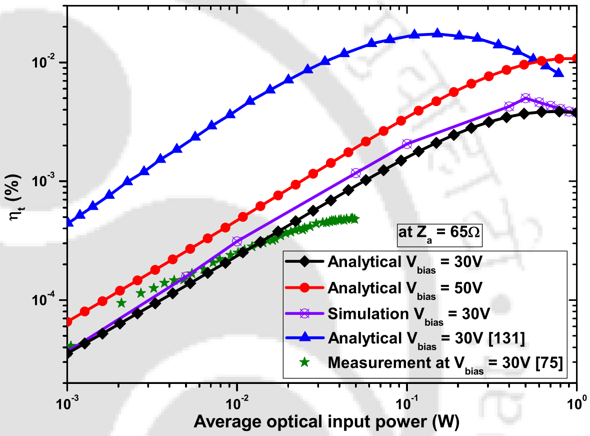

Fig. 4.11: Efficiency of the PCA at different V_{bias}

To validate the presented analysis, the results of P_{THz} and η_t obtained from the proposed circuit model are compared with the experimental results from Tani *et al.* [76] and the simulation results from the chapter 3. It is apparent from Figs.4.10 & 4.11 that results are in close agreement with the experimental and the simulation results. Moreover, the results are compared with the proposed circuit model of the PCA by Khiabani *et al.* [132] and found that the proposed circuit model in this chapter is more accurate.

4.3.2.2 Effect of the Temperature

The semiconductor material parameters are temperature dependent and a change in the substrate temperature (T) modifies the values of the parameters which affect the PCA's performance. There can be several reasons behind the change in the substrate temperature such as the laser power dissipation, the carrier-to-carrier collisions, and the power loss due to the substrate resistance. The increase in the temperature reduces the coupling efficiency and the carrier mobility, therefore, minimizing the carrier density in the active volume. A small value of the carrier density produces a low amplitude of the current pulse as shown in Fig. 4.12 consequently reducing P_{THz} and η_t of the PCA as shown in Figs. 4.13 & 4.14.

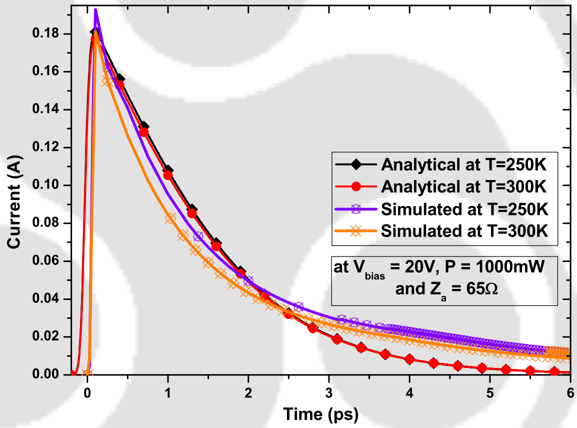

Fig. 4.12: Current pulse dependence on the temperature

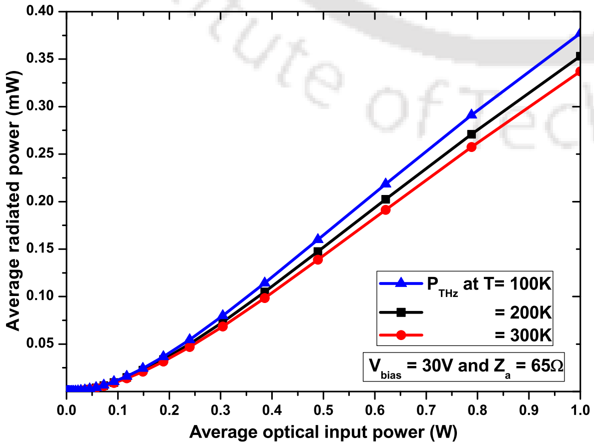

Fig. 4.13: Dependence of the average radiated power on the temperature

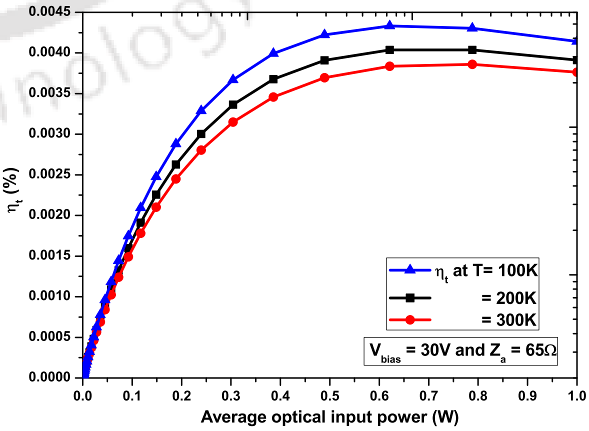

Fig. 4.14: Dependence of the PCA efficiency on the temperature

4.3.2.3 Effect of the Gap Length and the Carrier Lifetime

The net electric field as well as the current pulse amplitude strongly depend on the gap length (L). Increasing L decreases the net electric field which results in reduction of carrier velocity. As a consequence, the current pulse amplitude decreases as the carriers take longer time to reach the electrodes due to reduced velocity. The same behavior can be verified from Fig. 4.15. The behavior of P_{THz} and η_t also follow the same trend as the current pulse amplitude as shown in Figs. 4.16 & 4.17.

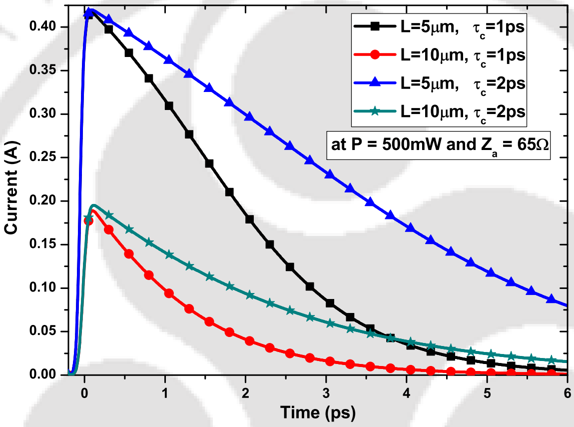

Fig. 4.15: Current pulse for different L and τ_c

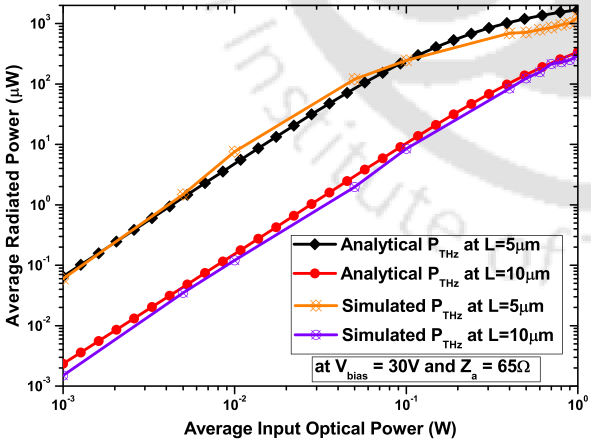

Fig. 4.16: Dependence of the average radiated power on L

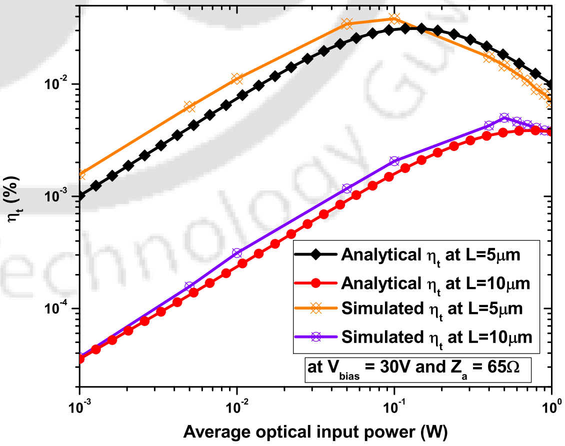

Fig. 4.17: Dependence of the PCA efficiency on L

The carrier lifetime (τ_c) defines how much time a carrier remains in the gap without recombining with the trap centers. Hence, a large value of τ_c increases the probability of the carriers to get collected at the electrodes. The value of τ_c mainly depends on the concentration of the

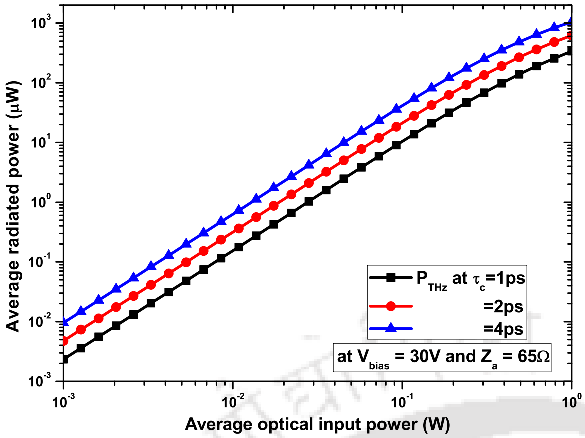

Fig. 4.18: Dependence of the average radiated power on τ_c

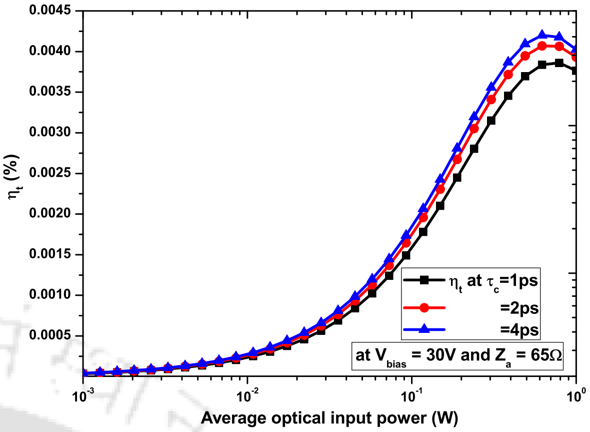

Fig. 4.19: Dependence of the PCA efficiency on τ_c

traps in the semiconductor material which is determined by the fabrication procedures and conditions [109]. Large values of τ_c effectively increases the amplitude and the pulse width of the current pulse as the carrier remain in the gap for a longer time and get collected at the electrodes as shown in Fig. 4.15. The amplitude of P_{THz} and η_t also increase with τ_c as shown in Figs. 4.18 & 4.19. The pulse width of the current pulse determines the maximum radiated frequency from the antenna and has an inverse relationship. In other words, the PCA with τ_c and L such that it generates high amplitude current pulse with a low pulse width is more suitable to radiate high THz frequencies.

4.3.2.4 Effect of the Antenna Impedance

The antenna impedance (Z_a) accounts for the power loss due to the radiation from the PCA. A large value of the antenna impedance facilitates high power loss across the antenna in the

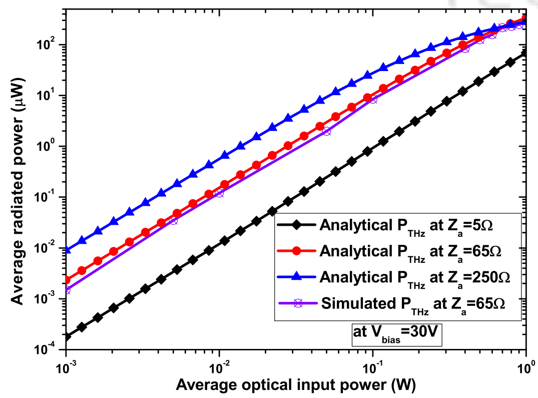

Fig. 4.20: Dependence of the average radiated power on Z_a

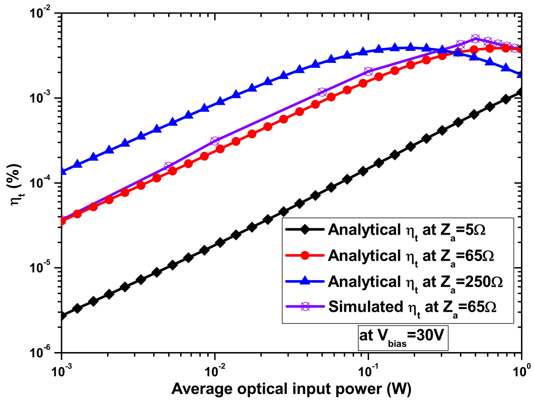

Fig. 4.21: Dependence of the PCA efficiency on Z_a

form of the radiation. From Fig. 4.20, it is evident that increasing Z_a, one can increase P_{THz}. However, at high optical input powers, the radiated power gets saturated due to the saturation of the current pulse. It is observed that the saturation of the radiated power is slower for the smaller values of Z_a. Moreover, for the large values of Z_a, the peak efficiency occurs at lower optical input powers as shown in Fig. 4.21. However, the peak efficiency of the PCA for the different values of Z_a changes only marginally.

4.3.2.5 Effect of the Absorption and the Reflection Coefficients

The PCA efficiency can be increased by increasing the overall optical power coupled to the semiconductor substrate. The optical power coupling can be enhance by increasing the optical absorption (α) and reducing the reflection (R) coefficients of the semiconductor material. The impact of α and R on the total efficiency of the PCA are shown in Figs. 4.22 & 4.23. An increase in the absorbed power facilitates the generation of more number of the carriers in the material which results in the increased η_t. The absorption of the laser power depends on the material absorption coefficient which is a wavelength dependent parameter; so adjusting the laser wavelength, the power coupled to semiconductor material can be changed. Similarly, using different techniques to reduce the power reflection at the interface such as anti-reflective coating [156], application of nano-crystalline structures [157] etc., the power coupling can be increased.

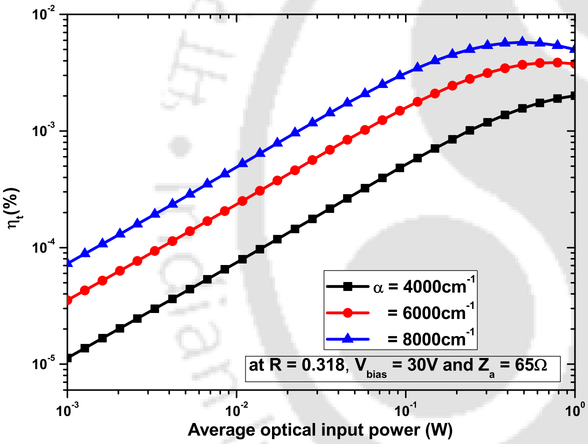

Fig. 4.22: The total efficiency of the PCA at the different absorption coefficients

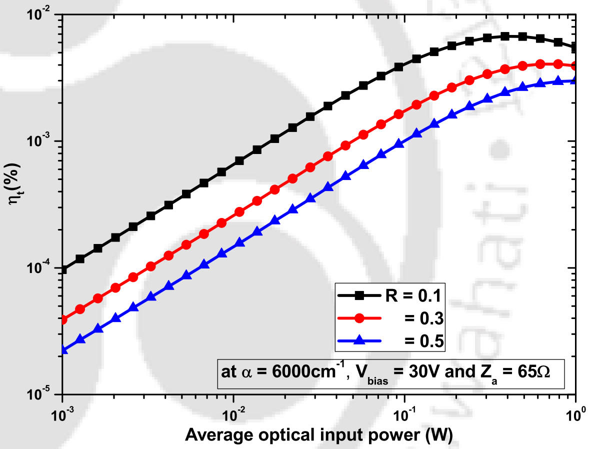

Fig. 4.23: The total efficiency of the PCA at the different reflection coefficients

4.3.2.6 Different Voltages in the PCA

Fig. 4.24 shows the effect of the optical power on the different voltages in the PCA. At any time instant, the total voltage (V_c + V_s + V_r) remains equal to the bias voltage (V_{bias}), and the same can be verified from the Fig. 4.24. The total number of the carriers increases with the laser power, which also tend to grow V_r and V_s which results in a reduced V_c. temporal behavior of the different voltage components can be verified from Fig. 4.24.

From Fig. 4.24, it can be seen that to increase the radiation efficiency of the PCA one has to reduce V_s. It limits the current flow in the PCA by reducing V_c across the active gap.

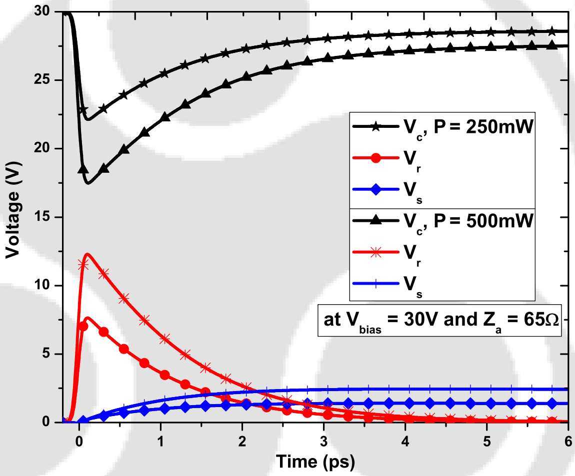

Fig. 4.24: Transient behavior of the voltages in the PCA

4.3.2.7 Gap Conductance

The gap conductance (G_p) depends on the conductivity of the semiconductor material. The material conductivity is proportional to the carrier density. So, increasing optical input power results in an increased value of the conductance in the semiconductor substrate. The same behavior of the gap conductance can be verified from Fig. 4.25. However, increasing the bias voltage decreases the effective mobility of the carriers by reducing the electric field dependent mobility value of the carriers. From (4.8), it can be seen that the conductance is directly proportional to mobility of the carriers. So, an increase in the bias voltage decreases the conductance value at the gap and the same can be observed in Fig. 4.26.

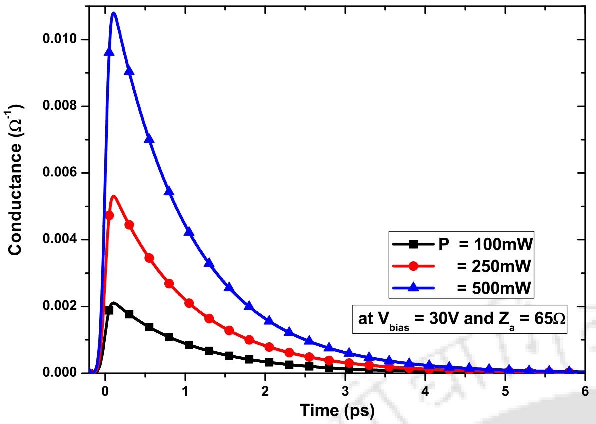

Fig. 4.25: Transient behavior of the conductance at different laser powers

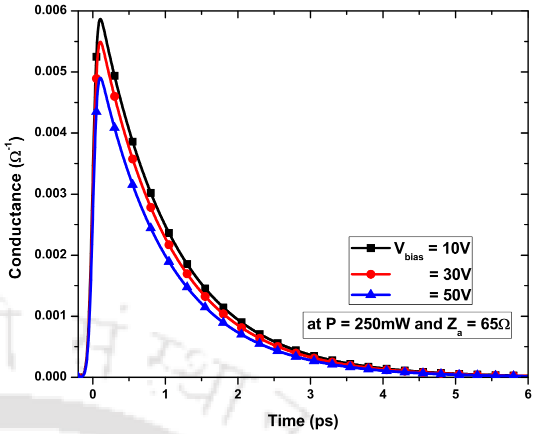

Fig. 4.26: Transient behavior of the conductance at different bias voltages

4.3.2.8 Gap Capacitance

The gap/active region capacitance depends on the carrier density at the gap and the voltage across it as given by (4.13). Increasing the laser power produces high carrier density at the gap thereby increasing the value of the capacitance as shown in Fig. 4.27. The voltage across the capacitor (V_c) is related to the bias voltage as given in (4.18). Increasing the bias voltage increases the amplitude of the V_c which results in a large value of the capacitance as shown in Fig. 4.28.

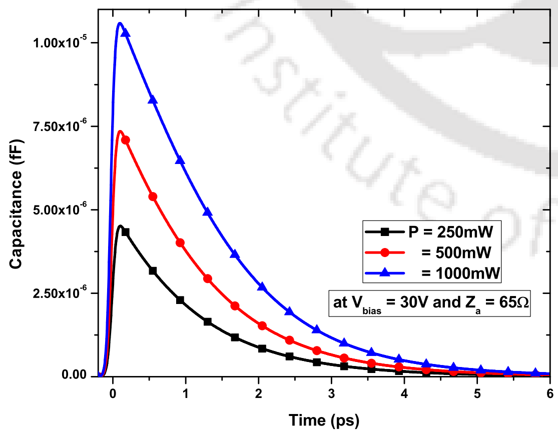

Fig. 4.27: Transient behavior of the capacitance at different laser powers

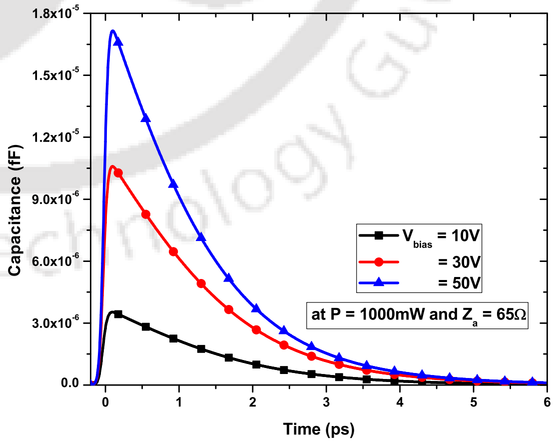

Fig. 4.28: Transient behavior of the capacitance at different bias voltages

4.4 Detection of the THz Radiation Using the PCA

Several detectors are available to detect the THz radiation as discussed in the Chapter 1, PCA can also be used for the same. The PCA working as a THz source can also be used as a detector. Except the biasing mechanism, the working principle of the PCA detector remains same as the PCA source. In this section a novel equivalent electrical circuit of the PCA working as the THz detector is proposed and analyzed. Prior to this, to the best of the author's knowledge, there is no study reported in the literature dealing with the circuit modeling of the PCA as the THz detector.

4.5 Proposed Equivalent Electrical Circuit Model of the PCA Working as the THz Receiver

The working principle of the PCA as a THz receiver is similar to the PCA as a THz source, except the fact that in receiver the electrodes do not require a voltage biasing. In the receiver, the laser beam illumination at the electrodes gap generates the photo-carriers. The density of the photo-carriers depends on the laser peak power and the gap dimensions. The electric field of the incoming THz signal develops a voltage across the gap which assist the movement of the carriers. It should be noted that the incoming THz signal and the laser beam fall on the substrate surface at the same time. As the electric field of the received signal is ultrafast so the motion of the carriers at the gap. The carrier's movement setup a transient current pulse in the PCA receiver which is further used for the post processing of the received signal.

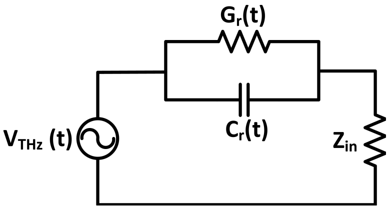

Fig. 4.29: Proposed equivalent electrical circuit of the PCA working as a THz receiver

In the proposed equivalent circuit of the PCA receiver, the gap between the electrodes is modeled as a parallel combination of the time varying conductance (G_r) and capacitance (C_r). The conductivity of the material at the gap changes due the generation of the carriers, which is modeled as the transient conductance. Similarly the presence of the carriers at the gap volume generates a capacitance effect. The impedance of the antenna structure is modeled as input impedance (Z_{in}) connected in series with the parallel combination of the conductance and capacitance. The proposed circuit of the PCA receiver is shown in Fig. 4.29.

4.5.1 Calculations of the Circuit Parameters

The working principle of the PCA source and the PCA detector is quite similar. So, to compute the circuit components, same calculations strategies are used as presented in section 4.3.1 and the values of the parameters are taken from Table 4.2.

4.5.1.1 Carrier Density

The average photo-generated carrier density at the gap can be solved by using (4.1)-(4.4) and is given as:

$$n_{rav}(t) = \frac{(1-R)\tau_l P_0}{\sqrt{2\pi} h\nu_{opt}\omega_{0r}^2 d}\left[1 - e^{\left(-\frac{2r^2}{\omega_{0r}^2}\right)}\right]\left[1 - e^{(-\alpha d)}\right] e^{\left(\frac{\tau_l^2}{8\tau_c^2} - \frac{t}{\tau_c}\right)}\left[1 + \operatorname{erf}\left(\frac{\sqrt{2}t}{\tau_l} - \frac{\sqrt{2}\tau_l}{4\tau_c}\right)\right] \tag{4.31}$$

where ω_{0r} is the laser beam waist radius at the air-semiconductor interface.

4.5.1.2 Gap Conductance

Similar to section 4.3.1.2, the transient conductance in the PCA receiver can be given as:

$$G_r(t) = \frac{q\mu_{er} W_r n_{rav}(t) d}{L_r} \tag{4.32}$$

where μ_{er} is the carrier mobility, L_r and W_r are the gap length and width, respectively.

The effective mobility of the carriers is calculated using Caughey-Thomas [145], and Arora [146] mobility models as explained in section 3.2.6 and given as:

$$\frac{1}{\mu_{er}} = \frac{1}{\mu_{elec,r}} + \frac{1}{\mu_{dop,r}} \tag{4.33}$$

where $\mu_{elec,r}$ is the electric field dependent carrier mobility obtained from Caughey-Thomas mobility model corresponding to the electric field at the receiver gap E_{rnet} and $\mu_{dop,r}$ is the doping dependent carrier mobility obtained from Arora mobility model corresponding to n_{rav}.

4.5.1.3 Capacitance Current

Using the calculation strategy provided in section 4.3.1.3, the current through the capacitance (C_r) can be given as:

$$I_{cr}(t) = \frac{\pi q \mu_{er}^2 \Delta t W_r n_{rav}(t) V_{gr}^2(t)}{4L_r^2} \tag{4.34}$$

4.5.1.4 Gap Capacitance

Using the relations proposed in section 4.3.1.4, the capacitance at the gap in the PCA receiver can be given as:

$$C_r(t) = \frac{\pi q \mu_{er}^2 \Delta t^2 W_r n_{rav}(t) V_{gr}(t)}{2L_r^2} \tag{4.35}$$

4.5.1.5 Total Circuit Current

From Fig. 4.29, the total circuit current can be written as:

$$I_r(t) = G_r(t) V_{gr}(t) + I_{cr}(t) \tag{4.36}$$

4.5.1.6 Gap Voltage

From Fig. 4.29, the voltage across the gap can be written as:

$$V_{gr}(t) = \frac{V_{THz}(t) - Z_{in} I_{cr}(t)}{1 + Z_{in} G_r(t)} \tag{4.37}$$

$$V_{THz}(t) = E_{THz} \times L_r \tag{4.38}$$

where E_{THz} is the electric field of the received THz signal which is calculate using the formula given in [82]:

$$E_{THz}(t) \cong \frac{A}{4\pi\varepsilon_0 c^2 r_d} \frac{\partial J}{\partial t} \tag{4.39}$$

where $A = W \times L$, and $J(t) = I(t) \times W \times d$, both related to the PCA working as the THz source, r_d is the distance between source and receiver which is assumed to be 100 mm in this case, and c is light velocity.

From (4.37), the net electric field at the gap can be written as:

$$E_{rnet} = \frac{V_{gr}(t)}{L_r} = \frac{V_{THz}(t) - Z_{in} I_{cr}(t)}{L_r\,(1 + Z_{in} G_r(t))} \tag{4.40}$$

4.5.2 Results and Discussions

In order to analyze the proposed equivalent electrical circuit of the PCA working as a THz receiver and to compute the circuit parameters, the value of the bias voltage $V_{bias} = 25$ V, and the laser power $P = 25$ mW are kept constant at the PCA working as the THz source. Additionally, to compare the performance of the PCA receiver, a comparison is made between the received THz signal in noisy and noise free medium. The noisy medium is assumed to have a white gaussian noise of 10 dB SNR.

4.5.2.1 Electric Field of the Received THz Signal and Induced Voltage

The received THz signal at the PCA receiver is calculated using (4.39). The received electric field at the gap of the PCA receiver in noise free and noisy mediums are shown in Figs. 4.30

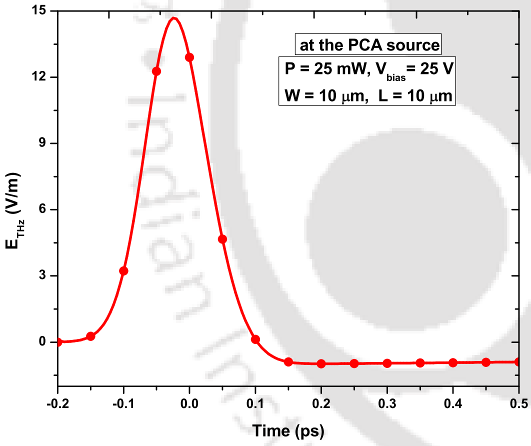

Fig. 4.30: The electric field of the received THz signal in the noise free medium

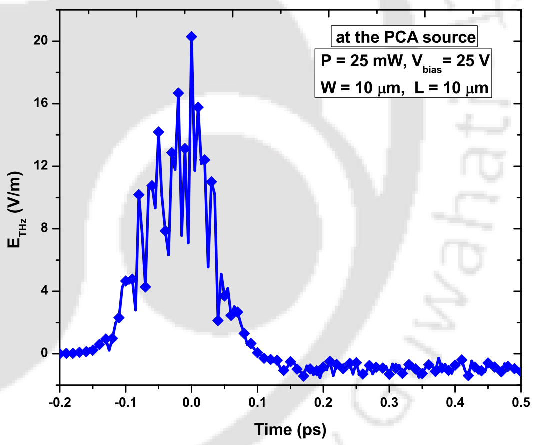

Fig. 4.31: The electric field of the received THz signal with the white gaussian noise of 10 dB SNR

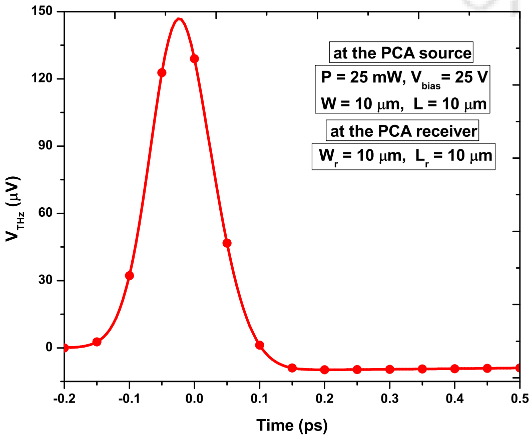

Fig. 4.32: Induced voltage at the gap in the noise free medium

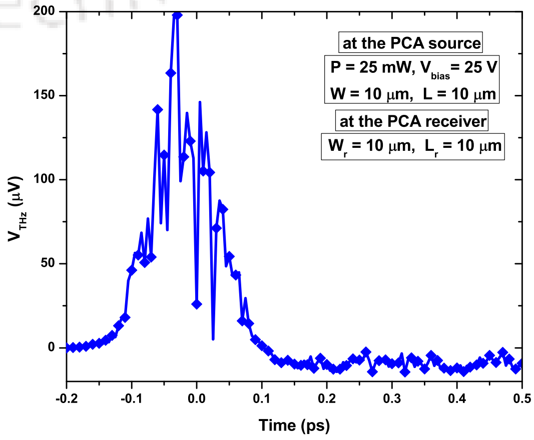

Fig. 4.33: Induced voltage at the gap with the white gaussian noise of 10 dB SNR

and 4.31. Also, the Incoming THz signal induces a voltage at the gap of the PCA receiver which are shown in Figs. 4.32 and 4.33 corresponding to the noise free and noisy mediums, respectively.

4.5.2.2 Net Electric Field at the Gap

The net electric field at the gap of the PCA receiver depends on the several parameters as given by (4.40). The behavior of the net electric at the gap in PCA receiver for a noise free and noisy mediums are shown in Figs. 4.34 and 4.35, respectively. A high net electric field at the gap facilitates a high amplitude current which increases the sensitivity of the PCA.

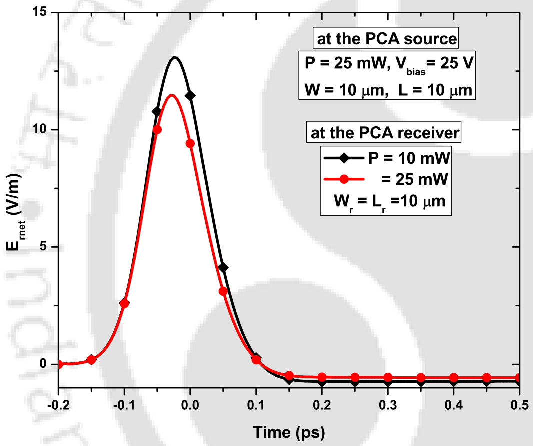

Fig. 4.34: Net electric field at the gap in the noise free medium

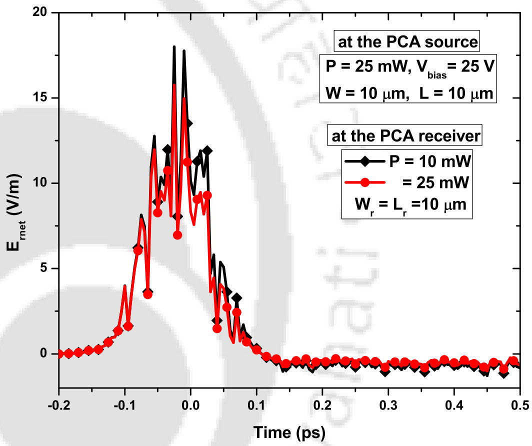

Fig. 4.35: Net electric field at the gap with the white gaussian noise of 10 dB SNR

4.5.2.3 Total Circuit Current

The total circuit current includes the currents through the conductance and the capacitance as given by (4.36). The behavior of the total circuit current in the PCA receiver is shown in Figs. 4.36 and 4.37 for the noise free and noisy mediums, respectively. The total circuit current mainly depends on the amplitude of the net electric field at the gap, which in turn depends on the gap length. So, by changing the gap length the current amplitude can be changed as shown in Fig. 4.38. It can be seen that, the amplitude of the current increases with the decrease in the gap length. The current amplitude is directly proportional to the sensitivity of the PCA receiver. Therefore, to increase the PCA receiver sensitivity, one has to use a small gap length PCA receiver.

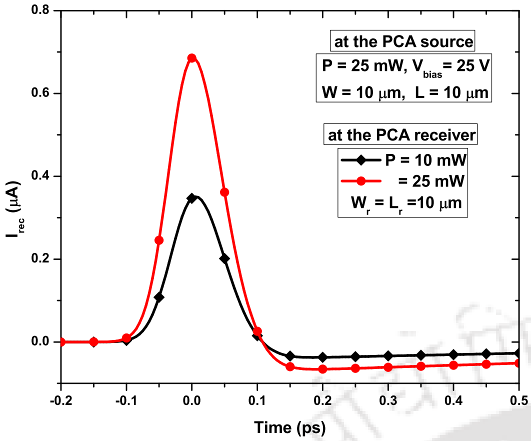

Fig. 4.36: Total circuit current in the noise free medium

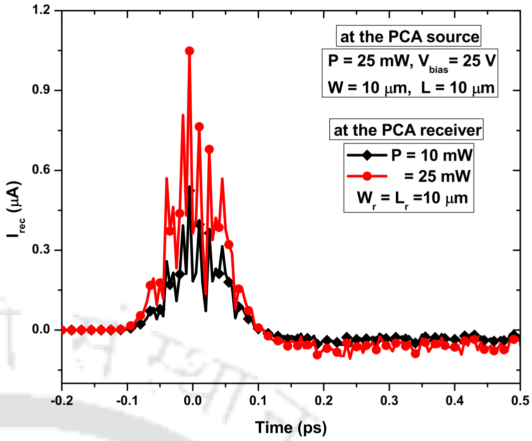

Fig. 4.37: Total circuit current for the white gaussian noise of 10 dB SNR

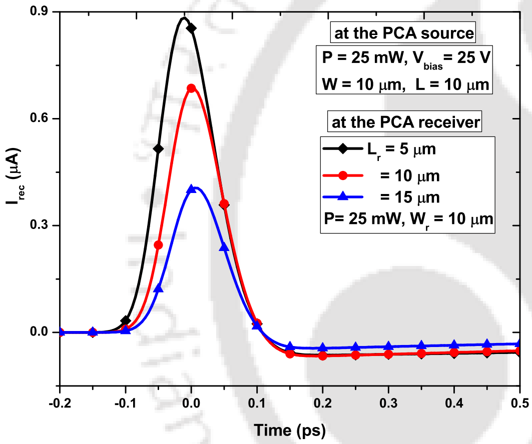

Fig. 4.38: Gap length effect on the total circuit current in the noise free medium

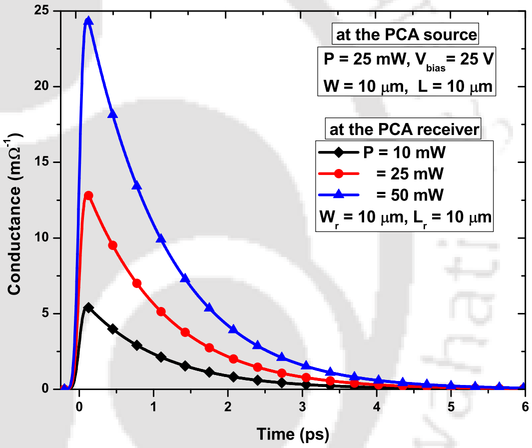

Fig. 4.39: Gap conductance of the PCA receiver in the noise free medium

4.5.2.4 Gap Conductance

The gap conductance mainly depends on the peak power of the laser beam. It increases with the laser peak power as can be seen from Fig. 4.39. A high value of the conductance supports a high amplitude current in the circuit which effectively enhances the sensitivity of the PCA receiver.

4.6 Summary

In this chapter, a detailed analysis of the PCA's performance has been carried out using equivalent electrical circuit model based studies. An improved equivalent circuit model of the PCA source, and a novel circuit of the PCA receiver has been proposed based on the physics involved in their working. It has been observed that the performance of the PCA working as a

THz radiation source can be enhanced by the different combinations of the parameters related to the substrate material, laser beam, and the antenna geometry, as shown in Table 4.3. It should be noted that the results from the macroscopic model (circuit model) presented in this study are in close agreement with the experimental results, which verifies the accuracy of the proposed analysis of the PCA source. Similarly, the performance analysis of the PCA receiver using the proposed circuit model has been carried out in the noisy and noise free mediums. The results show that, to achieve the high sensitivity, one should use a PCA receiver having a small gap length and with a high power laser beam excitation. As the analysis presented in this chapter are based on the physical parameters of the device, these studies are expected to be very useful in designing the practical and efficient THz sources and receivers using the PCAs.

Table 4.3: Summary of the PCA source analysis

Parameter	**Range**	$\eta_t(\%)$	P_{THz}	**comments**
V_{bias} (V)	10-50	(0.4-11) $\times 10^{-3}$	↑	Subjected to electrical breakdown
L (μm)	20-5	(0.25-31) $\times 10^{-3}$	↑	Decreases Radiation freq.
R	0.4-0.1	(3-6.7) $\times 10^{-3}$	↑	Requires special techniques
$\alpha(cm^{-1})$	(4-8) $\times 10^{3}$	(2-5.8) $\times 10^{-3}$	↑	Requires special techniques
$T(^{\circ}K)$	300-100	(3.9-4.3) $\times 10^{-3}$	↑	Requires additional equipment
$Z_a(\Omega)$	5-250	(1.2-3.9) $\times 10^{-3}$	↑	P_{THz} starts saturating at lower power

5

Effect of the Near Fields on the Large Aperture Photoconductive Antenna Performance

Contents

5.1 Introduction

The PCAs are widely used to generate the THz radiation which is useful for the different applications. Some of them demand high radiation power to fulfill their requirements. The radited power from the PCA depends on the several parameters and can be improved by different ways such as increasing the laser power, the bias voltage, antenna impedance, etc., as discussed in the chapter 4. Moreover, to increase the output power, large aperture PCAs (LAPCA) are also used in the literature [122, 158, 159]. The LAPCA is defined to have the gap dimensions (aperture size) much greater than the center wavelength of the radiated THz waves from it. The large aperture size facilitates the high bias voltage application which increases the amplitude of the current pulse and effectively enhances the radiated power. Although these methods improve the radiated power from the PCAs, the improvement factor still remains very small. Several factors exist which limit the performance of the PCA such as the electrical and the thermal breakdown limits, the carrier polarization, and the voltage screening. Apart from these limiting factors, the radiated near-zone fields also affect the radiated power [134] and has not been adequately addressed in the literature.

This chapter presents a analysis of the radiated near-zone fields effect on the radiated power from a LAPCA. The electromagnetic boundary conditions as well as the semiconductor carrier dynamics are used to compute the effect of the near-zone fields on the different parameters behavior.

5.2 Relationship Between the Near-Zone Fields and the Current Density

The analytical model to evaluate the radiated fields near the emitting surface of the LAPCA can be established by applying the boundary conditions on the electric and the magnetic fields at the surface/ air-semiconductor interface at the gap. In the LAPCA, the radiated wavelength is very small compared to the diameter of the current distribution. So, the radiation from these can be explained in the terms of the plane waves radiated from the planar surface of the antenna. As the calculations of the fields are very close to the surface; the retardation effect can be neglected [134].

The configuration of the different fields in the LAPCA is shown in Fig. 5.1. The near-zone magnetic and electric fields orientations have been computed using the current flow and the wave propagation directions. The different fields shown in figure are as follows:

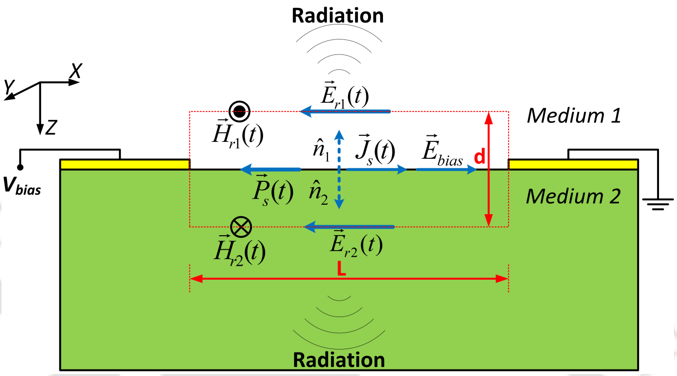

Fig. 5.1: The fields configuration in a PCA

- E_{bias}: The field due to the applied bias voltage.
- J_s: The surface current density at the electrodes gap.
- P_s: The polarization due to the applied electric field.
- E_{r1}: The radiated near-zone electric field in medium 1.
- H_{r1}: The radiated near-zone magnetic field in medium 1, pointing out of the page.
- E_{r2}: The radiated near-zone electric field in medium 2.
- H_{r2}: The radiated near-zone magnetic field in medium 2, pointing into the page.
- $\hat{n}_1$: Unit vector along the wave propagation direction in medium 1.
- $\hat{n}_2$: Unit vector along the wave propagation direction in medium 2.

where the medium 1 and 2 are air and the semiconductor substrate material, respectively. The gap area is L in length and W in width. As the radiated waves propagate along z-axis, unit vector $\hat{n}_z$ is used to show the direction of the wave propagation.

In spite of the time-varying nature, the steady state boundary conditions on the electric and the magnetic fields are applicable at the interface of the two media. From Fig. 5.1, the boundary condition of the electric field is given as [160]:

$$\oint_c \vec{E} \cdot d\vec{l} = -\int_s \mu \frac{\partial \vec{H}}{\partial t} \cdot \hat{n}_y ds \tag{5.1}$$

where c is the closed line of integral enclosing the surface area s which is L in length and d in width, with $d \to 0$.

Assuming a uniform electric field over the contour of integration, from the Fig. 5.1, (5.1) can be written as:

$$E_{r1}(t) - E_{r2}(t) = -\lim_{d\to 0}\left[\mu d\left(\frac{\partial H_{r1}(t)}{\partial t} - \frac{\partial H_{r2}(t)}{\partial t}\right)\right] \tag{5.2}$$

which further reduces to:

$$E_{r1}(t) = E_{r2}(t) \tag{5.3}$$

(5.3) can also be written as:

$$\hat{n}_z \times [\vec{E}_{r2}(t) - \vec{E}_{r1}(t)] = 0 \tag{5.4}$$

Similarly, the boundary condition on the magnetic field is given as [160]:

$$\oint_c \vec{H}\cdot\vec{dl} = \int_s\left(\vec{J} + \epsilon\frac{\partial\vec{E}}{\partial t}\right)\cdot\hat{n}_x ds \tag{5.5}$$

where s is W in length, d in width, and ϵ is the permittivity of the medium.. This surface of integration is orthogonal to the surface taken for the electric field integration in (5.1). From Fig. 5.1, (5.5) can be written as:

$$H_{r1}(t) + H_{r2}(t) = \lim_{d\to 0}\left[J_s(t) - d\left(\frac{\partial E_{r1}(t)}{\partial t} + \epsilon_s\frac{\partial E_{r2}(t)}{\partial t}\right)\right] \tag{5.6}$$

which further reduces to:

$$H_{r1}(t) + H_{r2}(t) = J_s(t) \tag{5.7}$$

$$\hat{n}_z \times [\vec{H}_{r2}(t) - \vec{H}_{r1}(t)] = \vec{J}_s(t) \tag{5.8}$$

In large aperture antennas, the radiated near-zone fields are related as [134, 161]:

$$\vec{H}_{r1}(t)\times\hat{n}_z = -\frac{\vec{E}_{r1}(t)}{\eta_0} \tag{5.9}$$

$$\vec{H}_{r2}(t)\times\hat{n}_z = \frac{\sqrt{\epsilon_r}\vec{E}_{r2}(t)}{\eta_0} \tag{5.10}$$

where η_0 is the wave impedance in medium 1 (air), and ϵ_r is the permittivity of the semiconductor substrate.

From (5.4) and (5.8)-(5.10), the radiated near-zone electric field can be expressed as a function of the surface current density as:

$$\vec{E}_{r2}(t) = \vec{E}_{r1}(t) = -\frac{\eta_0 \vec{J}_s(t)}{(1 + \sqrt{\epsilon_r})} \tag{5.11}$$

5.3 Semiconductor Carrier Dynamics

The photo-generated current density in the semiconductor material is computed using the continuity equation, including the carrier polarization, and the Drude-Lorentz theory of the semiconductors.

5.3.1 Carrier Densities

The carrier (electron & hole) concentrations in the active region of the photoconductive substrate follows the charge continuity equation given as [141, 142]:

$$\frac{dn(t)}{dt} = -\frac{n(t)}{\tau_n} + g(t) \tag{5.12}$$

$$\frac{dp(t)}{dt} = -\frac{p(t)}{\tau_p} + g(t) \tag{5.13}$$

where $n(t)$ and $p(t)$ are the time dependent densities of the electrons and the holes, respectively, τ_n and τ_p are the lifetime of the electrons and the holes, respectively, and $g(t)$ is the photo-carrier generation rate due to the laser impingement.

The photo-carrier generation rate can be written as:

$$g(t) = \frac{2\eta P(t,r)}{\pi\omega_0^2 h\nu_{opt}} \tag{5.14}$$

where η is the quantum efficiency of the semiconductor material, ω_0 is the laser beam waist radius at the interface, h is the Planck's constant, ν_{opt} is the laser frequency, and $P(t,r)$ is the total power absorbed by the semiconductor within the radius r.

The instantaneous power of a Gaussian laser beam is given as [152]:

$$P(t) = P_0 \, e^{\left(-\frac{2r^2}{\omega_0^2}\right)} e^{\left(-\frac{2t^2}{\tau_l^2}\right)} \tag{5.15}$$

where P_0 is the laser peak power and τ_l is the laser pulse width.

Including the laser penetration in the semiconductor material, the total power absorbed by the semiconductor material within the radius r is given as:

$$P(t,r) = \alpha(1-R)P_0 \left[1 - e^{\left(-\frac{2r^2}{\omega_0^2}\right)}\right] e^{\left(-\frac{2t^2}{\tau_l^2}\right)} e^{-\alpha z} \tag{5.16}$$

where α is the optical absorption coefficient of the semiconductor material, and R is the power reflection coefficient at the interface.

Using (5.12) and (5.13), the total number of the carriers within the active region can be written as:

$$n(t) = \frac{\eta(1-R)\tau_l P_0 WL}{\sqrt{2}\pi h\nu_{opt}\omega_0^2} \left[1 - e^{\left(-\frac{2r^2}{\omega_0^2}\right)}\right] \left[1 - e^{-\alpha l_n}\right] e^{\left(\frac{\tau_l^2}{8\tau_n^2} - \frac{t}{\tau_n}\right)} \left[1 + \mathrm{erf}\left(\frac{\sqrt{2}t}{\tau_l} - \frac{\sqrt{2}\tau_l}{4\tau_n}\right)\right] \tag{5.17}$$

where l_n is the diffusion length for the electrons and can be calculated from, $l_n = \sqrt{D_n\tau_n}$, and D_n is the diffusion coefficient of the electrons.

Similarly, the total number of the holes in the active region can be written as:

$$p(t) = \frac{\eta(1-R)\tau_l P_0 WL}{\sqrt{2}\pi h\nu_{opt}\omega_0^2} \left[1 - e^{\left(-\frac{2r^2}{\omega_0^2}\right)}\right] \left[1 - e^{(-\alpha l_p)}\right] e^{\left(\frac{\tau_l^2}{8\tau_p^2} - \frac{t}{\tau_p}\right)} \left[1 + \mathrm{erf}\left(\frac{\sqrt{2}t}{\tau_l} - \frac{\sqrt{2}\tau_l}{4\tau_p}\right)\right] \tag{5.18}$$

where l_p is the diffusion length for the holes and can be calculated from, $l_p = \sqrt{D_p\tau_p}$, and D_p is the diffusion coefficient of the holes.

The carriers within the volume corresponding to the diffusion length contribute towards the surface current while others remaining in the active region get recombine with the trap sites before reaching the surface. So, the average carrier densities are calculated for the volume corresponding to the diffusion lengths of the carriers and are given as:

$$n_{av}(t) = \frac{\eta(1-R)\tau_l P_0}{\sqrt{2}\pi h\nu_{opt}\omega_0^2 l_n} \left[1 - e^{\left(-\frac{2r^2}{\omega_0^2}\right)}\right] \left[1 - e^{(-\alpha l_n)}\right] e^{\left(\frac{\tau_l^2}{8\tau_n^2} - \frac{t}{\tau_n}\right)} \left[1 + \mathrm{erf}\left(\frac{\sqrt{2}t}{\tau_l} - \frac{\sqrt{2}\tau_l}{4\tau_n}\right)\right] \tag{5.19}$$

$$p_{av}(t) = \frac{\eta(1-R)\tau_l P_0}{\sqrt{2\pi} h\nu_{opt}\omega_0^2 l_p}\left[1 - e^{\left(-\frac{2r^2}{\omega_0^2}\right)}\right]\left[1 - e^{(-\alpha l_p)}\right] e^{\left(\frac{\tau_l^2}{8\tau_p^2} - \frac{t}{\tau_p}\right)}\left[1 + \mathrm{erf}\left(\frac{\sqrt{2}t}{\tau_l} - \frac{\sqrt{2}\tau_l}{4\tau_p}\right)\right] \tag{5.20}$$

5.3.2 Surface Current Density

The diffusion lengths of the carriers are very small compared to the gap dimensions. So, the current generated in the PCA can be assumed as the surface current. The total surface current density can computed by adding the current densities arising due to the electrons and the holes, given as:

$$J_s(t) = q\left[n_{av}(t)v_n(t)l_n + p_{av}(t)v_p(t)l_p\right] \tag{5.21}$$

where $v_n(t)$ and $v_p(t)$ are the velocities of the electrons and the holes, respectively.

5.3.3 Carrier Velocities

The time-dependent velocities of the carriers can be calculated by using the Drude-Lorentz theory of the carrier transport in the semiconductor material. The time-dependent velocities of the electrons and the holes can be written as:

$$\frac{dv_n(t)}{dt} = -\frac{v_n(t)}{\tau_{sn}} + \frac{qE_{net}(t)}{m_n^*} \tag{5.22}$$

where m_n^* is the effective mass of the electrons, τ_{sn} is the moment relaxation time of the electrons and can be calculated from, $\tau_{sn} = \frac{\mu_n m_n^*}{q}$, μ_n is the mobility of the electrons, and E_{net} is the net electric field across the electrodes gap.

$$\frac{dv_p(t)}{dt} = -\frac{v_p(t)}{\tau_{sp}} + \frac{qE_{net}(t)}{m_p^*} \tag{5.23}$$

where m_p^* is the effective mass of the holes, τ_{sp} is the moment relaxation time of the holes and can be calculated from, $\tau_{sp} = \frac{\mu_p m_p^*}{q}$, and μ_p is the mobility of the holes.

5.3.4 Net Electric Field

From the Fig. 5.1, the net electric field across the electrodes gap can be written as:

$$E_{net}(t) = E_{bias} - \frac{P_s(t)}{\zeta\epsilon_0\epsilon_r} - E_r(t) \tag{5.24}$$

where ζ is the is the geometrical factor and is equal to 3 for isotropic material [153], and E_r is the radiated near-zone electric field and can be computed using (5.11).

5.3.5 Carrier Polarization

The polarization of the carriers is given as [153]:

$$\frac{dP_s(t)}{dt} = -\frac{P_s(t)}{\tau_r} + J_s(t) \tag{5.25}$$

where τ_r is the carrier recombination time in pure semiconductor substrate.

5.3.6 Radiated THz Electric Field

The radiated THz electric field is proportional to the rate of change of the current density and can written as:

$$E_{THz}(t) \propto \frac{\partial J_s}{\partial t}$$

Using (5.21);

$$E_{THz}(t) \propto \left(q l_n \left[n_{av}(t)\frac{\partial v_n(t)}{\partial t} + v_n(t)\frac{\partial n_{av}(t)}{\partial t} \right] + q l_p \left[p_{av}(t)\frac{\partial v_p(t)}{\partial t} + v_p(t)\frac{\partial p_{av}(t)}{\partial t} \right] \right) \tag{5.26}$$

5.4 Results and Discussions

In this work, LT-GaAs is taken as the semiconductor substrate material for the PCA. The effective mass of the holes is almost seven times of the effective mass of the electrons in GaAs [162]. It is assumed that the same relation holds for the LT-GaAs. So, the mobility of the holes is considered to be almost one-seventh of the electrons. The trap density in LT-GaAs is very high which helps in reducing the lifetime of the carriers. The capturing time of the carriers by the trap sites situated at the mid-band energy levels is very small compared to the recombination time of the carriers. Hence, the average lifetime of the carriers is assumed to be equal to the its trapping time. The capturing time and the capture cross-section of the carriers are related as given by (3.9). The capturing time of the holes is assumed to be the three times of the electrons as the capture cross-section for the holes is very small compared to the electrons [163]. The value of the different parameters used in the calculations are given in Table 5.1 [76, 132, 164, 165].

Table 5.1: Parameters details for the near fields calculations

Parameter	Value
Power absorption coefficient (α)	6000 cm^{-1}
Semiconductor permittivity (ε_r)	12.9
Laser pulse width (τ_l)	250 fs
Laser repetition frequency (f_{rep})	1 KHz
Laser frequency (ν_{opt})	375 THz
Laser beam waist radius (ω_0)	L/2
Gap Width (W)	5 mm
Gap Length (L)	5 mm
Electrons lifetime (τ_n)	1 ps
Holes lifetime (τ_p)	3 ps
Carriers recombination time (τ_r)	100 ps
Electrons mobility (μ_e)	1500 cm^{2}V^{-1}s^{-1}
Holes mobility (μ_p)	210 cm^{2}V^{-1}s^{-1}
Electrons diffusion coefficient (D_n)	200 cm^{2}s^{-1}
Holes diffusion coefficient (D_p)	10 cm^{2}s^{-1}
Electrons effective mass (m_n^*)	0.067m_0
Holes effective mass (m_p^*)	0.47m_0
m_0	9.1×10^{-31} Kg
η	1

5.4.1 Effect of the Near-Zone Fields on the Net Electric Field

The radiation field comprises both the near and the far zone fields components. The orientation of the radiated near-zone electric field is such that it opposes the effect of the bias electric field and reduces the amplitude of the net electric field at the gap as in (6.32). The effect of the

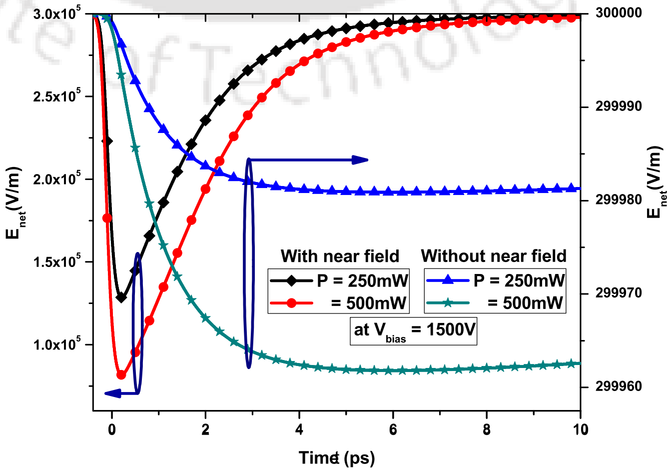

Fig. 5.2: Effect of the near-zone field on the net electric field

near-zone electric field on the net electric field at the gap is shown in Fig. 5.2. From Fig. 5.2, it can be seen that the transient behavior of the net electric field in both of the cases are different. Moreover, in the case of net electric field without considering the radiated near-zone electric field effect, the variation in the amplitude of the net electric field is negligibly small and is not restored back to its initial state after the disappearance of the carriers.

5.4.2 Effect of the Near-Zone Fields on the Carrier Velocities

It can be seen from (5.22) and (5.23) that the velocities of the electrons and the holes depend on the net electric field at the gap. As shown earlier, the near-zone electric field limits the amplitude of the net electric field, which results in reduced carrier velocities as shown in Figs. 5.3 and 5.4. As the consequence of the reduces carrier velocities, a small current pulse generated in the PCA.

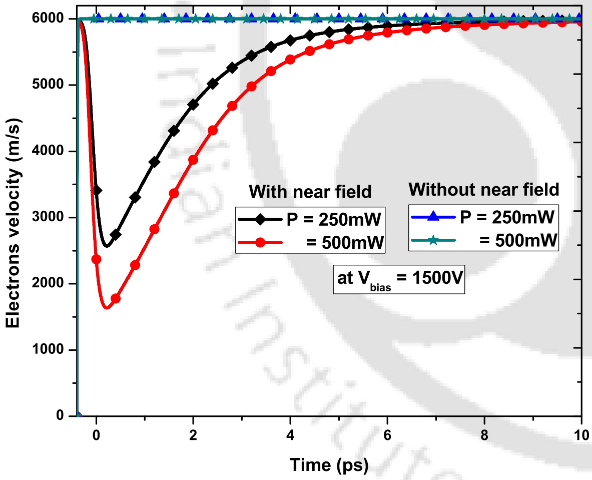

Fig. 5.3: Effect of the near zone field on the electrons velocity

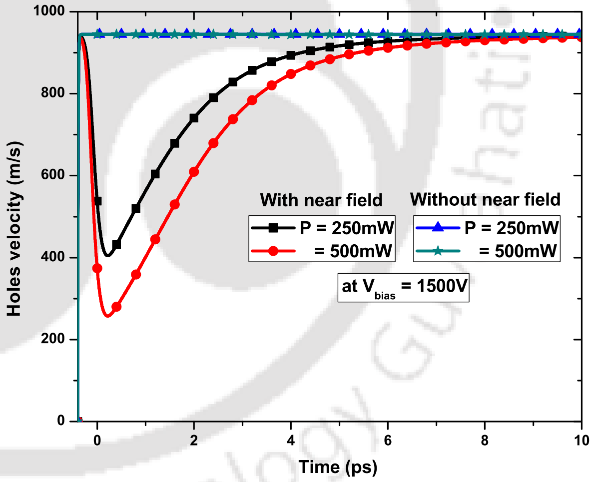

Fig. 5.4: Effect of the near zone field on the holes velocity

5.4.3 Effect of the Near-Zone Fields on the Current Density

Due to the reduction in the net electric field at the gap, the velocities of the carriers decrease as shown in Figs. 5.3 and 5.4, which results in a low current density at the gap. The effect of the near-zone electric field on the current density at the gap is shown in Fig. 5.5.

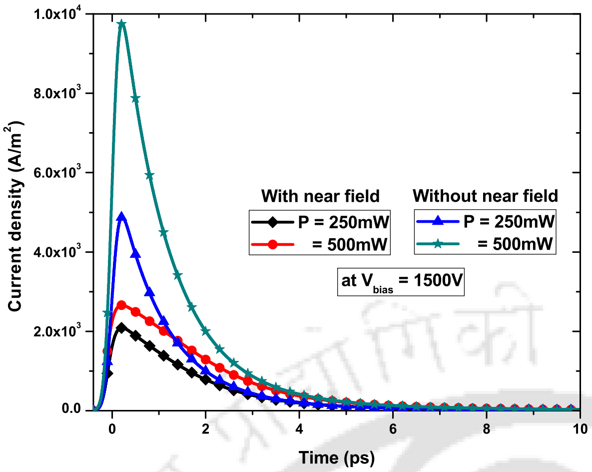

Fig. 5.5: Effect of the near zone field on the current density

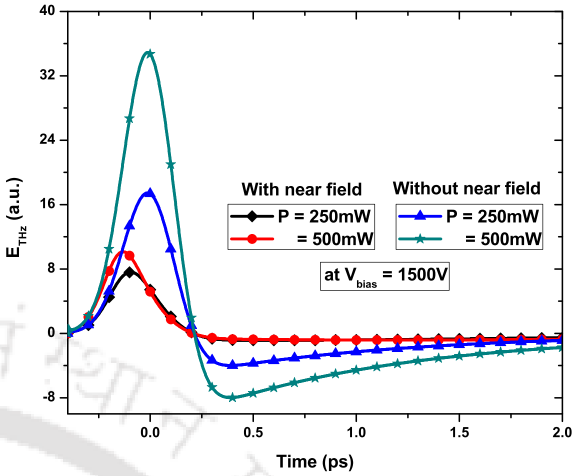

Fig. 5.6: Effect of the near zone field on the radiated far field

5.4.4 Effect of the Near-Zone Fields on the Radiated THz Electric Field

The reduced net electric field and the current density reduces the amplitude of the radiated THz electric field from the PCA. The effect of the near-zone electric field on the radiated far-zone electric field is shown in the Fig. 5.6. From the figure, it can be observed that the negative effect of the near-zone electric field on the radiated THz field increases with the laser power and become more prominent at higher values of the laser power.

5.4.5 Behavior of the Near-Zone Electric Field

The near-zone electric field depends on the current density generated at the gap in the PCA. The behavior of the near-zone electric field with V_{bias} and P is shown in Fig. 5.7. From the

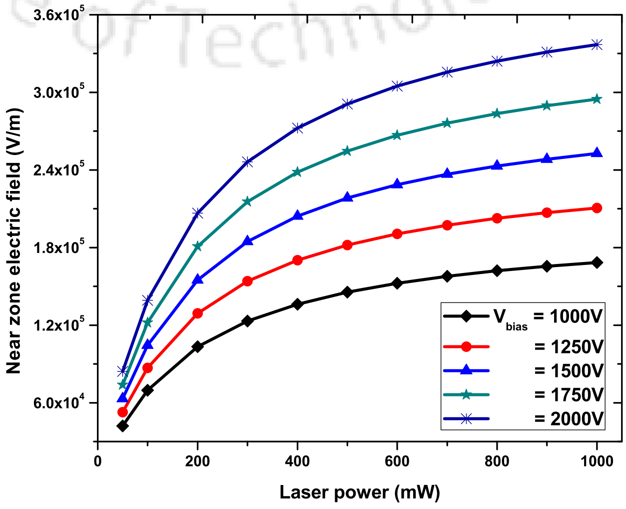

Fig. 5.7: The Near-zone electric field variation with V_{bias} and P

figure, it can be seen that the near-zone electric field amplitude increases with the voltage as well as with the laser power. However, the near zone electric field amplitude saturates at high laser power as shown in Fig. 5.7.

5.5 Summary

In this chapter, the effect of the radiated near-zone electric field on the performance of the LAPCA has been analyzed. The calculations show that the near-zone electric field limits the amplitude of the radiated THz electric field from the LAPCA. It also reduces the magnitude of other parameters too, such as the net electric field, current density, and carrier velocities. Although the near-zone electric field effect increases with the voltage and laser power, it saturates at the high laser powers. This study helps in understanding the reason behind the low efficiency of the PCA and is expected to be very useful in employing the techniques which can neutralize the effect of the near-zone electric field to improve its performance.

6

Magnetic Field-Assisted Radiation Enhancement from a Large Aperture Photoconductive Antenna

Contents

6.1 Introduction

In order to enhance the radiated power, it is imperative to counter the effect of the factors limiting the performance of a PCA. Changing the antenna geometry overcomes the problems arises due to voltage screening and carrier polarization. Similarly, using the large aperture PCAs (LAPCA) facilitate a high voltage biasing and enhance the output power from it. Although, these methods surely improves the radiated power from the PCA, the performance enhancement factor still remains very small. Apart from above said factors, the radiated electric field in the near zone also affect its performance as discussed in the chapter 5.

This chapter presents a novel method to study the effect of an external DC magnetic field on the performance of a LAPCA. Prior to this, to the best of the author's knowledge, there is no study available in the literature which deals with the same. The reduction in the amplitude of the current density due to the near-zone field effect can be overcome by using an external magnetic field, which also enhances the radiated power from the PCA. In order to analyze it numerically, the electromagnetic boundary conditions with the semiconductor carrier dynamics are employed. The semiconductor carrier dynamics model presented in this chapter incorporates the effect of antenna geometry, the carrier lifetime, space-charge polarization, transient mobilities, and the radiated near-zone fields on the behavior of the carriers dynamics in the semiconductor substrate. The effect of the external magnetic field on the current density, the amplitude and the polarity of the radiated far-zone electric field is computed and presented. The effect of the external magnetic field applied at an angle to the PCA is also analyzed and discussed. To verify the proposed theory, several results, in the absence of the external magnetic field, have been compared with the available experimental results in the literature.

6.2 Boundary Conditions

The distribution of the fields at the air-semiconductor interface are shown in Fig. 6.1. The external static magnetic field is applied along the positive direction of the y axis. The orientation of the radiated near-zone fields has been calculated using the current flow and wave propagation direction. The different fields shown in the Fig. 6.1, are as follows:

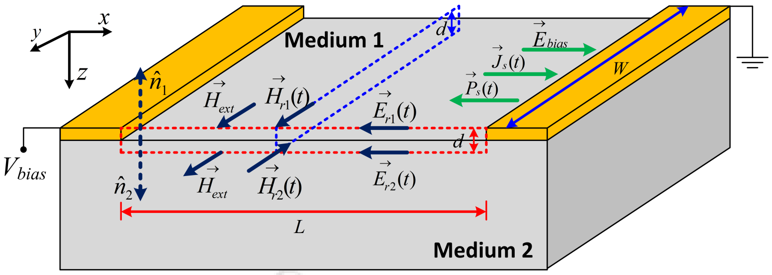

Fig. 6.1: The different fields orientation in a LAPCA

- E_{bias}: Field due to the applied bias voltage.
- J_s: Surface current density at the electrodes gap.
- P_s: Polarization due to the applied electric field.
- E_{r1}: The radiated near-zone electric field in the medium 1.
- H_{r1}: The radiated near-zone magnetic field in the medium 1.
- E_{r2}: The radiated near-zone electric field in the medium 2.
- H_{r2}: The radiated near-zone magnetic field in the medium 2.
- H_{ext}: The external static magnetic field.
- $\hat{n}_1$: Unit vector along the wave propagation direction in medium 1.
- $\hat{n}_2$: Unit vector along the wave propagation direction in medium 2.

where the medium 1 and medium 2 are air and semiconductor substrate, respectively. The gap dimensions are L in length and W in width. As the radiated waves propagate along z-axis, unit vector $\hat{n}_z$ is used to show the direction of the wave propagation.

The radiated far-zone electric field from a PCA depends on the photo-generated current density at the gap. The photo-generated current density at the gap depends on various parameters related to the PCA. The characteristics of the current density at the gap strongly rely on the net electric field at the gap. From Fig. 6.1, the net electric field comprises of the dc bias electric field, the radiated near-zone electric field, and the field associated with the polarization of the carriers. The relation between the radiated near-zone fields and the current density is calculated by applying the boundary conditions at the air–semiconductor interface.

At the gap of the electrodes, a uniform laser illumination is assumed while analyzing the behavior of the PCA. Due to the uniform carrier generation by the laser beam, the surface diffusion currents (along the x-axis and the y-axis) become zero. Moreover, the laser beam is assumed to be linearly polarized along the y-axis, so that it does not interfere with the net electric field along the x-axis at the gap.

The integral form of Maxwell's equation as given in (6.1) is considered and the boundary conditions on the magnetic field as in [160] are applied:

$$\oint_c \vec{H} \cdot \vec{dl} = \int_s \left(\vec{J} + \epsilon \frac{\partial \vec{E}}{\partial t} \right) \cdot \hat{n}_x ds \tag{6.1}$$

where the surface area (s) enclosed by the close line of the integral (c) is W (width of the electrodes) in length and d in width with $d \rightarrow 0$, $\vec{J}$ is the volume current density, and ϵ is the permittivity of the medium.

With reference to Fig. 6.1, (6.1) can be written as:

$$H_{net1}(t) + H_{net2}(t) = d\left\{ J(t) - \frac{\partial}{\partial t}\left[E_1(t) + \epsilon_r E_2(t)\right] \right\} \tag{6.2}$$

where ϵ_r is the permittivity of the medium 2.

The above equation reduces to:

$$H_{net1}(t) + H_{net2}(t) = J_s(t) \tag{6.3}$$

where J_s is the surface current density at the gap.

(6.3) can be written same as the steady state boundary condition as:

$$\hat{n}_z \times \left[\vec{H}_{net2}(t) - \vec{H}_{net1}(t) \right] = \vec{J}_s(t) \tag{6.4}$$

where

$$\vec{H}_{net1}(t) = \vec{H}_{r1}(t) + \vec{H}_{ext} \tag{6.5}$$

$$\vec{H}_{net2}(t) = \vec{H}_{r2}(t) - \vec{H}_{ext} \tag{6.6}$$

$$\hat{n}_z \times \left[\vec{H}_{r2}(t) - \vec{H}_{r1}(t) \right] = \vec{J}_s(t) + 2\hat{n}_z \times \vec{H}_{ext} \tag{6.7}$$

Similarly, the boundary conditions are applied to the (6.8) [160]:

$$\oint_c \vec{E} \cdot \vec{dl} = -\int_s \mu \frac{\partial \vec{H}}{\partial t} \cdot \hat{n}_y ds \tag{6.8}$$

where the area (s) enclosed by the close line of integral (c) is L (gap length between the electrodes) in length and d in width with $d \rightarrow 0$.

Assuming a uniform electric field over the gap length, (6.8) can be written as:

$$E_{r1}(t) - E_{r2}(t) = -\lim_{d\to 0}\left(\mu d \frac{\partial}{\partial t}\left[H_{net1}(t) - H_{net2}(t)\right]\right) \tag{6.9}$$

The above equation reduces to:

$$E_{r1}(t) = E_{r2}(t) \tag{6.10}$$

(6.10) can be written same as the steady state boundary condition as:

$$\hat{n}_z \times \left[\vec{E}_{r2}(t) - \vec{E}_{r1}(t)\right] = 0 \tag{6.11}$$

In large aperture antennas, the transient electric and magnetic fields in the near-zone [134, 161] are related as:

$$\vec{H}_{r1}(t) \times \hat{n}_z = -\frac{\vec{E}_{r1}(t)}{\eta_0} \tag{6.12}$$

$$\vec{H}_{r2}(t) \times \hat{n}_z = \frac{\sqrt{\epsilon_r}\vec{E}_{r2}(t)}{\eta_0} \tag{6.13}$$

where η_0 is the wave impedance in medium 1, and ϵ_r is the permittivity of the semiconductor substrate.

From (6.7) and (6.11)-(6.13), the radiated near-zone electric field can be expressed as a function of the surface current density and the external magnetic field, given as:

$$\vec{E}_{r2}(t) = \vec{E}_{r1}(t) = -\left(\frac{\eta_0}{1 + \sqrt{\epsilon_r}}\right)\left[\vec{J}_s(t) + 2\hat{n}_z \times \vec{H}_{ext}\right] \tag{6.14}$$

6.3 Semiconductor Carrier Dynamics Model

In this section, with some modifications, the same carrier dynamics model as presented in section 5.3 is used to evaluate the behavior of different parameters. It incorporates the effect of carrier concentration, carrier polarization, transient mobil1ities, and the transient velocity of the carriers. Additionally, the effect of the external magnetic field on the different parameters of the PCA is incorporated in the carrier dynamics.

6.3.1 Carrier Densities

The time-dependent carrier densities in the PCA are computed by using the generation and recombination rate of the carriers, also known as the continuity equation, and are given as [141, 142]:

$$\frac{dn(t)}{dt} = -\frac{n(t)}{\tau_n} + g(t) \tag{6.15}$$

$$\frac{dp(t)}{dt} = -\frac{p(t)}{\tau_p} + g(t) \tag{6.16}$$

where n and p are the electrons and the holes densities, respectively, τ_n and τ_p are the lifetime of the electrons and the holes, respectively, and $g(t)$ is the photo-carrier generation rate due to laser impingement and can be written as:

$$g(t) = \frac{2\eta P(t,r)}{\pi\omega_0^2 h\nu_{opt}} \tag{6.17}$$

where η is the quantum efficiency of the semiconductor material, ω_0 is the laser beam waist radius at the interface, h is the Planck's constant, ν_{opt} is the laser frequency, and $P(t,r)$ is the total power absorbed by the semiconductor material within the radius r.

The total power absorbed by the semiconductor material within the radius r and including the laser penetration in the semiconductor material is given as:

$$P(t,r) = \alpha(1-R)P_0\left[1 - e^{\left(-\frac{2r^2}{\omega_0^2}\right)}\right] e^{\left(-\frac{2t^2}{\tau_l^2}\right)} e^{(-\alpha z)} \tag{6.18}$$

where α is the optical absorption coefficient of the semiconductor material, R is the power reflection coefficient at the interface, P_0 is the laser peak power, and τ_l is the laser pulsewidth.

The solution of (6.15) and (6.16) can be written as:

$$n(t) = \frac{\eta(1-R)\tau_l P_0}{\sqrt{2\pi} h\nu_{opt}\omega_0^2}\left[1 - e^{\left(-\frac{2r^2}{\omega_0^2}\right)}\right]\left(1 - e^{(-\alpha l_n)}\right) e^{\left(\frac{\tau_l^2}{8\tau_n^2} - \frac{t}{\tau_n}\right)}\left[1 + \mathrm{erf}\left(\frac{\sqrt{2}t}{\tau_l} - \frac{\sqrt{2}\tau_l}{4\tau_n}\right)\right] \tag{6.19}$$

where l_n is the diffusion length for the electrons and can be calculated from, $l_n = \sqrt{k_B T \mu_n \tau_n / q}$,

k_B is Boltzmann constant, T is the temperature, and μ_n is the mobility of the electrons.

$$p(t) = \frac{\eta(1-R)\tau_l P_0}{\sqrt{2\pi} h\nu_{opt}\omega_0^2}\left[1 - e^{\left(-\frac{2r^2}{\omega_0^2}\right)}\right]\left(1 - e^{(-\alpha l_p)}\right) e^{\left(\frac{\tau_l^2}{8\tau_p^2} - \frac{t}{\tau_p}\right)}\left[1 + \operatorname{erf}\left(\frac{\sqrt{2}t}{\tau_l} - \frac{\sqrt{2}\tau_l}{4\tau_p}\right)\right] \tag{6.20}$$

where l_p is the diffusion length for the holes and can be calculated from, $l_p = \sqrt{k_B T \mu_p \tau_p / q}$, and μ_p is the mobility of the holes.

The average carrier densities of the electrons and holes can be given as:

$$n_{av}(t) = \frac{\eta(1-R)\tau_l P_0}{\sqrt{2\pi} h\nu_{opt}\omega_0^2 l_n}\left[1 - e^{\left(-\frac{2r^2}{\omega_0^2}\right)}\right]\left(1 - e^{(-\alpha l_n)}\right) e^{\left(\frac{\tau_l^2}{8\tau_n^2} - \frac{t}{\tau_n}\right)}\left[1 + \operatorname{erf}\left(\frac{\sqrt{2}t}{\tau_l} - \frac{\sqrt{2}\tau_l}{4\tau_n}\right)\right] \tag{6.21}$$

$$p_{av}(t) = \frac{\eta(1-R)\tau_l P_0}{\sqrt{2\pi} h\nu_{opt}\omega_0^2 l_p}\left[1 - e^{\left(-\frac{2r^2}{\omega_0^2}\right)}\right]\left(1 - e^{(-\alpha l_p)}\right) e^{\left(\frac{\tau_l^2}{8\tau_p^2} - \frac{t}{\tau_p}\right)}\left[1 + \operatorname{erf}\left(\frac{\sqrt{2}t}{\tau_l} - \frac{\sqrt{2}\tau_l}{4\tau_p}\right)\right] \tag{6.22}$$

To calculate the average carrier densities, the volume corresponding to the carrier diffusion lengths are used because only the carriers within this volume contribute to the surface current density, while others get recombined before reaching the surface.

6.3.2 Optical Absorption Coefficient

The optical absorption coefficient of the semiconductor material changes due to the bandfilling effect by the rapid generation of the carriers at the surface [166]. For an n-type semiconductor, the bandfilling effect on the optical absorption coefficient is modeled as:

$$\alpha = \alpha_0 - \Delta\alpha(n_{av}, p_{av}, E) \tag{6.23}$$

$$\begin{aligned}\Delta\alpha(n_{av}, p_{av}, E) = {} & \frac{C_{hh}}{E}\sqrt{E - E_g}\left[1 - f_v(E_{ah}) + f_c(E_{bh})\right] \\ & + \frac{C_{lh}}{E}\sqrt{E - E_g}\left[1 - f_v(E_{al}) + f_c(E_{bl})\right]\end{aligned} \tag{6.24}$$

$$f_v(E_{ah,al}) = \left[1 + e^{\left(\frac{E_{ah,al} - E_{FV}}{k_B T}\right)}\right]^{-1} \tag{6.25}$$

$$f_c(E_{bh,bl}) = \left[1 + e^{\left(\frac{E_{bh,bl} - E_{FC}}{k_B T}\right)}\right]^{-1} \tag{6.26}$$

$$E_{ah,al} = \left(E_g - E\right)\left[\frac{m_e}{m_e + m_{hh,lh}}\right] - E_g \tag{6.27}$$

$$E_{bh,bl} = \left(E - E_g\right)\left[\frac{m_{hh,lh}}{m_e + m_{hh,lh}}\right] \tag{6.28}$$

$$E_{FC} = \left\{\ln\left(\frac{n_{av}}{N_c}\right) + \left(\frac{n_{av}}{N_c}\right)\left[64 + 0.05524\frac{n_{av}}{N_c}\left\{64 + \sqrt{\frac{n_{av}}{N_c}}\right\}\right]^{-1/4}\right\} k_B T \tag{6.29}$$

$$E_{FV} = \left(-\left\{\ln\left(\frac{p_{av}}{N_v}\right) + \left(\frac{p_{av}}{N_v}\right)\left[64 + 0.05524\frac{p_{av}}{N_v}\left\{64 + \sqrt{\frac{p_{av}}{N_v}}\right\}\right]^{-1/4}\right\} - E_g\right) k_B T \tag{6.30}$$

where α_0 is the optical absorption constant of the semiconductor material for the photon energy E, and E_g is the semiconductor bandgap energy.

The change in the absorption coefficient induces a change in the dielectric constant value of the semiconductor material. However, the change in the value of the dielectric constant is very small and has been neglected.

6.3.3 Current Density

The total surface current density can be given by adding the current densities due to the electrons and the holes, written as:

$$J_s(t) = q\left[n_{av}(t)v_n(t)l_n + p_{av}(t)v_p(t)l_p\right] \tag{6.31}$$

where $v_n(t)$, $v_p(t)$ are the transient velocities of the electrons and the holes, respectively.

6.3.4 Net Electric Field

The net electric field across the electrodes gap, from the Fig. 6.1, can be written as:

$$E_{net}(t) = E_{bias} - \frac{P_s(t)}{\zeta\epsilon_0\epsilon_r} - E_r(t) \tag{6.32}$$

where ζ is the is the geometrical factor and is equal to 3 for the isotropic materiasl [153], and E_r is the radiated near-zone electric field and can be computed from (6.14).

6.3.5 Carrier Polarization

The time dependent polarization [153] due to the separation between the carriers caused by the bias electric field is given by:

$$\frac{dP_s(t)}{dt} = -\frac{P_s(t)}{\tau_r} + J_s(t) \tag{6.33}$$

where τ_r is the recombination time of the electrons with the holes in LT-GaAs.

6.3.6 Carrier Velocities

To calculate the transient velocities of the carriers, Caughey Thomas [145] and Arora [146] mobility models are used to incorporate the electric field and the carrier density dependence of the carrier mobility as explained in section 3.2.6. The doping dependent mobilities of the carriers are given as [141, 146]:

$$\mu_{dop,n}(t) = \mu_{low,n} + \mu_{d,n}\left[1 + \left(\frac{n_{av}(t)}{n_0}\right)^{0.6273}\right]^{-1} \tag{6.34}$$

$$\mu_{dop,p}(t) = \mu_{low,p} + \mu_{d,p}\left[1 + \left(\frac{p_{av}(t)}{p_0}\right)^{0.8057}\right]^{-1} \tag{6.35}$$

where $\mu_{low,n}$ and $\mu_{low,p}$ are the low field mobilities of the electrons and the holes, respectively and $\mu_{d,n}$ and $\mu_{d,p}$ are the differences between the highest and the lowest values of the mobilities of the electrons and the holes, respectively. The field dependent carrier mobilities are given as [141, 145]:

$$\mu_{elec,n}(t) = \mu_{low,n}\left[1 + \left(\frac{\mu_{low,n}E_{net}(t)}{v_{sat,e}}\right)^2\right]^{-1/2} \tag{6.36}$$

$$\mu_{elec,p}(t) = \mu_{low,p}\left[1 + \left(\frac{\mu_{low,p}E_{net}(t)}{v_{sat,p}}\right)^2\right]^{-1/2} \tag{6.37}$$

The effective mobilities μ_n and μ_p of the electrons and the holes, respectively, are given as:

$$\mu_n(t) = \frac{\mu_{elec,n}(t)\mu_{dop,n}(t)}{\mu_{elec,n}(t) + \mu_{dop,n}(t)} \tag{6.38}$$

$$\mu_p(t) = \frac{\mu_{elec,p}(t)\mu_{dop,p}(t)}{\mu_{elec,p}(t) + \mu_{dop,p}(t)} \tag{6.39}$$

Using the transient mobilities, the transient velocities of the carriers at the gap are given as:

$$v_n(t) = \mu_n(t)E_{net}(t) \tag{6.40}$$

$$v_p(t) = \mu_p(t)E_{net}(t) \tag{6.41}$$

The movement of the carriers get affected due to the applied magnetic field. A y-axis oriented external magnetic field changes the carrier's movement from x-axis towards the z-axis thereby changing the carrier densities. The increment or reduction in the carrier density depends on the orientation of the external magnetic field (positive or negative direction of the y-axis). The magnetic field-dependent carrier velocities are computed using the following equations:

$$\frac{dv_{pz}(t)}{dt} = -\frac{v_{pz}(t)}{\tau_{sp}} + \frac{q}{m_p^*}v_p(t)B_{ext} \tag{6.42}$$

$$\frac{dv_{nz}(t)}{dt} = -\frac{v_{nz}(t)}{\tau_{sn}} + \frac{q}{m_n^*}v_n(t)B_{ext} \tag{6.43}$$

where B_{ext} is the external magnetic flux density, m_n^* and m_p^* are the effective mass of the electrons and the holes, respectively, and $\tau_{sn,sp}$ are the moment relaxation time of the electrons and the holes, respectively. The moment relaxation time can be calculated from $\tau_{sn,sp} = \frac{\mu_{n,p}m_{n,p}^*}{q}$.

The distance covered by the carriers along the z-axis in the small time step dt is calculated as:

$$l_{nz,pz} = v_{nz,pz}dt \tag{6.44}$$

6.3.7 Effect of the Magnetic Field of the Carrier Densities

Including the effect of the external magnetic field on the carrier velocities, the changed average volume carrier densities are computed as:

$$n_{av}(t) = \frac{\eta(1-R)\tau_l P_0}{\sqrt{2\pi}h\nu_{opt}\omega_0^2 l_n}\left[1 - e^{\left(-\frac{2r^2}{\omega_0^2}\right)}\right]\left(1 - e^{(-\alpha[l_n + l_{nz}])}\right)e^{\left(\frac{\tau_l^2}{8\tau_n^2} - \frac{t}{\tau_n}\right)}\left[1 + \mathrm{erf}\left(\frac{\sqrt{2}t}{\tau_l} - \frac{\sqrt{2}\tau_l}{4\tau_n}\right)\right] \tag{6.45}$$

$$p_{av}(t) = \frac{\eta(1-R)\tau_l P_0}{\sqrt{2\pi}h\nu_{opt}\omega_0^2 l_p}\left[1 - e^{\left(-\frac{2r^2}{\omega_0^2}\right)}\right]\left(1 - e^{(-\alpha[l_p + l_{pz}])}\right)e^{\left(\frac{\tau_l^2}{8\tau_p^2} - \frac{t}{\tau_p}\right)}\left[1 + \mathrm{erf}\left(\frac{\sqrt{2}t}{\tau_l} - \frac{\sqrt{2}\tau_l}{4\tau_p}\right)\right] \tag{6.46}$$

When an external magnetic field is applied along the positive direction of the y-axis, l_{nz} and l_{pz} have positive and negative values, respectively. While for the negative direction of the y-axis applied magnetic field, l_{nz} and l_{pz} have negative and positive values, respectively.

6.3.8 Radiated THz Electric Field

The amplitude of the radiated far-zone THz electric field is proportional to the rate of change of the current density and is given as [82]:

$$E_{THz}(t) \cong \frac{A}{4\pi\varepsilon_0 c_l^2 z_d}\frac{\partial J_s(t)}{\partial t} \tag{6.47}$$

where A is the gap area, c_l is the speed of light and z_d is the measurement point distance.

Using (6.31), (6.47) can be written as:

$$E_{THz}(t) \cong \frac{A}{4\pi\varepsilon_0 c_l^2 z_d}\left(ql_n\left[n_{av}(t)\frac{\partial v_n(t)}{\partial t} + v_n(t)\frac{\partial n_{av}(t)}{\partial t}\right] + ql_p\left[p_{av}(t)\frac{\partial v_p(t)}{\partial t} + v_p(t)\frac{\partial p_{av}(t)}{\partial t}\right]\right) \tag{6.48}$$

6.4 Results and Discussions

The analytical results obtained for an external magnetic field effect on a LAPCA could not be compared readily with the experimental results as such results are not available in the literature. However, to substantiate the proposed theory, the results computed in the absence of the external magnetic field are compared with the available experimental results in the literature. It should be noted that the results reported in the literature are given in arbitrary units without any information about the distances at which the measurements of the THz signal is taken. So, instead of a direct comparison, a behavioral comparison of the results is presented. The different parameters and measurement distances are chosen such that the analytical results closely follow the experimental results.

In this study the LT-GaAs material is considered for the semiconductor substrate in the LAPCA. Same as the chapter 5, the mobility of the holes is assumed to be almost one-seventh of the electrons. Also, the capturing time of the holes is considered to be the three times of the electrons as the capture cross-section for the holes is very small compared to the electrons.

Table 6.1: Parameters value used in the calculations

Parameter	**Value**	**Parameter**	**Value**
α_0	6000 cm^{-1}	W	200 μm
ν_{opt}	375 THz	L	200 μm
ε_r	12.9	ω_0	0.707×gap width
τ_l	100 fs	$\mu_{low,n}$	200 $\text{cm}^2\text{V}^{-1}\text{s}^{-1}$
τ_n	1 ps	$\mu_{low,p}$	40 $\text{cm}^2\text{V}^{-1}\text{s}^{-1}$
n_0	1×10^{20} m^3	$\mu_{d,n}$	8300 $\text{cm}^2\text{V}^{-1}\text{s}^{-1}$
p_0	1×10^{21} m^3	$\mu_{d,p}$	360 $\text{cm}^2\text{V}^{-1}\text{s}^{-1}$
τ_p	3 ps	τ_r	100 ps
m_0	9.1×10^{-31} Kg	m_p^*	$0.47\times m_0$
m_n^*	$0.067\times m_0$	f_{rep}	250 KHz
η	1	$v_{sat}^{n,p}$	1.13×10^5 m s^{-1}
z_d	10 cm	r	0.5×gap width
C_{hh}	1.5×10^{14} m $\text{s}^{-1/2}$	C_{lh}	7.8×10^{13} m $\text{s}^{-1/2}$
m_{hh}	$0.45\times m_0$	m_{lh}	$0.084\times m_0$
m_e	$0.066\times m_0$	E_g	1.42 eV
N_c	$4.3\times10^{23}\text{m}^{-3}$	N_v	$8.3\times10^{24}\text{m}^{-3}$

The different semiconductor losses such as carrier-to-carrier collision, thermal and electrical are assumed to be negligibly small and neglected in the calculations. The values of different parameters used in the calculations are based on [76, 132, 141, 165–167] and given in Table 6.1.

6.4.1 In the Absence of the External Magnetic Field

From (6.32), it can be said that the net electric field characteristics depend on the bias field, the near-zone electric field, and the field associated with the polarization of the carriers (E_{pol}) given as:

$$E_{pol}(t) = \frac{P_c(t)}{\kappa\epsilon_0\epsilon_r} \tag{6.49}$$

The transient behaviors of the net electric field with the laser pulse, the polarization field, and the radiated near-zone field are shown in Fig. 6.2. From the figure, it is evident that the radiated near-zone electric field mainly causes the reduction in the amplitude of the net electric field.

The amplitude of the radiated far-zone field from a PCA depends on the parameters related to the laser beam, the photoconductive semiconductor material, and the printed antenna geom-

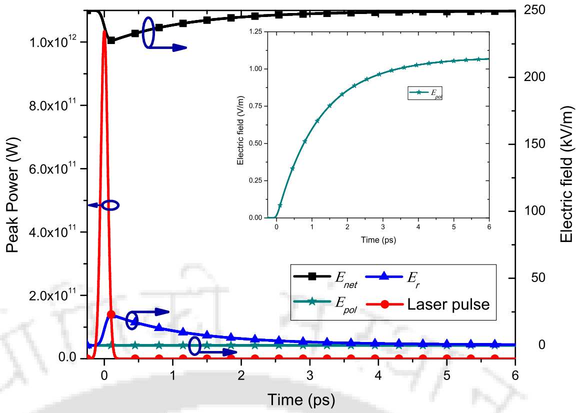

Fig. 6.2: Transient behavior of laser pulse, E_{net}, electric field due to polarization (E_{pol}), and E_r at V_{bias}=50 V and P=100 mW. The inset figure shows the zoomed view of E_{pol}

etry. To increase the amplitude of the far-zone field, an optimization of the values of these parameters or an optimized combination of the parameters is required. It can be seen in (6.48) that the amplitude of the radiated far-zone electric field depends on the rate of change of the carrier velocities and the carrier densities. The carrier densities mainly depend on the laser beam power, while the carrier velocities on the bias electric field. Thus, varying the laser beam power and the applied bias voltage (within the limit of the thermal and the electrical breakdown, respectively), the amplitude of the radiated far-zone electric field can be improved as shown in Fig. 6.3.

The analytically calculated results of the effect of voltage and laser power on the far-zone electric field are compared with the results from [168] & [169], respectively, and shown in Figs. 6.4 & 6.5. The values of different parameters used for the comparison study are given in Table 6.2 and 6.3.

Table 6.2: Parameters Details for Fig. 6.4

Parameter	Value	Parameter	Value
L	100 μm [168]	W	100 μm [168]
f_{rep}	75 MHz [168]	λ	800 nm [168]
τ_l	150 fs [168]	z_d	3.5 cm
P	90 mW		
Values of other parameters have been taken from Table 6.1			

The dimension of the gap between the electrodes and the net electric field across it affect the photo-generated carriers density in the PCA. Since the far-zone electric field amplitude is

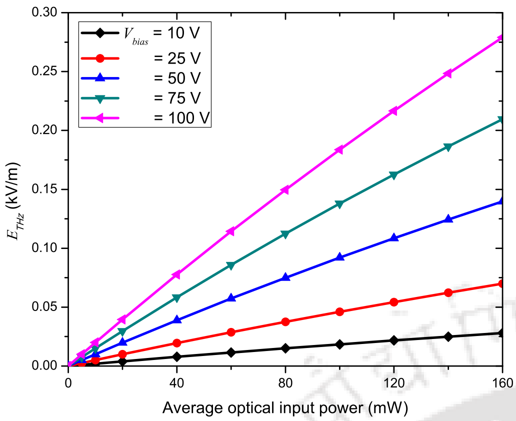

Fig. 6.3: Radiated far-zone electric field at different laser input power and DC bias voltage

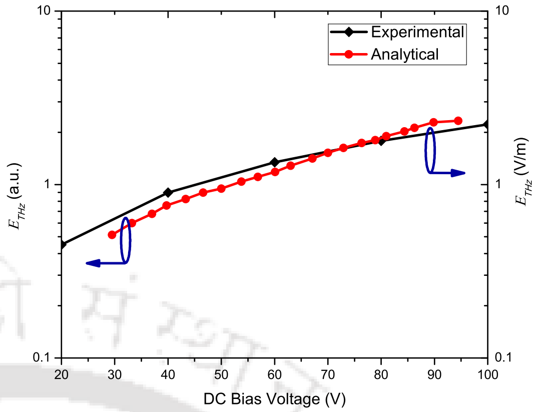

Fig. 6.4: Comparison of the analytical and the experimental [168] results of the bias voltage effect on the radiated far-zone electric field

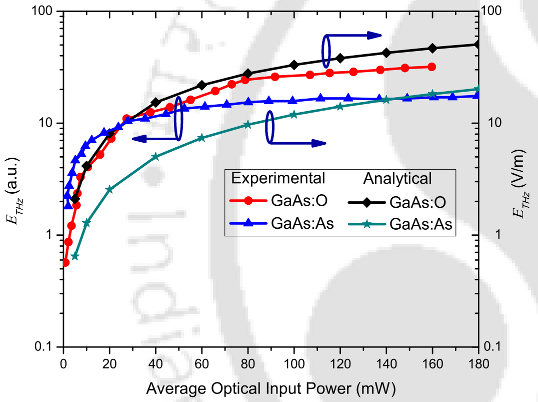

Fig. 6.5: Comparison of the analytical and the experimental [169] results of the laser input power effect on the radiated far-zone electric field

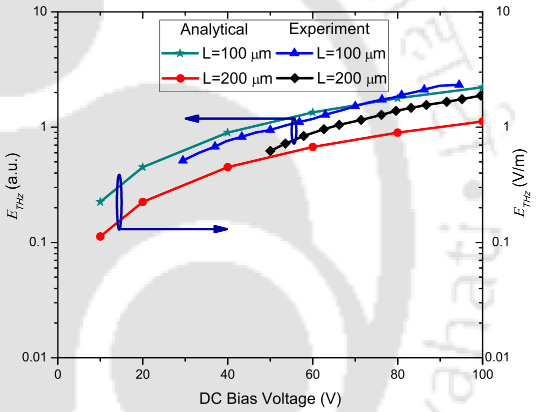

Fig. 6.6: Comparison of the analytical and the experimental [168] results of the gap length effect on the radiated far-zone electric field

Table 6.3: Parameters Details for Fig. 6.5

Parameter	Value	Parameter	Value
V_{bias} (GaAs:O)	100 V [169]	V_{bias} (GaAs:As)	110 V [169]
L	120 μm [169]	W	10 μm [169]
ω_0	5 μm [169]	f_{rep}	82 MHz [169]
τ_l	100 fs [169]	λ	760 nm [169]
τ_n	0.15 ps	z_d	8 cm
$\mu_{low,n}$ (GaAs:O)	500 cm^{2}V^{-1}s^{-1}	$\mu_{low,n}$ (GaAs:As)	200 cm^{2}V^{-1}s^{-1}
$\mu_{low,p}$ (GaAs:O)	100 cm^{2}V^{-1}s^{-1}	$\mu_{low,p}$ (GaAs:As)	40 cm^{2}V^{-1}s^{-1}
Values of other parameters have been taken from Table 6.1			

proportional to the rate of change of the current density, the parameters which effect the current density also influence the far-zone electric field. Thus, by changing the gap dimensions, the amplitude of the radiated far-zone electric field can be enhanced. Reducing the gap length increases the net electric field and the current density which effectively enhances the amplitude of the far-zone electric field. The result of the gap length effect is compared with the experimental result reported in [168] as shown in Fig. 6.6. The values of different parameters used in the calculations are given in Table 6.4.

Table 6.4: Parameters Details for Fig. 6.6

For $L = W$=100 μm and $L = W$=200 μm			
Parameter	**Value**	**Parameter**	**Value**
f_{rep}	75 MHz [168]	λ	800 nm [168]
τ_l	150 fs [168]	z_d	3.5 cm
Values of other parameters have been taken from Table 6.1			

From (6.15) & (6.16), it can be said that the rate of change of the carrier densities mainly depends on the carrier lifetime. A small carrier lifetime supports a fast rate of change, whereas a large value gives a slow rate of change. For the THz frequency generation from the PCA, a fast rate of change of the carrier densities is required which is supported by the small carrier lifetime. However, a small carrier lifetime provides a low current density compared to the larger values of the carrier lifetime, as the carriers remain available for a very short time to be collected at the electrodes. Increasing the carrier lifetime increases the availability period of the carriers at the gap, which supports a high current density and results in a intense radiation. The analytically calculated results of the carrier lifetime effect are compared with the results from [164] and shown in Fig. 6.7. The parameters values used in the analytical calculations are provided in Table 6.5.

Table 6.5: Parameters Details for Fig. 6.7

For τ_e=0.7 ps and 1.2 ps			
Parameter	**Value**	**Parameter**	**Value**
V_{bias}	1500 V [164]	L	5 mm [164]
W	5 mm [164]	ω_0	4 mm [164]
f_{rep}	1 kHz [164]	$\mu_{low,n}$	1500 cm^{2}V^{-1}s^{-1} [164]
τ_l	200 fs [164]	$\mu_{low,p}$	500 cm^{2}V^{-1}s^{-1}
λ	800 nm	z_d	18 cm
Values of other parameters have been taken from Table 6.1			

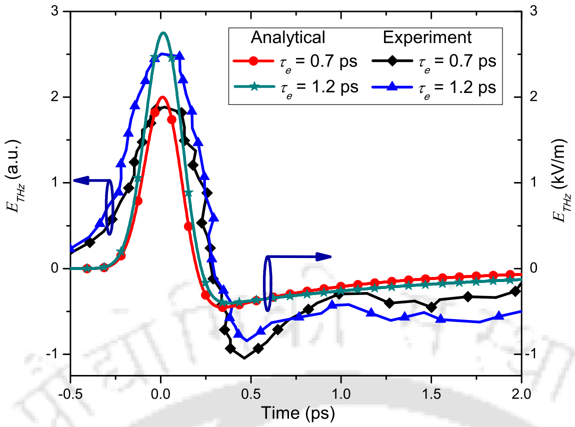

Fig. 6.7: Comparison of the analytical and the experimental [164] results of the carrier lifetime effect on the radiated far-zone electric field

6.4.2 In the Presence of the External Magnetic Field

From (6.31), (7.62) and (7.63), it can be seen that the current density strongly relies on the net electric field at the gap. The field associated with the polarization of the carriers and the near-zone electric field are oriented in such a way that they oppose the effect of the applied bias field and reduces the amplitude of the net electric field as given by (6.32). A high amplitude of the net electric field provides a high current density resulting in an intense radiation from the PCA. From (6.14) shows the relation of the near-zone field with the external magnetic field. From (6.14) and (6.32) show that the net electric field can be increased by the applied external magnetic field thereby increasing the current density. The effect of the applied magnetic field on the current density is shown in Fig. 6.8.

The application of the external magnetic field along the positive direction of the y-axis reduces the amplitude of the near-zone electric field as given in (6.14), which results in an increased current density. At the same time, it also changes the carrier's movement from the x-axis towards the z-axis direction(toward the surface of the semiconductor) thereby increasing the carrier densities as given by (6.45) and (6.46), which results in a high surface current density. However, it has been observed that the contribution to the current density from the change in carrier movement is negligibly small compared with the contribution of the reduction in the radiated near-zone electric field as shown in Fig. 6.9.

The effect of the external magnetic field on the carrier dynamics and the radiated far-zone

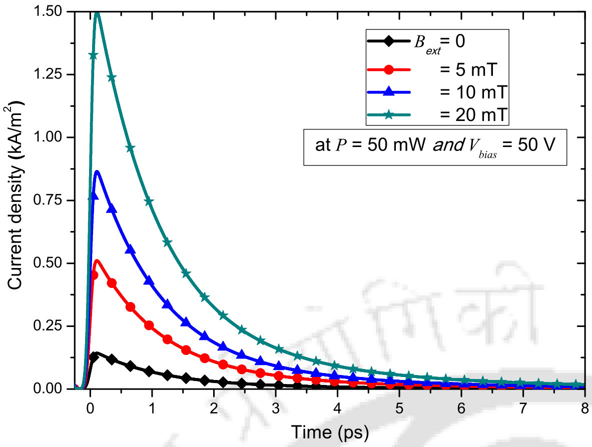

Fig. 6.8: Effect of the external magnetic field on the current density

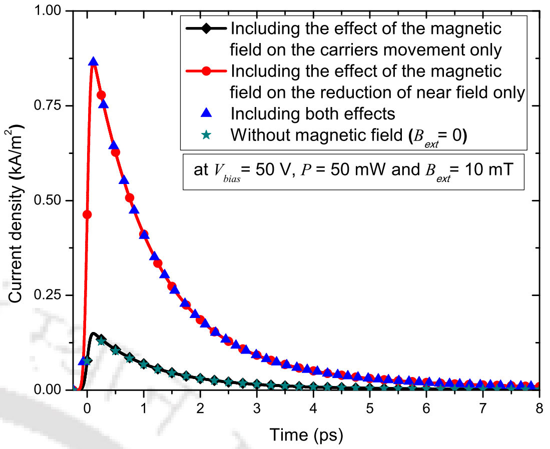

Fig. 6.9: Effect of the change in carrier's movement and reduction in the near field due to applied magnetic field on the current density

electric field is presented in section 6.3. It shows that the amplitude and the orientation of the radiated far-zone electric field strongly rely on the same of the applied magnetic field as shown in Fig. 6.10. The negative and the positive values of the magnetic field are used for the orientation along the negative and the positive directions of the *y*-axis, respectively.

The amplitude of the radiated far-zone electric field from the PCA increases with the applied magnetic field as shown in Fig. 6.11. At a fixed value of the laser beam power, the increment in the radiated far-zone electric field is calculated as:

$$R_v = \left.\frac{E_{THz}(peak)_{(at\ B_{ext})}}{E_{THz}(peak)_{(at\ B_{ext}=0)}}\right|_{P=constant} \tag{6.50}$$

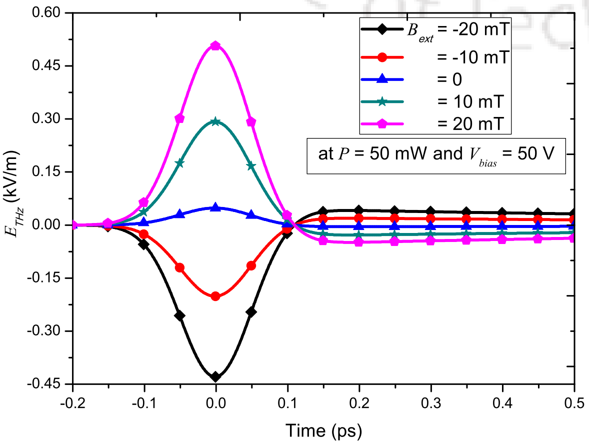

Fig. 6.10: External magnetic field effect on the polarity of the radiated far-zone electric field

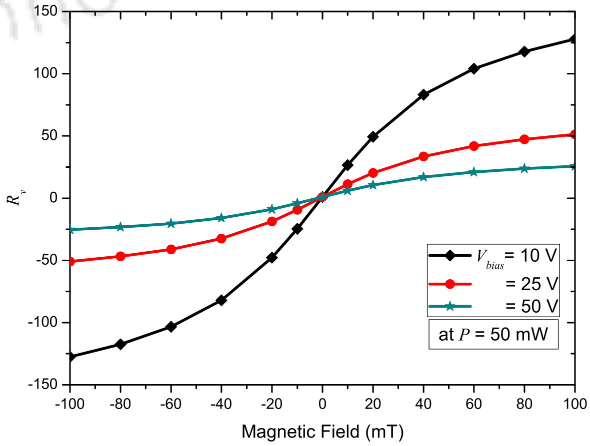

Fig. 6.11: Radiation enhancement at different values of the external magnetic field

Fig. 6.11 shows that the increment in the amplitude of the radiated far-zone electric field is very high at the low bias voltages and decreases with the increase in the bias voltage. However, the increment factor starts saturating at higher values of the magnetic field. Similarly, the amplitude of the far-zone electric field can also be enhanced by increasing the laser input power at the different values of the external magnetic field. The increment in the amplitude of the radiated far-zone electric field at a given value of the bias voltage is calculated as:

$$R_p = \left. \frac{E_{THz}(peak)_{(at\ B_{ext})}}{E_{THz}(peak)_{(at\ B_{ext}=0)}} \right|_{V_{bias}=constant} \tag{6.51}$$

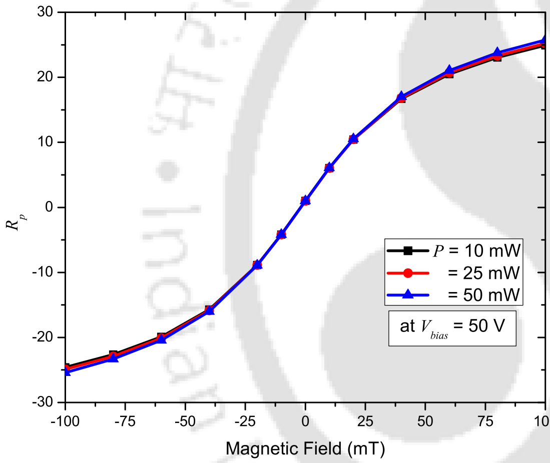

Fig. 6.12: Effect of the laser power on the radiation enhancement at different external magnetic field

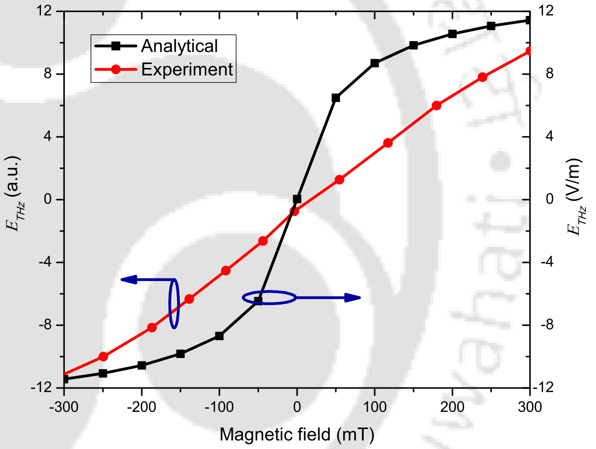

Fig. 6.13: Behavioral comparison of the external magnetic field effect on the radiated far-zone electric field from the PCA with the experimental result of the THz generation from the semiconductor surface [170]

From Figs. 6.11 and 6.12, it can be seen that the increment in the radiated far-zone electric field is very high in the case of the voltage variation, whereas changing the laser power does not affect much.

As there is no literature available dealing with the effect of the magnetic field on the radiation from a PCA, a comparison of the result of the radiated far-zone field from it (at V_{bias}=5 V, P=3.5 mW and z_d= 100 cm) is made with the magnetic field effect on the THz generation from the semiconductor surfaces from [170] and shown in Fig. 6.13. It can be seen from Fig. 6.13 that the PCA also exhibit the same behavior however, the saturation effect starts early.

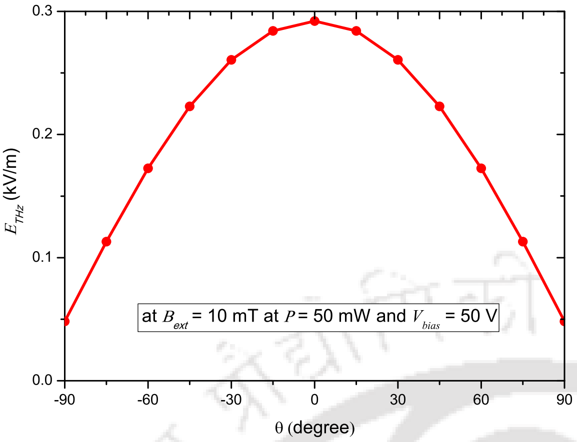

Fig. 6.14: Effect of the angle of incidence of the external magnetic field (from positive direction of the y-axis) on the radiated far-zone electric field.

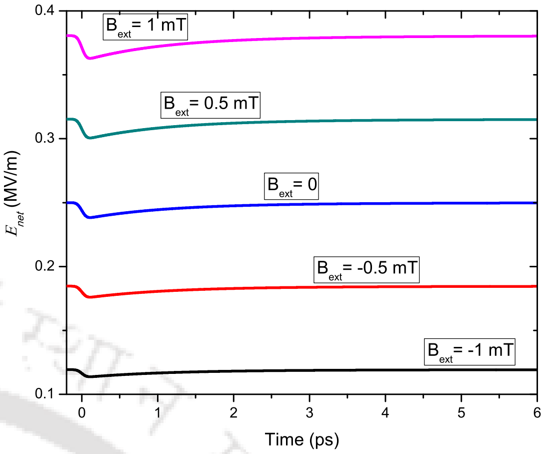

Fig. 6.15: Effect of the external magnetic field on E_{net}.

The effect of the angle of incidence of the applied magnetic field from the positive direction of the y-axis on the radiated far-zone electric field is shown in Fig. 6.14. For the large incidence angle of the magnetic field, the magnitude of the radiated far-zone THz field decreases due to the reduced amplitude of the magnetic field normal to the current density in the gap.

The effect of the external magnetic field on the net electric field at the gap is shown in Fig. 6.15 calculated at V_{bias} = 50 V and P = 50 mW. It can be seen that the net electric field can be changed by varying the amplitude and changing the orientation of the external magnetic field.

6.5 Summary

This chapter presents a novel idea to enhance the radiated power from a LAPCA by applying an external DC magnetic field. The analysis and results show that the improvement in the radiated power from a LAPCA using the external magnetic field is more effective compared to the other methods such as changing the laser input power, and the bias voltage. It has also been shown that the key factor in the enhancement of the radiated far-zone electric field is the reduction in the amplitude of the radiated near-zone electric field. Additionally, the external magnetic field also increases the current density by changing the carriers movement toward the surface, but the effect of this on the radiated THz field is negligibly small. It is interesting to note that the polarity of the radiated far-zone electric field can be controlled by the orientation of the applied external magnetic field as shown in the results.

7

Analysis of the Radiated Fields from the Photoconductive Antenna

Contents

7.1 Introduction

Since the first study made in the area of the THz generation using a PCA, several experimental, simulation, and circuit modeling studies have been reported in the literature. Among all the studies, very few are related to the analytical analysis of the radiated fields from the PCA as discussed in the chapter 2.

This chapter presents derivation of radiated fields from a PCA incorporating the semiconductor substrate effect in the analysis. Furthermore, to calculate the current density, an improved semiconductor carrier dynamics is proposed which helps in analyzing the radiation behavior of the PCA. The proposed carrier dynamics first calculates the transient variation of the substrate temperature which further helps in incorporating the temperature dependency of the different parameters. The proposed carrier dynamics also assimilates the effect of the transient mobilities of the carriers, transient lifetime of the carriers, carrier polarization, and the radiated near-zone field. In order to validate the derived formulae and proposed carrier dynamics, comparative studies are presented with the experimental results available in the literature.

7.2 Derivation of Radiated Fields from a PCA

The derivation of the radiated fields from a PCA is based on the assumption that the radiation is due to the fast changing current density. In order to develop the formulae for the radiated fields from a PCA, Maxwell's equations in the material media are used. The presented equations also incorporate the effect of the bound charges due to the polarization of the carriers and the current density due to these polarized carriers at the gap. The semiconductor substrate material used in the PCA has a very large defect densities facilitating a very small carrier lifetime and free carrier densities. Assuming that the initial free carrier densities are almost zero in the semiconductor substrate material, Maxwell's equations are written as [171]:

$$\nabla \cdot \vec{E} = \frac{\rho_p}{\varepsilon_0} \tag{7.1}$$

$$\nabla \cdot \vec{H} = 0 \tag{7.2}$$

$$\nabla \times \vec{D} = \varepsilon_0 \vec{J}_p - \frac{1}{c^2}\frac{\partial \vec{H}}{\partial t} \tag{7.3}$$

$$\nabla \times \vec{B} = \mu_0 \vec{J} + \mu_0 \frac{\partial \vec{P}_s}{\partial t} + \frac{1}{c^2}\frac{\partial \vec{E}}{\partial t} \tag{7.4}$$

where ρ_p is the bound charge density due to the polarization $\vec{P}_s$, $\vec{J}_p$ is the polarization current density, $\vec{J}$ is the photo-generated current density, $\vec{E}$ and $\vec{H}$ are the electric and the magnetic field intensities, respectively, $\vec{D}$ and $\vec{B}$ are the electric and the magnetic flux densities, respectively, and c is the light velocity. Also;

$$\rho_p = -\nabla \cdot \vec{P}_s; \qquad \vec{J}_p = (\nabla \times \vec{P}_s)/\varepsilon_0 \tag{7.5}$$

$$\vec{D} = \vec{P}_s + \varepsilon_0 \vec{E}; \qquad \vec{B} = \mu_0 \vec{H} \tag{7.6}$$

Using (7.1)-(7.6), the wave equation can be written as;

$$\nabla \times (\nabla \times \vec{E}) + \left(\frac{1}{c^2}\right)\frac{\partial^2 \vec{E}}{\partial t^2} = -\mu_0 \frac{\partial \vec{J}}{\partial t} - \mu_0 \frac{\partial^2 \vec{P}_s}{\partial t^2} \tag{7.7}$$

The solution of (7.7) can be written as;

$$\vec{E}(t) = \frac{1}{4\pi\varepsilon_0}\int \left(-\frac{[\nabla' \cdot \vec{P}_s]}{r^2} - \frac{1}{rc}\frac{\partial [\nabla' \cdot \vec{P}_s]}{\partial t} \right) \hat{r}\, dv' - \frac{1}{4\pi\varepsilon_0 r c^2}\int \left[\frac{\partial \vec{J}}{\partial t} + \frac{\partial^2 \vec{P}_s}{\partial t^2} \right] dv' \tag{7.8}$$

Similarly, the solution of magnetic field intensity can be given as;

$$\vec{H}(t) = \frac{1}{4\pi}\int \left\{ \left(\frac{[\vec{J}]}{r^2} + \frac{1}{rc}\left[\frac{\partial \vec{J}}{\partial t}\right] \right) \times \hat{r} + \frac{1}{r}\frac{\partial [\nabla' \times \vec{P}_s]}{\partial t} \right\} dv' \tag{7.9}$$

The operator ∇' operates at the source coordinates x', y', z' only. The [ ] in (7.9)(and also in the subsequent equations) indicates that the corresponding quantity is to be evaluated at the retarded time $t' = t - (r/c)$, where t is the time at which $\vec{E}$ and $\vec{H}$ fields are evaluated.

It can be seen that (7.8) and (7.9) have spatial derivative operations with the retarded time derivative. In order to simplify (7.8) and (7.9), following relations are used [172]:

$$\int \frac{1}{r}\frac{\partial [\nabla' \times \vec{P}_s]}{\partial t} dv' = \int \left(\frac{1}{r^2}\left[\frac{\partial \vec{P}_s}{\partial t}\right] \times \hat{r} + \frac{1}{rc}\left[\frac{\partial^2 \vec{P}_s}{\partial t^2}\right] \times \hat{r} \right) dv' \tag{7.10}$$

$$\int \left(\frac{[\nabla' \cdot \vec{P}_s]}{r^2} + \frac{1}{rc}\frac{\partial[\nabla' \cdot \vec{P}_s]}{\partial t} \right) \hat{r}\, dv' = -\int \left\{ \frac{1}{r^3}\left(3\left([\vec{P}_s]\cdot\hat{r}\right)\hat{r} - [\vec{P}_s]\right) + \frac{1}{rc^2}\left(\left[\frac{\partial^2 \vec{P}_s}{\partial t^2}\right]\cdot\hat{r}\right)\hat{r} + \frac{1}{r^2 c}\left(3\left(\left[\frac{\partial \vec{P}_s}{\partial t}\right]\cdot\hat{r}\right)\hat{r} - \left[\frac{\partial \vec{P}_s}{\partial t}\right]\right)\right\} dv' \qquad (7.11)$$

Using (7.8)-(7.11), the simplified solutions of the electric and the magnetic field intensities can be written as;

$$\vec{E}(t) = \frac{1}{4\pi\varepsilon_0}\int \left\{ \frac{1}{rc^2}\left(\left(\left[\frac{\partial^2 \vec{P}_s}{\partial t^2}\right]\cdot\hat{r}\right)\hat{r} - \left[\frac{\partial^2 \vec{P}_s}{\partial t^2}\right] - \left[\frac{\partial \vec{J}}{\partial t}\right]\right) + \frac{1}{r^3}\left(3\left([\vec{P}_s]\cdot\hat{r}\right)\hat{r} - [\vec{P}_s]\right) + \frac{1}{r^2 c}\left(3\left(\left[\frac{\partial \vec{P}_s}{\partial t}\right]\cdot\hat{r}\right)\hat{r} - \left[\frac{\partial \vec{P}_s}{\partial t}\right]\right)\right\} dv' \qquad (7.12)$$

$$\vec{H}(t) = \frac{1}{4\pi}\int \left\{ \frac{1}{rc}\left[\frac{\partial \vec{J}}{\partial t} + \frac{\partial^2 \vec{P}_s}{\partial t^2}\right]\times\hat{r} + \frac{1}{r^2}\left[\vec{J} + \frac{\partial \vec{P}_s}{\partial t}\right]\times\hat{r}\right\} dv' \qquad (7.13)$$

The far-zone fields can be written as:

$$\vec{E}_{far}(t) = \frac{1}{4\pi\varepsilon_0 rc^2}\int \left\{\left(\left(\left[\frac{\partial^2 \vec{P}_s}{\partial t^2}\right]\cdot\hat{r}\right)\hat{r} - \left[\frac{\partial^2 \vec{P}_s}{\partial t^2}\right] - \left[\frac{\partial \vec{J}}{\partial t}\right]\right)\right\} dv' \qquad (7.14)$$

$$\vec{H}_{far}(t) = \frac{1}{4\pi rc}\int \left(\left[\frac{\partial \vec{J}}{\partial t} + \frac{\partial^2 \vec{P}_s}{\partial t^2}\right]\times\hat{r}\right) dv' \qquad (7.15)$$

A 3D representation of a PCA is shown in Fig. 7.1. Using spherical co-ordinate system for the arrangement shown in Fig. 7.1 and dropping the time retardation, the far-zone fields can be written as:

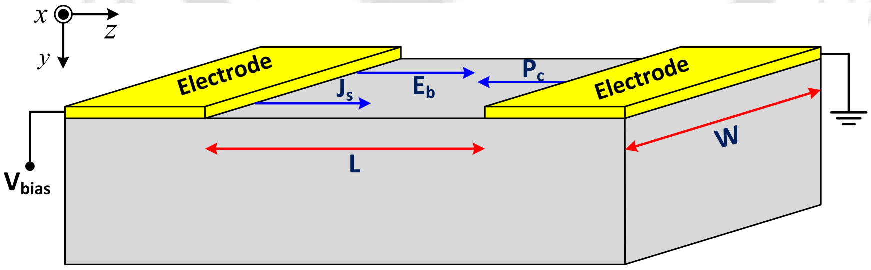

Fig. 7.1: 3D representation of a PCA with fields directions

$$\vec{E}_{far}(t) = \frac{1}{4\pi\varepsilon_0 rc^2}\int \left\{-\frac{\partial J}{\partial t}\cos\theta\,\hat{r} - \left(\frac{\partial^2 P_s}{\partial t^2} - \frac{\partial J}{\partial t}\right)\sin\theta\,\hat{\theta}\right\} dv' \qquad (7.16)$$

$$\vec{H}_{far}(t) = \frac{1}{4\pi rc}\int \left(\frac{\partial J}{\partial t} - \frac{\partial^2 P_s}{\partial t^2}\right)\sin\theta\,\hat{\phi}\, dv' \qquad (7.17)$$

7.3 Semiconductor Carrier Dynamics

In order to analyze the behavior of the radiated THz electric field, the calculation of the current density at the electrodes gap is essential. To evaluate the current density, an improved semiconductor carrier dynamics is proposed in this section. The analysis of the carrier dynamics presented in this section includes the effect of change in the substrate temperature due to lase illumination and dependency of different parameters on the substrate temperature. Furthermore, It also includes the carrier generation rate due to the laser beam impingement, the carrier polarization, change in the carrier lifetime, time-varying absorption coefficient due to band filling effect, and the transient velocities of the carriers.

The application of the laser beam on the semiconductor material not only generates the free carriers but also increases the temperature of the substrate material. As the different parameters related to the semiconductor material are temperature dependent, the analysis of the substrate temperature is imperative. In order to derive a closed-form analytical expression, the following assumptions have been considered:

- The optical absorption and power reflection coefficients of the material are temperature independent.
- The thickness of the semiconductor substrate material is very large compare to the laser beam skin depth.
- A uniform laser illumination at the electrodes gap.
- The Gaussian laser pulse is approximated with the exponential functions as shown in the Fig. 7.2.

Due to uniform laser illumination at the surface, the heat flows in y direction only for the given setup in Fig. 7.1. The one dimensional differential equation of the heat flow in terms of the temperature $T(y,t)$ and laser intensity is written as [173]:

$$\frac{\partial T(y,t)}{\partial t} = \eta_T \frac{\partial^2 T(y,t)}{\partial y^2} + \frac{\alpha I_T\, e^{-\alpha y}}{\rho c_p} \tag{7.18}$$

where $\eta_T = \frac{k}{\rho c_p}$, ρ is the density of the material, c_p is the specific heat capacity of the material, k

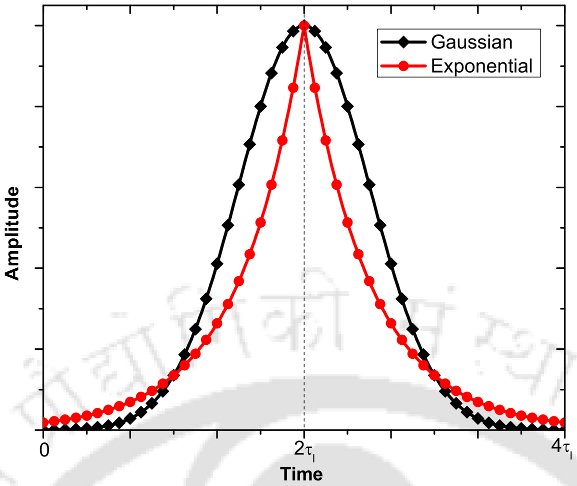

Fig. 7.2: Approximation of Gaussian pulse using exponential functions

is the thermal conductivity of the material, α is the optical absorption coefficient of the material, and I_T is the laser intensity within the radius r applied at the material surface.

The laser intensity within the radius r including the time variation as shown in Fig. 7.2 can be given as:

$$I_T = \begin{cases} A_T\, e^{\frac{2(t-2\tau_l)}{\tau_l}} & \text{for } 0 \le t \le 2\tau_l \\ A_T\, e^{\frac{-2(t-2\tau_l)}{\tau_l}}\, u(t-2\tau_l) & \text{for } 2\tau_l \le t < \infty \end{cases} \tag{7.19}$$

with

$$A_T = \frac{2(1-R)P_0}{\pi\omega_0^2}\left[1 - e^{\left(\frac{-2r^2}{\omega_0^2}\right)}\right] \tag{7.20}$$

where τ_l is the laser pulse width, R is the power reflection coefficient, P_0 is the laser peak power, and ω_0 is the laser beam waist radius.

In order to achieve the closed form solution, the following boundary conditions are applied:

- for $0 \le t \le 2\tau_l$

$$T(y,0) = T(\infty,t) = T_0 = 300\ \text{K};\ \left.\frac{\partial T}{\partial y}\right|_{y=0} = 0$$

- for $2\tau_l \le t < \infty$

$$T(y,2\tau_l) = T_{2\tau_l};\ T(\infty,t) = T_0;\ \left.\frac{\partial T}{\partial y}\right|_{y=0} = 0$$

Using the boundary conditions with (A.10) & (7.19), the solution for the surface temperature (at $y = 0$) can be written as:

$$
T(t) = \begin{cases}
T_0 + \dfrac{\alpha A_T e^{-4}\tau_l}{\rho c_p}\left[\dfrac{\left(e^{\frac{2t}{\tau_l}} - e^{\eta_T\alpha^2 t}\right)}{(2-\eta_T\alpha^2\tau_l)} - \dfrac{\alpha\sqrt{\eta_T\tau_l}\, e^{\frac{2t}{\tau_l}}\operatorname{erf}\left(\sqrt{\frac{2t}{\tau_l}}\right)}{\sqrt{2}\,(2-\eta_T\alpha^2\tau_l)} + \dfrac{e^{\eta_T\alpha^2 t}\operatorname{erf}\left(\alpha\sqrt{\eta_T t}\right)}{(2-\eta_T\alpha^2\tau_l)}\right] \\
\hfill \text{for } 0 \le t \le 2\tau_l \\
T_{2\tau_l} + \dfrac{\alpha A_T e^{4}\tau_l}{\rho c_p}\left[\dfrac{\left(e^{-4+\eta_T\alpha^2(t-2\tau_l)} - e^{-\frac{2t}{\tau_l}}\right)}{(2+\eta_T\alpha^2\tau_l)} - \dfrac{e^{-4+\eta_T\alpha^2(t-2\tau_l)}\operatorname{erf}\left[\alpha\sqrt{\eta_T(t-2\tau_l)}\right]}{(2+\eta_T\alpha^2\tau_l)}\right. \\
\qquad\qquad \left. + \dfrac{\alpha\sqrt{\eta_T\tau_l}\, e^{\frac{-2t}{\tau_l}}\operatorname{erfi}\left(\sqrt{\frac{2(t-2\tau_l)}{\tau_l}}\right)}{\sqrt{2}\,(2+\eta_T\alpha^2\tau_l)}\right] \\
\hfill \text{for } 2\tau_l \le t < \infty
\end{cases} \tag{7.21}
$$

where $T_{2\tau_l}$ is the substrate temperature at $t = 2\tau_l$. The detailed solution of the heat equation is explained in Appendix A.2.

7.3.1 Carrier Densities

The photocarrier densities generated at the gap by the laser beam are calculated using the continuity equation given as [141, 142]:

$$\frac{dn(t)}{dt} = -\frac{n(t)}{\tau_n} + g(t) \tag{7.22}$$

$$\frac{dp(t)}{dt} = -\frac{p(t)}{\tau_p} + g(t) \tag{7.23}$$

where $n(t)$ and $p(t)$ are the time dependent electrons and the holes densities, respectively, τ_n and τ_p are the lifetime of the electrons and the holes, respectively, and $g(t)$ is the photo-carrier generation rate due to laser impingement and can be written as:

$$g(t) = \frac{2P(t,r)}{\pi\omega_0^2 h\nu_{opt}} \tag{7.24}$$

where h is the Planck's constant, ν_{opt} is the laser frequency, and $P(t,r)$ is the total absorbed power by the semiconductor material within the radius r.

The total power, absorbed by the semiconductor material within the radius r, including the beam penetration in the material of a Gaussian profile laser beam is given as [152]:

$$P_{opt}(t) = \alpha[1 - R]P_0 \left[1 - e^{\left(\frac{-2r^2}{\omega_0^2}\right)}\right] e^{\left(\frac{-2(t-2\tau_l)^2}{\tau_l^2}\right)} e^{-\alpha d} \tag{7.25}$$

where d is the depth in to the semiconductor material.

For a constant values of the carrier's lifetimes τ_n and τ_p, the solution of the Eqs. (7.22) and (7.23) can be written as:

$$\begin{aligned} n(t) = \frac{(1-R)\tau_l P_0}{\sqrt{2}\pi h f \omega_0^2} &\left[1 - e^{\left(\frac{-2r^2}{\omega_0^2}\right)}\right] \left[1 - e^{-\alpha l_n}\right] e^{\left(\frac{-t}{\tau_n}\right)} e^{\left(\frac{\tau_l^2}{8\tau_n^2} + \frac{2\tau_l}{\tau_n}\right)} \\ &\times \left[\mathrm{erf}\left(\frac{4}{\sqrt{2}} + \frac{\sqrt{2}\tau_l}{4\tau_n}\right) - erf\left(\frac{4}{\sqrt{2}} + \frac{\sqrt{2}\tau_l}{4\tau_n} - \frac{\sqrt{2}t}{\tau_l}\right)\right] \end{aligned} \tag{7.26}$$

where l_n is the diffusion length of the electrons and can be calculated from, $l_n = \sqrt{\frac{k_B T \mu_n \tau_n}{q}}$, k_B is the Boltzmann constant, T is the temperature, μ_n is the mobility of the electrons, and q is the electron charge.

$$\begin{aligned} p(t) = \frac{(1-R)\tau_l P_0}{\sqrt{2}\pi h f \omega_0^2} &\left[1 - e^{\left(\frac{-2r^2}{\omega_0^2}\right)}\right] \left[1 - e^{-\alpha l_p}\right] e^{\left(\frac{-t}{\tau_p}\right)} e^{\left(\frac{\tau_l^2}{8\tau_p^2} + \frac{2\tau_l}{\tau_p}\right)} \\ &\times \left[\mathrm{erf}\left(\frac{4}{\sqrt{2}} + \frac{\sqrt{2}\tau_l}{4\tau_p}\right) - erf\left(\frac{4}{\sqrt{2}} + \frac{\sqrt{2}\tau_l}{4\tau_p} - \frac{\sqrt{2}t}{\tau_l}\right)\right] \end{aligned} \tag{7.27}$$

where l_p is the diffusion length for the holes and can be calculated from, $l_p = \sqrt{\frac{k_B T \mu_p \tau_p}{q}}$, μ_p is the mobility of the holes.

However, in the analysis presented in this chapter, a time varying carrier's lifetimes have been assumed which depends on the density of the filled and unfilled trap densities. The time dependency of the carrier's lifetime will be discussed in subsequent sections. The carriers within the volume corresponding to its diffusion length contribute to the surface current while the remaining in the active region get recombine with the traps before reaching the surface of the semiconductor substrate. So, to calculate the average carrier densities (n_{av} and p_{av}), volumes corresponding to the carrier's diffusion lengths have been used in the analysis.

7.3.2 Absorption Constant

The rapid increase of the carrier densities at the semiconductor surface changes the amplitude of the optical absorption coefficient (α) which is modeled as proposed in [166]. For an n-type semiconductor material, the change in the absorption coefficient due to optical injection of the carriers is modeled as:

$$\alpha = \alpha_0 - \Delta\alpha(n_{av}, p_{av}, E) \tag{7.28}$$

$$\begin{aligned}\Delta\alpha(n_{av}, p_{av}, E) = {} & \frac{C_{hh}}{E}\sqrt{E - E_g}[1 - f_v(E_{ah}) + f_c(E_{bh})] \\ & + \frac{C_{lh}}{E}\sqrt{E - E_g}[1 - f_v(E_{al}) + f_c(E_{bl})]\end{aligned} \tag{7.29}$$

$$f_v(E_{ah,al}) = \left[1 + e^{\left(\frac{E_{ah,al} - E_{FV}}{k_B T}\right)}\right]^{-1} \tag{7.30}$$

$$f_c(E_{bh,bl}) = \left[1 + e^{\left(\frac{E_{bh,bl} - E_{FC}}{k_B T}\right)}\right]^{-1} \tag{7.31}$$

$$E_{ah,al} = (E_g - E)\left[\frac{m_e}{m_e + m_{hh,lh}}\right] - E_g \tag{7.32}$$

$$E_{bh,bl} = (E - E_g)\left[\frac{m_{hh,lh}}{m_e + m_{hh,lh}}\right] \tag{7.33}$$

$$E_{FC} = \left\{\ln\left(\frac{n_{av}}{N_c}\right) + \left(\frac{n_{av}}{N_c}\right)\left[64 + 0.05524\left(\frac{n_{av}}{N_c}\right)\left\{64 + \sqrt{\frac{n_{av}}{N_c}}\right\}\right]^{-0.25}\right\} k_B T \tag{7.34}$$

$$E_{FV} = \left(-\left\{\ln\left(\frac{p_{av}}{N_v}\right) + \left(\frac{p_{av}}{N_v}\right)\left[64 + 0.05524\left(\frac{p_{av}}{N_v}\right)\left\{64 + \sqrt{\frac{p_{av}}{N_v}}\right\}\right]^{-0.25}\right\} - E_g\right) k_B T \tag{7.35}$$

where α_0 is the optical absorption coefficient of the semiconductor material for the photon energy E, and E_g is the semiconductor bandgap energy.

7.3.3 Carrier Lifetime

The carrier lifetime in the PCA is assumed to be equal to the time taken by the traps to capture the carriers which is given as [141]:

$$\tau_n = \frac{1}{(\sigma_n v_{th,n} N_{fr})} \tag{7.36}$$

$$\tau_p = \frac{1}{(\sigma_p v_{th,p} N_{fi})} \tag{7.37}$$

where σ_n and σ_p are the capture cross-sections for the electrons and the holes, respectively, N_{fr} is the density of unfilled traps, N_{fi} is the density of the filled traps, $v_{th,n}$ and $v_{th,p}$ are the thermal velocities of the electrons and the holes, respectively, and can be calculated from: $v_{th,n,p} = \sqrt{\frac{3k_BT}{m^*_{n,p}}}$, $m^*_{n,p}$ are the effective masses of the electrons and the holes, respectively.

Due to capturing(recombination) of the electrons and the holes with the traps, during the THz generation process, the densities of the filled and the unfilled traps varies with the time and can be computed from:

$$\frac{\partial N_{fr}}{\partial t} = \frac{N_{fi}}{\tau_p} - \frac{N_{fr}}{\tau_n} \tag{7.38}$$

$$\frac{\partial N_{fi}}{\partial t} = \frac{N_{fr}}{\tau_n} - \frac{N_{fi}}{\tau_p} \tag{7.39}$$

7.3.4 Current Density

The drift current in the PCA is caused due to the motion of the electrons as well as the holes. The total current density can be given by adding the current densities of the electrons and the holes. The total surface current density is given as:

$$J_s(t) = q\left[n_{av}(t)v_n(t)l_n + p_{av}(t)v_p(t)l_p\right] \tag{7.40}$$

where $v_n(t)$ and $v_p(t)$ are the time dependent velocities of the electrons and the holes, respectively.

7.3.5 Net Electric Field

As it can be seen from the Fig. 7.1 that the net electric field across the electrodes gap can be given by the algebraic sum of the bias electric field and the field due to the carrier polarization. The net electric field at the gap (for small and semi-large aperture PCA) can be written as [123, 153]:

$$E_{net}(t) = E_{bias} - \frac{P_s(t)}{\zeta \epsilon_0 \epsilon_r} \tag{7.41}$$

where ζ is the is a geometrical factor and is equal to 3 for isotropic material, and ϵ_r is the permittivity of the semiconductor substrate material.

Whereas, for the large aperture PCAs, the net electric field at the gap also includes the effect of the radiated near-zone electric field as explained in section 6.3.4, and is given as:

$$E_{net}(t) = E_{bias} - \frac{P_s(t)}{\zeta \epsilon_0 \epsilon_r} - E_r(t) \tag{7.42}$$

$$E_r(t) = -\frac{\eta_0 J_s(t)}{1 + \sqrt{\varepsilon_r}} \tag{7.43}$$

where η_0 is the free space impedance.

7.3.6 Carrier Polarization

The carriers at the gap region get polarized due the electric field across the gap. It is given as [153]:

$$\frac{dP_s(t)}{dt} = -\frac{P_s(t)}{\tau_r} + J_s(t) \tag{7.44}$$

where τ_r is the carrier recombination time of the electrons with the holes in the pure semiconductor material.

7.3.7 Carrier Velocities

The transient velocities of the carriers are modeled using the transient mobilities given by the Caughey-Thomas and Arora mobility models. These mobility models are used to incorporate the electric field and the doping density dependence of the mobilities. The average mobilities μ_n and μ_p of the electrons and the holes, respectively, are calculated by using Caughey-Thomas, and Arora mobility models as explained in section 6.3.6. Moreover, the proposed carrier dynamics in this chapter also include the temperature dependency of the mobilities given as [141, 145, 146]:

$$\mu_{elec,n}(E_{net}) = \mu_{low,n}\left[1+\left(\frac{\mu_{low,n}E_{net}}{v_{sat}^{n}}\right)^{2}\right]^{-0.5} \tag{7.45}$$

$$\mu_{elec,p}(E_{net}) = \mu_{low,p}\left[1+\left(\frac{\mu_{low,p}E_{net}}{v_{sat}^{p}}\right)^{2}\right]^{-0.5} \tag{7.46}$$

$$\mu_{dop,n}(n_{av}) = \mu_{ln} + \mu_{diff,n}\left[1+\left(\frac{n_{av}}{N_n}\right)^{a_n}\right]^{-1} \tag{7.47}$$

$$\mu_{dop,p}(p_{av}) = \mu_{lp} + \mu_{diff,p}\left[1+\left(\frac{p_{av}}{N_p}\right)^{a_p}\right]^{-1} \tag{7.48}$$

$$v_{sat}^{n,p} = \left[11.3 - 3.6\left(\frac{T}{T_0}\right)\right]\times 10^{4} \tag{7.49}$$

$$\mu_{ln} = \mu_{low,n}\left(\frac{T}{T_0}\right)^{-0.7457} \tag{7.50}$$

$$\mu_{lp} = \mu_{low,p}\left(\frac{T}{T_0}\right)^{-1.124} \tag{7.51}$$

$$\mu_{diff,n} = \mu_{d,n}\left(\frac{T}{T_0}\right)^{-2.687} \tag{7.52}$$

$$\mu_{diff,p} = \mu_{d,p}\left(\frac{T}{T_0}\right)^{-2.366} \tag{7.53}$$

$$N_n = n_0\left(\frac{T}{T_0}\right)^{3.535} \tag{7.54}$$

$$N_p = p_0\left(\frac{T}{T_0}\right)^{3.69} \tag{7.55}$$

$$a_n = 0.6273\left(\frac{T}{T_0}\right)^{-0.1441} \tag{7.56}$$

$$a_p = 0.8057\left(\frac{T}{T_0}\right)^{0} \tag{7.57}$$

$$\mu_{d,n} = 8500 - \mu_{low,n} \tag{7.58}$$

$$\mu_{d,p} = 400 - \mu_{low,p} \tag{7.59}$$

where $\mu_{d,n}$, $\mu_{d,p}$, $\mu_{low,n}$, and $\mu_{low,p}$ are in cm^{2}V^{-1}s^{-1}.

The effective mobilities of the electrons and the holes can be given as:

$$\mu_n(t) = \frac{\mu_{elec,n}(t)\mu_{dop,n}(t)}{\mu_{elec,n}(t) + \mu_{dop,n}(t)} \tag{7.60}$$

$$\mu_p(t) = \frac{\mu_{elec,p}(t)\mu_{dop,p}(t)}{\mu_{elec,p}(t) + \mu_{dop,p}(t)} \tag{7.61}$$

Using the transient mobilities, the velocities of the carriers are given as:

$$v_n(t) = \mu_n(t)E_{net}(t) \tag{7.62}$$

$$v_p(t) = \mu_p(t)E_{net}(t) \tag{7.63}$$

7.3.8 Radiated THz Fields

As the diffusion lengths of the carriers, l_n & l_p, are very small compared to the gap dimensions, the generated current density can be taken as the surface current density. Considering the THz radiation is emitted and detected along the y-axis for setup shown in Fig. 7.1, (7.16) and (7.17) can be re-written as:

$$\vec{E}_{THz}(t) = \frac{A}{4\pi\varepsilon_0 y_d c^2}\left(\frac{\partial J_s}{\partial t} - \frac{\partial^2 P_s}{\partial t^2}\right)\hat{\theta} \tag{7.64}$$

$$\vec{H}_{THz}(t) = \frac{A}{4\pi y_d c}\left(\frac{\partial J_s}{\partial t} - \frac{\partial^2 P_s}{\partial t^2}\right)\hat{\phi} \tag{7.65}$$

where A is the gap area and y_d is the distance along the y-axis from the source point. Eqs. (7.64) and (7.65) can be expanded further with the help of other relations shown in previous equations and are given in Appendix A.3.

7.4 Results and Discussions

The PCA's performance has been analyzed by using the derived formule in section 7.2 with the proposed semiconductor carrier dynamics in section 7.3. The value of the different parameters used in the analytical calculations are given in Table 7.1 [132, 141, 165, 166, 173, 174]. Moreover, The analytically calculated results are compared with the experimental results reported in the literature. The reported experimental results are given in arbitrary units, so instead of a direct comparison, a behavioral comparison of the results are presented and the parameters values are provided with the results.

Table 7.1: Parameters Details for the calculation of the radiated fields

Parameter	**Value**	**Parameter**	**Value**
k	33 W/m K	ρ	5320 kg/m^3
c_p	350 J/kg K	τ_l	60 fs
α_0	6000 cm^{-1}	f	375 THz
ε_r	12.9	ω_0	0.707×gap width
r	0.5×gap width	R	0.318
τ_n	1 ps	τ_p	30 ps
m_0	9.1×10^{-31} Kg	τ_r	100 ps
C_{hh}	1.5×10^{14} m s$^{-1/2}$	C_{lh}	7.8×10^{13} m s$^{-1/2}$
m_{hh}	0.45×m_0	m_{lh}	0.084×m_0
m_e	0.066×m_0	E_g	1.42 eV
N_c	4.3×10^{23}m^{-3}	N_v	8.3×10^{24}m^{-3}
σ_n	1×10^{-19} m^2	σ_p	1×10^{-20} m^2
m_n^*	0.067×m_0	m_p^*	0.47×m_0
$\mu_{low,n}$	300 cm^{2}V^{-1}s^{-1}	$\mu_{low,p}$	60 cm^{2}V^{-1}s^{-1}
n_0	1×10^{20} m^{-3}	p_0	1×10^{21} m^{-3}
f_{rep}	80 MHz	y_d	100 mm

7.4.1 Effect of the Laser Power on the Substrate Temperature

The laser beam power increases the temperature of the semiconductor substrate which varies with the time. As the semiconductor material parameters are temperature dependent, the behavior of the substrate temperature has been analyzed and included in the semiconductor carrier dynamics used in this study. The transient behavior of the substrate temperature is shown in Fig. 7.3.

7.4.2 Effect of the Bias Voltage and the Laser Power

The current density in the PCA strongly depends on the carrier concentrations and the velocities, as given by (7.40). The carrier densities depend on the laser beam power as shown in (6.21) and (6.22). Similarly, the carrier velocities depend on the net electric field at the gap as given by (7.62) and (7.63). The net electric field at the gap can be changed by varying the bias voltage and given in (7.41) & (7.42). So, by increasing the laser power and the bias voltage, the radiated THz electric field can be enhanced as shown in Fig. 7.4.

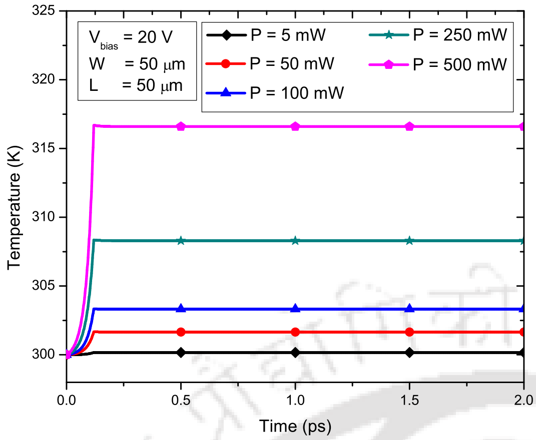

Fig. 7.3: Semiconductor substrate temperature at different laser beam power

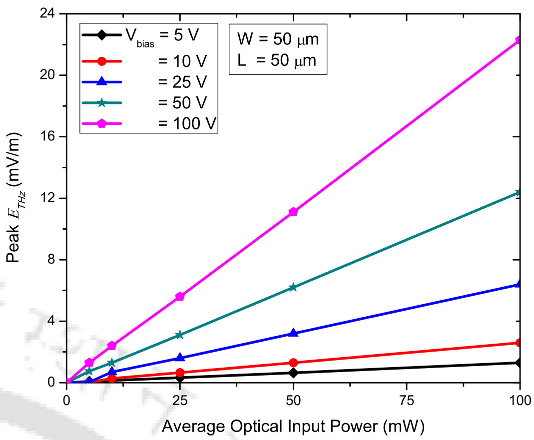

Fig. 7.4: Effect of the bias voltages and the laser powers on the radiated THz field

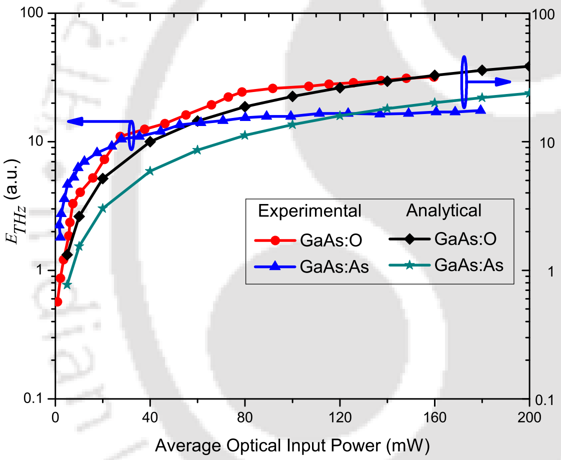

Fig. 7.5: Comparison of the laser power effect on the radiated THz field with the results from [169]

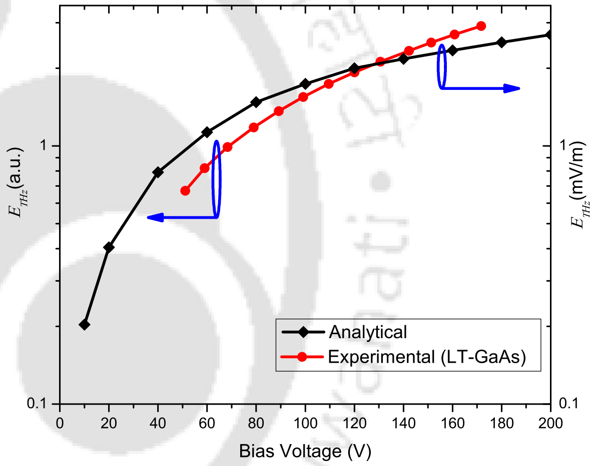

Fig. 7.6: Comparison of the bias voltage effect on the radiated THz field with the results from [174]

Table 7.2: Parameters' value for Fig. 7.5

Parameter	Value	Parameter	Value
V_{bias}(GaAs:O)	100 V [169]	V_{bias}(GaAs:As)	110 V [169]
L	120 μm [169]	W	10 μm [169]
ω_0	5 μm [169]	f_{rep}	82 MHz [169]
f	394.74 THz [169]	τ_l	100 fs
τ_n(GaAs:O)	0.5 ps	τ_n(GaAs:As)	0.25 ps
τ_p(GaAs:O)	15 ps	τ_p(GaAs:As)	7.5 ps
$\mu_{low,n}$(GaAs:O)	250 cm^{2}V^{-1}s^{-1}	$\mu_{low,n}$(GaAs:As)	200 cm^{2}V^{-1}s^{-1}
$\mu_{low,p}$(GaAs:O)	50 cm^{2}V^{-1}s^{-1}	$\mu_{low,p}$(GaAs:As)	40 cm^{2}V^{-1}s^{-1}
y_d	240 mm		
Other parameters values are taken from Table 7.1			

Table 7.3: Parameters' value for Fig. 7.6

Parameter	Value	Parameter	Value
L	50 μm [174]	W	50 μm [174]
P	90 mW [174]	y_d	1.15 m
Other parameters values are taken from Table 7.1			

The analytically computed results of the laser beam power and the bias voltage effect on the radiated electric field are compared with the reported experimental results in [169] and [174], respectively. The comparison of the results are shown in Fig. 7.5 and 7.6. The different parameters and their values used in the analytical calculations to analyze the effect of the laser power and the bias voltage are given in Table 7.2 and 7.3, respectively.

7.4.3 Effect of the Laser Pulse Width

The average carrier densities in the PCA depend on the peak power of the laser beam as given by (6.21) and (6.22). Decreasing the laser pulse width increases the laser peak power which results in an increased current density and the radiated electric field. Also, the radiated power from a PCA increases with the radiated THz electric field. A comparison of the analytically calculated radiated powers with the experimental results from [175] is shown in Fig. 7.7. The values of the different parameters used in the analytical calculations are given in Table 7.4.

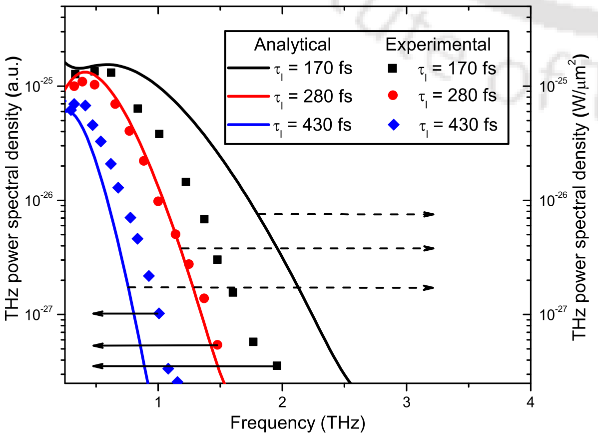

Fig. 7.7: Comparison of laser pulsewidth effect on the radiated THz field with the results from [175]

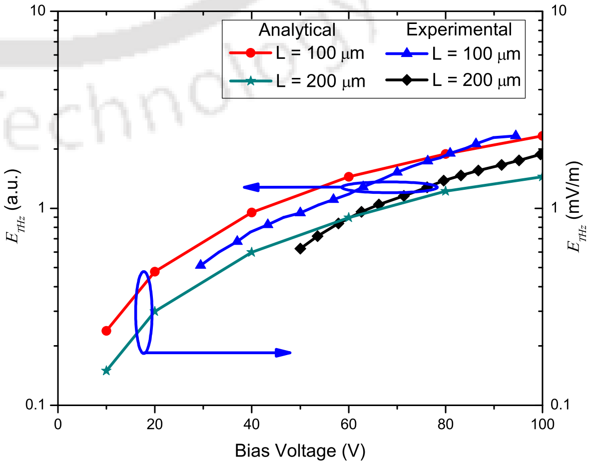

Fig. 7.8: Comparison of the gap length effect on the radiated THz field with the results from [168]

Table 7.4: Parameters Details for Fig. 7.7

Parameter	Value	Parameter	Value
V_{bias}	50 V [175]	L	20 μm [175]
W	20 μm [175]	f_{rep}	45 MHz [175]
P	8 mW [175]	f	291.26 THz [175]
E_g	1.2 eV	y_d	400 mm
$\mu_{low,n}$	100 cm^{2}V^{-1}s^{-1}	$\mu_{low,p}$	20 cm^{2}V^{-1}s^{-1}
Other parameters values are taken from Table 7.1			

7.4.4 Effect of the Gap Length

From (7.62) and (7.63), it is evident that the carrier velocities depend on the amplitude of the net electric field at the gap. At the same time, the net electric field strongly depends on the bias electric field as given by (7.41) & (7.42), whose amplitude can be changed by changing the gap length. Decreasing the gap length increases the net electric field, which results in a high current density thereby increasing the radiated electric field. The analytically calculated results of the gap length effect on the radiated THz electric field have been compared with the experimental results from [168] and shown in Fig. 7.8. Table 7.5 shows the value of the parameters used in the analytical calculations.

Table 7.5: Parameters Details for Fig. 7.8

Parameter	Value	Parameter	Value
f_{rep}	75 MHz [168]	τ_l	150 fs [168]
P	90 mW [168]	y_d	45 mm
$\mu_{low,n}$	200 cm^{2}V^{-1}s^{-1}	$\mu_{low,p}$	40 cm^{2}V^{-1}s^{-1}
Other parameters values are taken from Table 7.1			

7.5 Summary

In this chapter, the formulae for the radiated fields from a PCA incorporating the effect of the semiconductor substrate have been presented. Moreover, an improved semiconductor carrier dynamics has been proposed incorporating the transient substrate temperature and its effect on the different parameters, the carrier polarization, the transient velocities & lifetime of the carriers , and the antenna geometry. The developed formulae, with the help of the proposed carriers dynamics, are able to predict the effect of the different parameters on the radiated fields as discussed in section 7.4.

8

Discussion and Suggestions for Future Work

Contents

In this thesis, we have addressed issues concerning modeling of the THz generation from a PCA. We have proposed different models and methods to analyze the process of the THz radiation from a PCA and to improve its performance. In this chapter, the main contributions of the work presented in this thesis are summarized in section 8.1, and possible future extension of the work are outlined in section 8.2.

8.1 Summary of Contributions and Discussions

In this section, a summary and the review of the findings during this thesis work are presented. This thesis presents:

- ✔ **Simulation study of the current pulse generation in the PCA :**

  The simulation study include the semiconductor physics such as effect of the trap parameters, the different parameters dependencies, inter and intra-band transitions, and the different models affecting the carrier dynamics. The effect of the various parameters on the current pulse behavior has been analyzed and discussed. Furthermore, it also presents a novel study of the effect of the trap parameters, laser spot position, and laser beam radius on the current pulse.

- ✔ **Equivalent electrical circuit models of the PCA :**

  This study proposed an improved circuit model of the PCA as a THz source and a novel circuit model of the PCA as a detector. The proposed circuit models incorporate the components based on the physics undergoing in their operations. The circuit model of the PCA source has a time-varying conductance for the conductivity in the active region, time-varying capacitance for the accumulation of unpaired carriers in the active region, and a screening voltage for the screening effect due to carriers polarization. A novel method to calculate the transient capacitance is proposed in this work. Similarly, the PCA receiver has a time-varying conductance for the conductivity in the active region, time-varying capacitance for the accumulation of unpaired carriers in the active region. Keeping the simplicity of the lumped circuit models, the physical behavior of the device is taken into consideration while calculating the circuit components value. Using the proposed circuit models, the influence of the various device parameters on the performance of the PCA have been analyzed. The several results of the PCA source have been found to be agreed well with the simulation and the reported experimental results.

- ✔ **The effect of the near fields on the performance of the large aperture PCAs :**

  The presented theoretical study includes the electromagnetic boundary conditions and the semiconductor carrier dynamics. It analyzes the radiated near-zone fields effect on the behavior of the various parameters of the PCA. It shows that the near-zone electric field produces a negative effect on the net electric field at the electrodes gap thereby decreasing the current density at the gap and carrier velocities which results in reduced THz radiation.

- ✔ **External magnetic field assisted performance enhancement of the large aperture PCAs :**

  This study presents a novel method to improve the output characteristics of the PCA by using an external magnetic field. This study includes the electromagnetic boundary conditions, semiconductor carrier dynamics with the effect of the external magnetic field on the carriers. The results show that the amplitude and the polarity of the radiated far zone electric field can be controlled by the amplitude and the orientation of the applied magnetic field, respectively. It has also been observed that the radiation enhancement of the PCA mainly depends on the bias voltage, external magnetic field amplitude and its orientation, rather than the laser beam power.

- ✔ **Analysis of the Radiated THz Fields from the PCA :**

  In this work, a theoretical study to derive the formulae for the radiated fields from the PCA has been presented. The study uses the basic electromagnetic relations including the semiconductor material effect. Furthermore, an improved semiconductor carrier dynamics has also been proposed which incorporates the transient temperature analysis, band-filling effect, transient mobilities, and transient carrier lifetime. The results have been validated by the comparative study with the reported experimental results in the literature.

8.2 Suggestions for the Future Work

In this thesis, several issues associated with the modeling and the performance enhancement of the PCAs have been studied. These studies are based on the few assumptions which reduces the accuracy of the results. We propose some possible directions in which the present work can be extended to make these models more reliable and accurate.

- The simulation study of the current pulse generation in the PCA has been carried out without inclusion of the radiated field effect on it. It would be interesting to analyze the current pulse behavior, including the effect of the radiated fields in the analysis.
- The modeling of the equivalent electrical circuits of the PCAs have been carried out assuming the antenna to be frequency independent, neglecting antenna losses, and a rectangular shape active region. To make the circuit models more generalized, the frequency dependency could be added which also requires to incorporate the antenna losses in the calculations. Moreover, the carrier concentrations could be computed by utilizing the spatial distribution of the laser power, electric field, and carrier mobilities.
- The external magnetic field effect on the performance of the large aperture PCA presented in this thesis is purely theoretical and based on several assumptions. Including the magnetic properties of the material would make the analysis more practical. Also, a experimental validation can be done to prove the proposed theory.
- In this thesis, several physics and effects have been incorporated in the proposed semiconductor carrier dynamics to compute the PCAs behaviors. However, there are still various semiconductor physics which could have been included to make the analysis more accurate. The various physics such as different scattering mechanism, band-to-band transitions, temperature effect on the trap behaviors, and trap mobilities, can be used in the carrier dynamics.

A

Appendix

A.1 Finite Difference Method

Many advance engineering problems involve non linear and non-homogeneous differential equations. The solution of these equations often are beyond the reach by classical methods and a closed form solution is normally not possible. To solve these equations, numerical methods such as Finite Difference Method (FDM), Finite Element Method (FEM), are employed [176]. The FDM is used to solve ordinary differential equations that have conditions imposed on the boundary rather than at the initial point.

Physically, a derivative represents the rate of change of a physical quantity represented by a function with respect to the change of its variable. For example:

$$\frac{\partial f}{\partial x} \approx \frac{\triangle f}{\triangle x} \tag{A.1}$$

It should be noted that smaller the value of $\triangle x$ closer the values of the both sides in (A.1).

In FDM, there are three ways to express the differentials of the functions:

(i) Forward Difference Scheme

(ii) Backward Difference Scheme

(iii) Central Difference Scheme

Using the FDM, the first and second order differentials can be expressed as:

- **Forward Difference Scheme:**

$$\left.\frac{\partial f}{\partial x}\right|_{x=x_i} \approx \left.\frac{\Delta f}{\Delta x}\right|_{x=x_i} = \frac{f_{i+1} - f_i}{x_{i+1} - x_i} = \frac{f_{i+1} - f_i}{\triangle x} \tag{A.2}$$

where $\triangle x$ is the incremental step size.

$$\left.\frac{\partial^2 f}{\partial x^2}\right|_{x=x_i} = \frac{f_{i+2} - 2f_{i+1} + f_i}{(\triangle x)^2} \tag{A.3}$$

- **Backward Difference Scheme:**

$$\left.\frac{\partial f}{\partial x}\right|_{x=x_i} = \frac{f_i - f_{i-1}}{\Delta x} \tag{A.4}$$

$$\left.\frac{\partial^2 f}{\partial x^2}\right|_{x=x_i} = \frac{f_i - 2f_{i-1} + f_{i-2}}{(\triangle x)^2} \tag{A.5}$$

- **Central Difference Scheme:**

$$\left.\frac{\partial f}{\partial x}\right|_{x=x_i} = \frac{f_{i+1} - f_{i-1}}{2\triangle x} \tag{A.6}$$

$$\left.\frac{\partial^2 f}{\partial x^2}\right|_{x=x_i} = \frac{f_{i+1} - 2f_i + f_{i-1}}{(\triangle x)^2} \tag{A.7}$$

In this thesis work, the central difference scheme is used to solve the differential equations. As, the differentials are with respect to time, they can be written as:

$$\left.\frac{\partial f}{\partial t}\right|_{t=t_i} = \frac{f_{i+1} - f_{i-1}}{2\triangle t} \tag{A.8}$$

$$\left.\frac{\partial^2 f}{\partial t^2}\right|_{t=t_i} = \frac{f_{i+1} - 2f_i + f_{i-1}}{(\triangle t)^2} \tag{A.9}$$

where $\triangle t$ is the incremental time step.

A.2 Solution of the Heat Equation

The laser pulse used to generate the photo-carriers in the PCA gap is shown in Fig. A.1, where the gaussian pulse is approximated with the exponential functions. The following assumptions have also been considered to solve the heat equation;

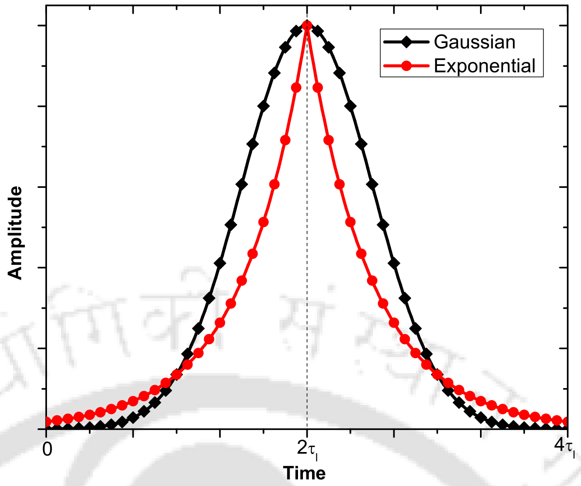

Fig. A.1: Approximation of Gaussian pulse using exponential functions

- The optical absorption and power reflection coefficients of the material are temperature independent.
- The thickness of the semiconductor substrate material is very large compare to the laser beam skin depth.
- A uniform laser illumination at the electrodes gap.

The heat equation in terms of temperature and laser intensity can be written as [173]:

$$\frac{\partial T(y,t)}{\partial t} = \eta \frac{\partial^2 T(y,t)}{\partial y^2} + \frac{\alpha I_T\, e^{-\alpha y}}{\rho c_p} \tag{A.10}$$

where $\eta = \frac{k}{\rho c_p}$, ρ is the density of the material, c_p is the specific heat capacity of the material, k is the thermal conductivity of the material, α is the optical absorption coefficient of the material, and I_T is the laser intensity within the radius r applied at the material surface.

The laser intensity within the radius r including the time variation as shown in Fig. A.1 can be given as:

$$I_T = \begin{cases} A_T\, e^{\frac{2(t-2\tau_l)}{\tau_l}} & \text{for } 0 \le t \le 2\tau_l \\ A_T\, e^{\frac{-2(t-2\tau_l)}{\tau_l}}\, u(t-2\tau_l) & \text{for } 2\tau_l \le t < \infty \end{cases} \tag{A.11}$$

with

$$A_T = \frac{2(1-R)P_0}{\pi \omega_0^2} \left[1 - e^{\left(\frac{-2r^2}{\omega_0^2}\right)} \right] \tag{A.12}$$

where τ_l is the laser pulse width, R is the power reflection coefficient, P_0 is the laser peak power, and ω_0 is the laser beam waist radius.

In order to achieve the closed form solution, the following boundary conditions have been used:

- $T(y,0) = T_0 = 300$ K
- $T(\infty,t) = T_0 = 300$ K
- $\left.\frac{\partial T}{\partial y}\right|_{y=0} = 0$

To solve the heat equation, dividing it into time domain as:

(i) $0 \leq t \leq 2\tau_l$

(ii) $2\tau_l \leq t < \infty$

A.2.1 For 0≤t≤2τ_l

The heat equation for $0 \leq t \leq 2\tau_l$ can be written as:

$$\frac{\partial T(y,t)}{\partial t} = \eta\frac{\partial^2 T(y,t)}{\partial y^2} + \frac{\alpha A_T\, e^{\frac{2(t-2\tau_l)}{\tau_l}}\; e^{-\alpha y}}{\rho c_p} \tag{A.13}$$

Taking the Laplace transform of (A.13) gives:

$$sT(y,s) - T_0 = \eta\frac{\partial^2 T(y,s)}{\partial y^2} + \frac{\alpha A_T\; e^{-4}\; e^{-\alpha y}}{\rho c_p(s-a)} \tag{A.14}$$

where $a = \frac{2}{\tau_l}$

Solving the second order differential equation (A.14) in the spatial domain, using the boundary conditions the solution can be written as:

$$T(y,s) = \frac{\alpha A_T e^{-4}}{\rho c_p}\left[\frac{e^{-\alpha y}}{(s-a)(s-\eta\alpha^2)} - \frac{\alpha\sqrt{\eta}\; e^{-y\sqrt{\frac{s}{\eta}}}}{\sqrt{s}(s-a)(s-\eta\alpha^2)}\right] + \frac{T_0}{s} \tag{A.15}$$

Taking inverse Laplace transform of (A.15) and for $y = 0$ the solution can be written as:

$$T(t) = T_0 + \frac{\alpha A_T e^{-4}}{\rho c_p}\left[\frac{e^{at} - e^{\eta\alpha^2 t}}{a-\eta\alpha^2} - \frac{\alpha\sqrt{\eta}e^{at}\ \mathrm{erf}(\sqrt{at})}{\sqrt{a}(a-\eta\alpha^2)} + \frac{e^{\eta\alpha^2 t}\mathrm{erf}(\alpha\sqrt{\eta t})}{a-\eta\alpha^2}\right] \tag{A.16}$$

The following relations have been used to get the above solution:

$$\mathcal{L}^{-1}\left[\frac{e^{-y\sqrt{\frac{s}{\eta}}}}{\sqrt{s}(s-a)}\right] = \frac{1}{2\sqrt{a}}\left[e^{at-y\sqrt{\frac{a}{\eta}}}\,\mathrm{erfc}\left(\frac{y}{2\sqrt{\eta t}} - \sqrt{at}\right) - e^{at+y\sqrt{\frac{a}{\eta}}}\,\mathrm{erfc}\left(\frac{y}{2\sqrt{\eta t}} + \sqrt{at}\right)\right] \tag{A.17}$$

$$\mathrm{erfc}(-x) = 2 - \mathrm{erfc}(x) \tag{A.18}$$

$$\mathrm{erf}(x) = 1 - \mathrm{erfc}(x) \tag{A.19}$$

A.2.2 For $2\tau_l \leq$t$< \infty$

For this time duration the following boundary conditions are used:

- $T(y, 2\tau_l) = T_{2\tau_l}$
- $T(\infty, t) = T_0 = 300$ K
- $\left.\frac{\partial T}{\partial y}\right|_{y=0} = 0$

The heat equation for $2\tau_l \leq t < \infty$ can be written as:

$$\frac{\partial T(y,t)}{\partial t} = \eta\frac{\partial^2 T(y,t)}{\partial y^2} + \frac{\alpha A_T\, e^{\frac{-2(t-2\tau_l)}{\tau_l}}\; e^{-\alpha y}}{\rho c_p}u(t-2\tau_l) \tag{A.20}$$

Taking the Laplace transform of (A.20) gives:

$$sT(y,s) - T_{2\tau_l} = \eta\frac{\partial^2 T(y,s)}{\partial y^2} + \frac{\alpha A_T\, e^4\, e^{-\alpha y}\, e^{2\tau_l(s+a)}}{\rho c_p(s+a)} \tag{A.21}$$

The solution of (A.21) can be written as:

$$T(y,s) = \frac{\alpha A_T e^4\, e^{2\tau_l(s+a)}}{\rho c_p}\left[\frac{e^{-\alpha y}}{(s+a)(s-\eta\alpha^2)} - \frac{\alpha\sqrt{\eta}\, e^{-y\sqrt{\frac{s}{\eta}}}}{\sqrt{s}(s+a)(s-\eta\alpha^2)}\right] + \frac{T_{2\tau_l}}{s} \tag{A.22}$$

Taking inverse Laplace transform of (A.22) and for $y = 0$ the solution can be written as:

$$\begin{aligned} T(t) = T_{2\tau_l} + \frac{\alpha A_T e^4}{\rho c_p}\Bigg[&\frac{e^{-2a\tau_l+\eta\alpha^2(t-2\tau_l)} - e^{-at}}{a+\eta\alpha^2} - \frac{e^{-2a\tau_l+\eta\alpha^2(t-2\tau_l)}\,\mathrm{erf}(\alpha\sqrt{\eta(t-2\tau_l)})}{a+\eta\alpha^2} \\ &- \frac{\alpha\sqrt{\eta}\, e^{-at}\,\mathrm{erfi}(\sqrt{a(t-2\tau_l)})}{\sqrt{a}(a+\eta\alpha^2)}\Bigg] \end{aligned} \tag{A.23}$$

The following relations have been used to get the above solution:

$$\mathcal{L}^{-1}\left[\frac{e^{-y\sqrt{\frac{s}{\eta}}}\ e^{2\tau_l(s+a)}}{\sqrt{s}(s-\eta\alpha^2)}\right]=\frac{e^{-2a\tau_l}}{2\alpha\sqrt{\eta}}\left[e^{\eta\alpha^2(t-2\tau_l)-\alpha y}\ \mathrm{erfc}\left(\frac{y}{2\sqrt{\eta(t-2\tau_l)}}-\alpha\sqrt{\eta(t-2\tau_l)}\right)\right.$$
$$\left.-e^{\eta\alpha^2(t-2\tau_l)+\alpha y}\ \mathrm{erfc}\left(\frac{y}{2\sqrt{\eta(t-2\tau_l)}}+\alpha\sqrt{\eta(t-2\tau_l)}\right)\right] \tag{A.24}$$

$$\mathcal{L}^{-1}\left[\frac{e^{-y\sqrt{\frac{s}{\eta}}}\ e^{2\tau_l(s+a)}}{\sqrt{s}(s+a)}\right]=\frac{e^{-2a\tau_l}}{2i\sqrt{a}}\left[e^{-a(t-2\tau_l)-iy\sqrt{\frac{a}{\eta}}}\ \mathrm{erfc}\left(\frac{y}{2\sqrt{\eta(t-2\tau_l)}}-i\sqrt{a(t-2\tau_l)}\right)\right.$$
$$\left.-e^{-a(t-2\tau_l)+iy\sqrt{\frac{a}{\eta}}}\ \mathrm{erfc}\left(\frac{y}{2\sqrt{\eta(t-2\tau_l)}}+i\sqrt{a(t-2\tau_l)}\right)\right] \tag{A.25}$$

$$\mathrm{erfc}(ix)=1-\mathrm{erf}(ix) \tag{A.26}$$

$$\mathrm{erfc}(-ix)=1+\mathrm{erf}(ix) \tag{A.27}$$

$$\mathrm{erfi}(x)=-i\ \mathrm{erf}(ix)=i[\mathrm{erfc}(ix)-1] \tag{A.28}$$

So, the complete solution of the heat equation at the surface of the semiconductor material can be written as:

$$T(t)=\begin{cases} T_0+\dfrac{\alpha A_T e^{-4}\tau_l}{\rho c_p}\left[\dfrac{\left(e^{\frac{2t}{\tau_l}}-e^{\eta\alpha^2 t}\right)}{(2-\eta\alpha^2\tau_l)}-\dfrac{\alpha\sqrt{\eta\tau_l}e^{\frac{2t}{\tau_l}}\ \mathrm{erf}\left(\sqrt{\frac{2t}{\tau_l}}\right)}{\sqrt{2}\,(2-\eta\alpha^2\tau_l)}+\dfrac{e^{\eta\alpha^2 t}\ \mathrm{erf}\left(\alpha\sqrt{\eta t}\right)}{(2-\eta\alpha^2\tau_l)}\right] \\ \qquad\qquad\qquad\qquad\qquad\qquad\qquad\qquad \text{for } 0\le t\le 2\tau_l \\ T_{2\tau_l}+\dfrac{\alpha A_T e^{4}\tau_l}{\rho c_p}\left[\dfrac{\left(e^{-4+\eta\alpha^2(t-2\tau_l)}-e^{-\frac{2t}{\tau_l}}\right)}{(2+\eta\alpha^2\tau_l)}-\dfrac{e^{-4+\eta\alpha^2(t-2\tau_l)}\mathrm{erf}\left[\alpha\sqrt{\eta(t-2\tau_l)}\right]}{(2+\eta\alpha^2\tau_l)}\right. \\ \qquad\qquad\qquad \left.+\dfrac{\alpha\sqrt{\eta\tau_l}\ e^{\frac{-2t}{\tau_l}}\ \mathrm{erfi}\left(\sqrt{\frac{2(t-2\tau_l)}{\tau_l}}\right)}{\sqrt{2}\,(2+\eta\alpha^2\tau_l)}\right] \\ \qquad\qquad\qquad\qquad\qquad\qquad\qquad\qquad \text{for } 2\tau_l\le t<\infty \end{cases} \tag{A.29}$$

A.3 Expansion of Eqs. (7.64) and (7.65)

Using (7.40), (7.41), (7.42), (7.44), (7.62), (7.63),(7.64) and (7.65), the radiated magnetic fields from the small aperture and large aperture PCA can be written as:

- **For Small Aperture PCA:**

$$\vec{E}_{THz}(t) = \frac{A}{4\pi\varepsilon_0 y_d c^2}\left\{E_{net}(t)\left[\frac{qn_{av}(t)\mu_n(t)l_n + qp_{av}(t)\mu_p(t)l_p}{\tau_r} + \frac{\zeta\epsilon_0\epsilon_r}{\tau_r^2}\right] - \frac{E_{bias}}{\tau_r^2}\right\}\hat{\theta} \tag{A.30}$$

$$\vec{H}_{THz}(t) = \frac{A}{4\pi y_d c}\left\{E_{net}(t)\left[\frac{qn_{av}(t)\mu_n(t)l_n + qp_{av}(t)\mu_p(t)l_p}{\tau_r} + \frac{\zeta\epsilon_0\epsilon_r}{\tau_r^2}\right] - \frac{E_{bias}}{\tau_r^2}\right\}\hat{\phi} \tag{A.31}$$

- **For Large Aperture PCA:**

$$\begin{aligned}\vec{E}_{THz}(t) = \frac{A}{4\pi\varepsilon_0 y_d c^2}&\Bigg\{\Bigg[\Bigg(\frac{1}{\tau_r} - \frac{\eta_0\zeta\epsilon_0\epsilon_r}{\tau_r^2\left(1+\sqrt{\varepsilon_r}\right)}\Bigg)\\ &\times\frac{qn_{av}(t)\mu_n(t)l_n + qp_{av}(t)\mu_p(t)l_p}{\tau_r} + \frac{\zeta\epsilon_0\epsilon_r}{\tau_r^2}\Bigg]E_{net}(t) - \frac{E_{bias}}{\tau_r^2}\Bigg\}\hat{\theta}\end{aligned} \tag{A.32}$$

$$\begin{aligned}\vec{H}_{THz}(t) = \frac{A}{4\pi y_d c}&\Bigg\{\Bigg[\Bigg(\frac{1}{\tau_r} - \frac{\eta_0\zeta\epsilon_0\epsilon_r}{\tau_r^2\left(1+\sqrt{\varepsilon_r}\right)}\Bigg)\\ &\times\frac{qn_{av}(t)\mu_n(t)l_n + qp_{av}(t)\mu_p(t)l_p}{\tau_r} + \frac{\zeta\epsilon_0\epsilon_r}{\tau_r^2}\Bigg]E_{net}(t) - \frac{E_{bias}}{\tau_r^2}\Bigg\}\hat{\phi}\end{aligned} \tag{A.33}$$

Bibliography

[1] B. Ferguson and X.-C. Zhang, “Materials for terahertz science and technology,” *Nat. Mater.*, vol. 1, no. 1, 2002.

[2] D. Dragoman and M. Dragoman, “Terahertz fields and applications,” *Prog. Quant. Electron.*, vol. 28, pp. 1–66, 2004.

[3] P. H. Siegel, “Terahertz technology,” *IEEE Trans. Microw. Theory Techn.*, vol. 50, no. 3, 2002.

[4] W. L. Chan, J. Deibel, and D. M. Mittleman, “Imaging with terahertz radiation,” *Rep. Prog. Phys.*, vol. 70, no. 8, 2007.

[5] Q. Song, Y. Zhao, A. Redo-Sanchez, C. Zhang, and X. Liu, “Fast continuous terahertz wave imaging system for security,” *Opt. Commun.*, vol. 282, no. 10, 2009.

[6] E. Pickwell and V. Wallace, “Biomedical applications of terahertz technology,” *J Phys D Appl Phys.*, vol. 39, no. 17, 2006.

[7] P. U. Jepsen, D. G. Cooke, and M. Koch, “Terahertz spectroscopy and imaging–modern techniques and applications,” *Laser Photon. Rev.*, vol. 5, no. 1, 2011.

[8] A. Markelz, A. Roitberg, and E. J. Heilweil, “Pulsed terahertz spectroscopy of DNA, bovine serum albumin and collagen between 0.1 and 2.0 THz,” *Chem. Phys. Lett.*, vol. 320, no. 1, 2000.

[9] A. Davies, E. H. Linfield, and M. B. Johnston, “The development of terahertz sources and their applications,” *Phys. Med. Biol*, vol. 47, no. 21, 2002.

[10] P. Mukherjee and B. Gupta, “Terahertz (THz) frequency sources and antennas-A brief review,” *Int J Infrared Millimeter Waves*, vol. 29, no. 12, 2008.

[11] M. Tonouchi, “Cutting-edge terahertz technology,” *Nature Photonics*, vol. 1, 2007.

[12] R. A. Lewis, “A review of terahertz sources,” *J. Phys. D Appl. Phys.*, vol. 47, no. 37, 2014.

[13] F. Lewen, E. Michael, R. Gendriesch, J. Stutzki, and G. Winnewisser, “Terahertz laser sideband spectroscopy with backward wave oscillators,” *J. Mol. Spectrosc.*, vol. 183, no. 1, 1997.

[14] A. Toreev, V. Fedorov, and E. Patrusheva, “Millimeter-wave extended interaction klystron,” *Journal of Communications Technology and Electronics*, vol. 54, no. 8, 2009.

[15] V. Bratman, Y. K. Kalynov, and V. Manuilov, “Large-orbit gyrotron operation in the terahertz frequency range,” *Phys. Rev. Lett.*, vol. 102, no. 24, 2009.

[16] J. Barros, C. Evain, L. Manceron, J.-B. Brubach, M.-A. Tordeux, P. Brunelle, L. Nadolski, A. Loulergue, M.-E. Couprie, S. Bielawski *et al.*, “Coherent synchrotron radiation for broadband terahertz spectroscopy,” *Rev. Sci. Instrum.*, vol. 84, no. 3, 2013.

[17] S. Bhattacharjee, J. H. Booske, C. L. Kory, D. W. Van Der Weide, S. Limbach, S. Gallagher, J. D. Welter, M. R. Lopez, R. M. Gilgenbach, R. L. Ives *et al.*, "Folded waveguide traveling-wave tube sources for terahertz radiation," *IEEE Trans. Plasma Sci.*, vol. 32, no. 3, 2004.

[18] J. H. Booske, R. J. Dobbs, C. D. Joye, C. L. Kory, G. R. Neil, G.-S. Park, J. Park, and R. J. Temkin, "Vacuum electronic high power terahertz sources," *IEEE Trans. THz Sci. Technol.*, vol. 1, no. 1, 2011.

[19] L.-A. Yang, Y. Hao, Q. Yao, and J. Zhang, "Improved negative differential mobility model of GaN and AlGaN for a terahertz Gunn diode," *IEEE Trans. Electron Devices*, vol. 58, no. 4, 2011.

[20] W. Knap, J. Lusakowski, T. Parenty, S. Bollaert, A. Cappy, V. Popov, and M. Shur, "Terahertz emission by plasma waves in 60 nm gate high electron mobility transistors," *Appl. Phys. Lett.*, vol. 84, no. 13, 2004.

[21] A. Maestrini, J. S. Ward, J. J. Gill, C. Lee, B. Thomas, R. H. Lin, G. Chattopadhyay, and I. Mehdi, "A frequency-multiplied source with more than 1 mW of power across the 840–900-GHz band," *IEEE Trans. Microw. Theory Techn.*, vol. 58, no. 7, 2010.

[22] S. Suzuki, M. Asada, A. Teranishi, H. Sugiyama, and H. Yokoyama, "Fundamental oscillation of resonant tunneling diodes above 1 THz at room temperature," *Appl. Phys. Lett.*, vol. 97, no. 24, 2010.

[23] M. Mukherjee, N. Mazumder, S. K. Roy, and K. Goswami, "GaN IMPATT diode: a photosensitive high power terahertz source," *Semicond. Sci. Tech.*, vol. 22, no. 12, 2007.

[24] H. Hamster, A. Sullivan, S. Gordon, W. White, and R. Falcone, "Subpicosecond, electromagnetic pulses from intense laser-plasma interaction," *Phys. Rev. Lett.*, vol. 71, no. 17, 1993.

[25] J. Dai, J. Liu, and X.-C. Zhang, "Terahertz wave air photonics: terahertz wave generation and detection with laser-induced gas plasma," *IEEE J. Sel. Topics Quantum Electron.*, vol. 17, no. 1, 2011.

[26] K. Vijayraghavan, Y. Jiang, M. Jang, A. Jiang, K. Choutagunta, A. Vizbaras, F. Demmerle, G. Boehm, M. C. Amann, and M. A. Belkin, "Broadly tunable terahertz generation in mid-infrared quantum cascade lasers," *Nat. Commun.*, vol. 4, 2013.

[27] C. Walther, M. Fischer, G. Scalari, R. Terazzi, N. Hoyler, and J. Faist, "Quantum cascade lasers operating from 1.2 to 1.6 THz," *Appl. Phys. Lett.*, vol. 91, no. 13, 2007.

[28] W. Shi, Y. J. Ding, and P. G. Schunemann, "Coherent terahertz waves based on difference-frequency generation in an annealed zinc–germanium phosphide crystal: improvements on tuning ranges and peak powers," *Opt. Commun.*, vol. 233, no. 1, 2004.

[29] A. Tomasino, A. Parisi, S. Stivala, P. Livreri, A. Cino, A. Busacca, M. Peccianti, and R. Morandotti, "Wideband THz time domain spectroscopy based on optical rectification and electro-optic sampling," *Sci. Rep.*, vol. 3, 2013.

[30] H. Eisele, "InP Gunn devices for 400–425 GHz," *Electron. Lett.*, vol. 42, no. 6, 2006.

[31] P. Tripathy, M. Mukherjee, and S. Pati, "Photosensitive InP IMPATTs in the THz Regime: Modulation of Frequency-Chirping by Optical Means," *Adv. Sci. Lett.*, vol. 22, no. 2, 2016.

[32] G. Chattopadhyay, E. Schlecht, J. S. Ward, J. J. Gill, H. H. Javadi, F. Maiwald, and I. Mehdi, "An all-solid-state broad-band frequency multiplier chain at 1500 GHz," *IEEE Transactions on Microwave Theory and Techniques*, vol. 52, no. 5, pp. 1538–1547, 2004.

[33] P. H. Siegel, R. P. Smith, M. Graidis, and S. C. Martin, "2.5-THz GaAs monolithic membrane-diode mixer," *IEEE Transactions on Microwave Theory and Techniques*, vol. 47, no. 5, pp. 596–604, 1999.

[34] J. L. Hesler, H. Xu, T. Reck, and T. W. Crowe, "Development and testing of a 2.5 THz Schottky mixer," in *36th International Conference on Infrared, Millimeter and Terahertz Waves (IRMMW-THz), 2011*. IEEE, 2011, pp. 1–2.

[35] A. Maestrini, I. Mehdi, J. V. Siles, J. S. Ward, R. Lin, B. Thomas, C. Lee, J. Gill, G. Chattopadhyay, E. Schlecht *et al.*, "Design and characterization of a room temperature all-solid-state electronic source tunable from 2.48 to 2.75 THz," *IEEE Transactions on Terahertz Science and Technology*, vol. 2, no. 2, pp. 177–185, 2012.

[36] A. Biswas, S. Sinha, A. Acharyya, A. Banerjee, S. Pal, H. Satoh, and H. Inokawa, "1.0 THz GaN IMPATT Source: Effect of Parasitic Series Resistance," *Journal of Infrared, Millimeter, and Terahertz Waves*, pp. 1–21, 2018.

[37] M. Asada and S. Suzuki, "Room-temperature oscillation of resonant tunneling diodes close to 2 THz and their functions for various applications," *J Infrared Millim Terahertz Waves*, vol. 37, no. 12, 2016.

[38] H. Qin, J. Sun, Z. He, X. Li, X. Li, S. Liang, C. Yu, Z. Feng, X. Tu, B. Jin *et al.*, "Heterodyne detection at 216, 432, and 648 GHz based on bilayer graphene field-effect transistor with quasi-optical coupling," *Carbon*, 2017.

[39] X. Mei, W. Yoshida, M. Lange, J. Lee, J. Zhou, P.-H. Liu, K. Leong, A. Zamora, J. Padilla, S. Sarkozy *et al.*, "First demonstration of amplification at 1 THz using 25-nm InP high electron mobility transistor process," *IEEE Electron Device Lett.*, vol. 36, no. 4, 2015.

[40] Z. Luqi, W. Yanyu, G. Guo, X. Jin, W. Wanghe, W. Yuanyuan, D. Chong, J. Xuebing, Z. Guoqing, G. Yubin *et al.*, "An ultra-broadband watt-level terahertz BWO based upon novel sine shape ridge waveguide," *J Phys D Appl Phys.*, vol. 49, no. 23, 2016.

[41] A. Q. Zhao and B. S. Yu, "The Nonlinear Designs and Experiments on a 0.42-THz Second Harmonic Gyrotron With Complex Cavity," *IEEE Trans. Electron Devices*, vol. 64, no. 2, 2017.

[42] D. Wang, G. Wang, J. Wang, S. Li, P. Zeng, and Y. Teng, "A high-order mode extended interaction klystron at 0.34 THz," *Physics of Plasmas*, vol. 24, no. 2, 2017.

[43] L. R. Billa, X. Shi, M. N. Akram, and X. Chen, "Improved Design and Microfabrication of H -Plane and E -Plane Loaded Rectangular Slow-Wave Structure for THz TWT Amplifier," *IEEE Trans. Electron Devices*, vol. 64, no. 5, 2017.

[44] G. Liang, T. Liu, and Q. J. Wang, "Recent developments of terahertz quantum cascade lasers," *IEEE J. Sel. Topics Quantum Electron.*, vol. 23, no. 4, 2017.

[45] D. Yan, Y. Wang, D. Xu, P. Liu, C. Yan, J. Shi, H. Liu, Y. He, L. Tang, J. Feng *et al.*, "High-average-power, high-repetition-rate tunable terahertz difference frequency generation with GaSe crystal pumped by 2 μm dual-wavelength intracavity KTP optical parametric oscillator," *Photonics Research*, vol. 5, no. 2, 2017.

[46] B. J. Kang, I. H. Baek, S.-H. Lee, W. T. Kim, S.-J. Lee, Y. U. Jeong, O.-P. Kwon, and F. Rotermund, "Highly nonlinear organic crystal OHQ-T for efficient ultra-broadband terahertz wave generation beyond 10 THz," *Opt. Express*, vol. 24, no. 10, 2016.

[47] H. Ito and T. Ishibashi, "Photonic Terahertz-Wave Generation Using Slot-Antenna-Integrated Uni-Traveling-Carrier Photodiodes," *IEEE J. Sel. Topics Quantum Electron.*, vol. 23, no. 4, 2017.

[48] N. T. Yardimci, H. Lu, and M. Jarrahi, "High power telecommunication-compatible photoconductive terahertz emitters based on plasmonic nano-antenna arrays," *Appl. Phys. Lett.*, vol. 109, no. 19, 2016.

[49] F. Sizov and A. Rogalski, "THz detectors," *Prog. Quant. Electron.*, vol. 34, no. 5, 2010.

[50] R. Han, Y. Zhang, Y. Kim, D. Y. Kim, H. Shichijo, E. Afshari *et al.*, "Active terahertz imaging using Schottky diodes in CMOS: Array and 860-GHz pixel," *IEEE J. Solid-State Circuits*, vol. 48, no. 10, 2013.

[51] L. Liu, S. M. Rahman, Z. Jiang, W. Li, and P. Fay, "Advanced Terahertz Sensing and Imaging Systems Based on Integrated III-V Interband Tunneling Devices," *Proceedings of the IEEE*, vol. 105, no. 6, 2017.

[52] S. Seliverstov, S. Maslennikov, S. Ryabchun, M. Finkel, T. Klapwijk, N. Kaurova, Y. Vachtomin, K. Smirnov, B. Voronov, and G. Goltsman, "Fast and sensitive terahertz direct detector based on superconducting antenna-coupled hot electron bolometer," *IEEE Trans. Appl. Supercond.*, vol. 25, no. 3, 2015.

[53] L. Jing, W. Ming-Jye, S. Sheng-Cai, and H. Matsuo, "Terahertz Detection with Twin Superconductor-Insulator-Superconductor Tunnel Junctions," *Chin. Phys. Lett.*, vol. 24, no. 2, 2007.

[54] Y. Zhang, X. Zhang, S. Li, J. Gu, Y. Li, Z. Tian, C. Ouyang, M. He, J. Han, and W. Zhang, "A broadband THz-TDS system based on DSTMS emitter and LTG InGaAs/InAlAs photoconductive antenna detector," *Sci. Rep.*, vol. 6, 2016.

[55] H. Hafez, X. Chai, A. Ibrahim, S. Mondal, D. Férachou, X. Ropagnol, and T. Ozaki, "Intense terahertz radiation and their applications," *Journal of Optics*, vol. 18, no. 9, 2016.

[56] X. Yang, X. Zhao, K. Yang, Y. Liu, Y. Liu, W. Fu, and Y. Luo, "Biomedical applications of terahertz spectroscopy and imaging," *Trends Biotechnol.*, vol. 34, no. 10, 2016.

[57] P. H. Siegel, "Terahertz technology in biology and medicine," *IEEE Trans. Microw. Theory Techn*, vol. 52, no. 10, 2004.

[58] T. Löffler, T. Bauer, K. Siebert, H. G. Roskos, A. Fitzgerald, and S. Czasch, "Terahertz dark-field imaging of biomedical tissue," *Opt. Express*, vol. 9, no. 12, 2001.

[59] C. B. Reid, G. Reese, A. P. Gibson, and V. P. Wallace, "Terahertz time-domain spectroscopy of human blood," *IEEE Trans. THz Sci. Technol.*, vol. 3, no. 4, 2013.

[60] M. Stringer, D. Lund, A. Foulds, A. Uddin, E. Berry, R. Miles, and A. Davies, "The analysis of human cortical bone by terahertz time-domain spectroscopy," *Phys. Med. Biol*, vol. 50, no. 14, 2005.

[61] Y.-C. Shen and P. F. Taday, “Development and application of terahertz pulsed imaging for nondestructive inspection of pharmaceutical tablet,” *IEEE J. Sel. Topics Quantum Electron.*, vol. 14, no. 2, 2008.

[62] R. K. May, M. J. Evans, S. Zhong, I. Warr, L. F. Gladden, Y. Shen, and J. A. Zeitler, “Terahertz in-line sensor for direct coating thickness measurement of individual tablets during film coating in real-time,” *J. Pharm. Sci.*, vol. 100, no. 4, 2011.

[63] H. Lin, Y. Dong, D. Markl, B. M. Williams, Y. Zheng, Y. Shen, and J. A. Zeitler, “Measurement of the Intertablet Coating Uniformity of a Pharmaceutical Pan Coating Process With Combined Terahertz and Optical Coherence Tomography In-Line Sensing,” *J. Pharm. Sci.*, vol. 106, no. 4, 2017.

[64] R. K. May, K. Su, L. Han, S. Zhong, J. A. Elliott, L. F. Gladden, M. Evans, Y. Shen, and J. A. Zeitler, “Hardness and density distributions of pharmaceutical tablets measured by terahertz pulsed imaging,” *J. Pharm. Sci.*, vol. 102, no. 7, 2013.

[65] L. Ho, R. Müller, C. Krüger, K. C. Gordon, P. Kleinebudde, M. Pepper, T. Rades, Y. Shen, P. F. Taday, and J. A. Zeitler, “Investigating dissolution performance critical areas on coated tablets: A case study using terahertz pulsed imaging,” *J. Pharm. Sci.*, vol. 99, no. 1, 2010.

[66] P. F. Taday, I. Bradley, D. Arnone, and M. Pepper, “Using terahertz pulse spectroscopy to study the crystalline structure of a drug: A case study of the polymorphs of ranitidine hydrochloride,” *J. Pharm. Sci.*, vol. 92, no. 4, 2003.

[67] W. R. Tribe, D. A. Newnham, P. F. Taday, and M. C. Kemp, “Hidden object detection: security applications of terahertz technology,” in *Proc. of SPIE Vol*, vol. 5354, 2004.

[68] N. Krumbholz, T. Hochrein, N. Vieweg, T. Hasek, K. Kretschmer, M. Bastian, M. Mikulics, and M. Koch, “Monitoring polymeric compounding processes inline with THz time-domain spectroscopy,” *Polymer Testing*, vol. 28, no. 1, 2009.

[69] C. Jansen, S. Wietzke, O. Peters, M. Scheller, N. Vieweg, M. Salhi, N. Krumbholz, C. Jördens, T. Hochrein, and M. Koch, “Terahertz imaging: applications and perspectives,” *Appl. Opt.*, vol. 49, no. 19, 2010.

[70] H.-J. Song and T. Nagatsuma, “Present and future of terahertz communications,” *IEEE Trans. THz Sci. Technol.*, vol. 1, no. 1, 2011.

[71] T. Nagatsuma, G. Ducournau, and C. C. Renaud, “Advances in terahertz communications accelerated by photonics,” *Nature Photonics*, vol. 10, no. 6, 2016.

[72] D. Auston, K. Cheung, and P. Smith, “Picosecond photoconducting Hertzian dipoles,” *Appl. Phys. Lett.*, vol. 45, no. 3, 1984.

[73] D. H. Auston, K. Cheung, J. Valdmanis, and D. Kleinman, “Cherenkov radiation from femtosecond optical pulses in electro-optic media,” *Phys. Rev. Lett.*, vol. 53, no. 16, 1984.

[74] M. Ketchen, D. Grischkowsky, T. Chen, C.-C. Chi, I. Duling Iii, N. Halas, J.-M. Halbout, J. Kash, and G. Li, “Generation of subpicosecond electrical pulses on coplanar transmission lines,” *Appl. Phys. Lett.*, vol. 48, no. 12, 1986.

[75] C. Fattinger and D. Grischkowsky, “Point source terahertz optics,” *Appl. Phys. Lett.*, vol. 53, no. 16, 1988.

[76] M. Tani, S. Matsuura, K. Sakai, and S.-i. Nakashima, "Emission characteristics of photoconductive antennas based on low-temperature-grown GaAs and semi-insulating GaAs," *Appl. Opt.*, vol. 36, no. 30, 1997.

[77] B. Salem, D. Morris, V. Aimez, J. Beerens, J. Beauvais, and D. Houde, "Pulsed photoconductive antenna terahertz sources made on ion-implanted GaAs substrates," *J. Phys. Condens. Matter*, vol. 17, no. 46, 2005.

[78] J. Mangeney and P. Crozat, "Ion-irradiated $In_{0.53}Ga_{0.47}As$ photoconductive antennas for THz generation and detection at 1.55μm wavelength," *Comptes Rendus Physique*, vol. 9, no. 2, 2008.

[79] S. Gupta, J. F. Whitaker, and G. A. Mourou, "Ultrafast carrier dynamics in III-V semiconductors grown by molecular-beam epitaxy at very low substrate temperatures," *IEEE J. Quantum Electron.*, vol. 28, no. 10, 1992.

[80] A. Krotkus, S. Marcinkevicius, J. Jasinski, M. Kaminska, H. Tan, and C. Jagadish, "Picosecond carrier lifetime in GaAs implanted with high doses of As ions: An alternative material to low-temperature GaAs for optoelectronic applications," *Appl. Phys. Lett.*, vol. 66, no. 24, 1995.

[81] P. R. Smith, D. H. Auston, and M. C. Nuss, "Subpicosecond photoconducting dipole antennas," *IEEE J. Quantum Electron.*, vol. 24, no. 2, 1988.

[82] P. Benicewicz, J. Roberts, and A. Taylor, "Scaling of terahertz radiation from large-aperture biased photoconductors," *JOSA B*, vol. 11, no. 12, 1994.

[83] P. Mounaix, M. Tondusson, N. Chimot, J. Mangeney, K. Blary, and J. Lampin, "High emission and detection efficiency of terahertz beam with heavy-ion-irradiated InP material excited at 0.8 μm," *Electron. Lett.*, vol. 42, no. 15, 2006.

[84] O. Imafuji, B. P. Singh, Y. Hirose, Y. Fukushima, and S. Takigawa, "High power subterahertz electromagnetic wave radiation from GaN photoconductive switch," *Appl. Phys. Lett.*, vol. 91, no. 7, 2007.

[85] A. Fekecs, M. Bernier, D. Morris, M. Chicoine, F. Schiettekatte, P. Charette, and R. Arès, "Fabrication of high resistivity cold-implanted InGaAsP photoconductors for efficient pulsed terahertz devices," *Opt. Mater. Express*, vol. 1, no. 7, 2011.

[86] H. Roehle, R. Dietz, H. Hensel, J. Böttcher, H. Künzel, D. Stanze, M. Schell, and B. Sartorius, "Next generation 1.5 μm terahertz antennas: mesa-structuring of InGaAs/InAlAs photoconductive layers," *Opt. Express*, vol. 18, no. 3, 2010.

[87] K. Bertulis, A. Krotkus, G. Aleksejenko, V. Pačebutas, R. Adomavičius, G. Molis, and S. Marcinkevičius, "GaBiAs: A material for optoelectronic terahertz devices," *Appl. Phys. Lett.*, vol. 88, no. 20, 2006.

[88] M. Kaminska, Z. Liliental-Weber, E. Weber, T. George, J. Kortright, F. Smith, B.-Y. Tsaur, and A. Calawa, "Structural properties of As-rich GaAs grown by molecular beam epitaxy at low temperatures," *Applied physics letters*, vol. 54, no. 19, pp. 1881–1883, 1989.

[89] G. Galiev, E. Klimov, M. Grekhov, S. Pushkarev, D. Lavrukhin, and P. Maltsev, "Structural and photoluminescence properties of low-temperature GaAs grown on GaAs (100) and GaAs (111) A substrates," *Semiconductors*, vol. 50, no. 2, pp. 195–203, 2016.

[90] C. L. Von Gabriel, "Investigation of low-temperature-grown GaAs photoconductive antennae for continous-wave and pulsed terahertz generation," Ph.D. dissertation, Uni-Frankfurt. De, 2007.

[91] K. Xie, Z. Huang, and C. Wie, "Deep level studies in MBE GaAs grown at low temperature," *Journal of electronic materials*, vol. 20, no. 8, pp. 553–558, 1991.

[92] K. Zhang and D. Miller, "Electrical properties of low-temperature GaAs grown by molecular beam epitaxy and migration enhanced epitaxy," *Journal of electronic materials*, vol. 22, no. 12, pp. 1433–1436, 1993.

[93] P. Kordoš, A. Förster, J. Betko, M. Morvic, and J. Novák, "Semi-insulating GaAs layers grown by molecular-beam epitaxy," *Applied physics letters*, vol. 67, no. 7, pp. 983–985, 1995.

[94] M. Melloch, N. Otsuka, J. Woodall, A. Warren, and J. Freeouf, "Formation of arsenic precipitates in GaAs buffer layers grown by molecular beam epitaxy at low substrate temperatures," *Applied physics letters*, vol. 57, no. 15, pp. 1531–1533, 1990.

[95] R. Yano, Y. Hirayama, S. Miyashita, N. Uesugi, and S. Uehara, "Arsenic pressure dependence of carrier lifetime and annealing dynamics for low-temperature grown GaAs studied by pump–probe spectroscopy," *Journal of applied physics*, vol. 94, no. 6, pp. 3966–3971, 2003.

[96] P. Specht, S. Jeong, H. Sohn, M. Luysberg, A. Prasad, J. Gebauer, R. Krause-Rehberg, and E. R. Weber, "Defect control in As-rich GaAs," in *Materials Science Forum*, vol. 258. Trans Tech Publ, 1997, pp. 951–956.

[97] D. C. Look, J. Grant, and J. Sizelove, "Shifted x-ray photoelectron peak in molecular beam epitaxial GaAs grown at 200°C," *Applied physics letters*, vol. 61, no. 11, pp. 1329–1331, 1992.

[98] D. C. Look, D. Walters, G. Robinson, J. Sizelove, M. Mier, and C. Stutz, "Annealing dynamics of molecular-beam epitaxial GaAs grown at 200°C," *Journal of applied physics*, vol. 74, no. 1, pp. 306–310, 1993.

[99] M. Manasreh, D. C. Look, K. Evans, and C. Stutz, "Infrared absorption of deep defects in molecular-beam-epitaxial GaAs layers grown at 200°C: Observation of an EL2-like defect," *Physical Review B*, vol. 41, no. 14, p. 10272, 1990.

[100] A. Warren, J. Woodall, P. Kirchner, X. Yin, F. Pollak, M. Melloch, N. Otsuka, and K. Mahalingam, "Role of excess As in low-temperature-grown GaAs," *Physical Review B*, vol. 46, no. 8, p. 4617, 1992.

[101] M. Luysberg, H. Sohn, A. Prasad, P. Specht, Z. Liliental-Weber, E. Weber, J. Gebauer, and R. Krause-Rehberg, "Effects of the growth temperature and As/Ga flux ratio on the incorporation of excess As into low temperature grown GaAs," *Journal of applied physics*, vol. 83, no. 1, pp. 561–566, 1998.

[102] D. C. Look, "Molecular beam epitaxial GaAs grown at low temperatures," *Thin solid films*, vol. 231, no. 1-2, pp. 61–73, 1993.

[103] X. Liu, A. Prasad, W. Chen, A. Kurpiewski, A. Stoschek, Z. Liliental-Weber, and E. Weber, "Mechanism responsible for the semi-insulating properties of low-temperature-grown GaAs," *Applied physics letters*, vol. 65, no. 23, pp. 3002–3004, 1994.

[104] H. Von Bardeleben, M. Manasreh, D. C. Look, K. Evans, and C. Stutz, "Electron-paramagnetic-resonance study of GaAs grown by low-temperature molecular-beam epitaxy," *Physical Review B*, vol. 45, no. 7, p. 3372, 1992.

[105] S. Gupta, M. Frankel, J. Valdmanis, J. F. Whitaker, G. A. Mourou, F. Smith, and A. Calawa, "Subpicosecond carrier lifetime in GaAs grown by molecular beam epitaxy at low temperatures," *Appl. Phys. Lett.*, vol. 59, no. 25, 1991.

[106] S. Prabhu, S. Ralph, M. Melloch, and E. Harmon, "Carrier dynamics of low-temperature-grown GaAs observed via THz spectroscopy," *Appl. Phys. Lett.*, vol. 70, no. 18, 1997.

[107] K. McIntosh, K. Nichols, S. Verghese, and E. Brown, "Investigation of ultrashort photocarrier relaxation times in low-temperature-grown GaAs," *Applied physics letters*, vol. 70, no. 3, pp. 354–356, 1997.

[108] H. Němec, A. Pashkin, P. Kužel, M. Khazan, S. Schnüll, and I. Wilke, "Carrier dynamics in low-temperature grown GaAs studied by terahertz emission spectroscopy," *J. Appl. Phys.*, vol. 90, no. 3, 2001.

[109] E. Harmon, M. Melloch, J. Woodall, D. Nolte, N. Otsuka, and C. Chang, "Carrier lifetime versus anneal in low temperature growth GaAs," *Appl. Phys. Lett.*, vol. 63, no. 16, 1993.

[110] S. Benjamin, H. Loka, A. Othonos, and P. Smith, "Ultrafast dynamics of nonlinear absorption in low-temperature-grown GaAs," *Applied physics letters*, vol. 68, no. 18, pp. 2544–2546, 1996.

[111] J. Luo, H. Thomas, D. Morgan, and D. Westwood, "Transport properties of GaAs layers grown by molecular beam epitaxy at low temperature and the effects of annealing," *Journal of applied physics*, vol. 79, no. 7, pp. 3622–3629, 1996.

[112] D. C. Look, D. Walters, M. Manasreh, J. Sizelove, C. Stutz, and K. Evans, "Anomalous Hall-effect results in low-temperature molecular-beam-epitaxial GaAs: Hopping in a dense EL2-like band," *Physical Review B*, vol. 42, no. 6, p. 3578, 1990.

[113] M. Kaminska and E. R. Weber, "Low temperature GaAs: Electrical and optical properties," in *Materials Science Forum*, vol. 83. Trans Tech Publ, 1992, pp. 1033–1044.

[114] G. Segschneider, F. Jacob, T. Löffler, H. G. Roskos, S. Tautz, P. Kiesel, and G. Döhler, "Free-carrier dynamics in low-temperature-grown GaAs at high excitation densities investigated by time-domain terahertz spectroscopy," *Physical Review B*, vol. 65, no. 12, p. 125205, 2002.

[115] M. C. Beard, G. M. Turner, and C. A. Schmuttenmaer, "Subpicosecond carrier dynamics in low-temperature grown GaAs as measured by time-resolved terahertz spectroscopy," *Journal of Applied Physics*, vol. 90, no. 12, pp. 5915–5923, 2001.

[116] D. C. Look, G. D. Robinson, J. Sizelove, and C. Stutz, "Electrical properties of molecular beam epitaxial GaAs grown at 300-450°C," *Journal of electronic materials*, vol. 22, no. 12, pp. 1425–1428, 1993.

[117] M. Stellmacher, J.-P. Schnell, D. Adam, and J. Nagle, "Photoconductivity investigation of the electron dynamics in GaAs grown at low temperature," *Applied physics letters*, vol. 74, no. 9, pp. 1239–1241, 1999.

[118] J. Zhang, Y. Hong, S. Braunstein, and K. Shore, "Terahertz pulse generation and detection with LT-GaAs photoconductive antenna," *IEE P. Optoelectron.*, vol. 151, no. 2, 2004.

[119] M. Tonouchi, M. Tani, Z. Wang, K. Sakai, M. Hangyo, N. Wada, and Y. Murakami, "Enhanced THz radiation from YBCO thin film bow-tie antennas with hyper-hemispherical MgO lens," *IEEE Trans. Appl. Supercond*, vol. 7, no. 2, 1997.

[120] C. W. Berry and M. Jarrahi, “Terahertz generation using plasmonic photoconductive gratings,” *New J. Phys.*, vol. 14, no. 10, 2012.

[121] C. Berry, N. Wang, M. Hashemi, M. Unlu, and M. Jarrahi, “Significant performance enhancement in photoconductive terahertz optoelectronics by incorporating plasmonic contact electrodes,” *Nat. Commun.*, vol. 4, 2013.

[122] T. Hattori, K. Egawa, S.-i. Ookuma, and T. Itatani, “Intense terahertz pulses from large-aperture antenna with interdigitated electrodes,” *Jpn. J. Appl. Phys.*, vol. 45, no. 4L, 2006.

[123] M. R. Stone, M. Naftaly, R. E. Miles, J. R. Fletcher, and D. P. Steenson, “Electrical and radiation characteristics of semilarge photoconductive terahertz emitters,” *IEEE Trans. Microw. Theory Techn.*, vol. 52, no. 10, 2004.

[124] M. Suzuki and M. Tonouchi, “Fe-implanted InGaAs photoconductive terahertz detectors triggered by 1.56 μm femtosecond optical pulses,” *Appl. Phys. Lett.*, vol. 86, no. 16, 2005.

[125] S. Hughes, M. Tani, and K. Sakai, “Vector analysis of terahertz transients generated by photoconductive antennas in near-and far-field regimes,” *J. Appl. Phys.*, vol. 93, no. 8, 2003.

[126] E. Castro-Camus, J. Lloyd-Hughes, and M. Johnston, “Three-dimensional carrier-dynamics simulation of terahertz emission from photoconductive switches,” *Phys. Rev. B*, vol. 71, no. 19, 2005.

[127] P. Kirawanich, S. J. Yakura, and N. E. Islam, “Study of high-power wideband terahertz-pulse generation using integrated high-speed photoconductive semiconductor switches,” *IEEE Trans. Plasma Sci.*, vol. 37, no. 1, 2009.

[128] E. Moreno, M. Pantoja, F. Ruiz, J. Roldán, and S. García, “On the numerical modeling of terahertz photoconductive antennas,” *J Infrared Millim Terahertz Waves*, vol. 35, no. 5, 2014.

[129] R. Emadi, N. Barani, R. Safian, and A. Z. Nezhad, “Hybrid computational simulation and study of terahertz pulsed photoconductive antennas,” *J Infrared Millim Terahertz Waves*, vol. 37, no. 11, 2016.

[130] G. C. Loata, M. D. Thomson, T. Löffler, and H. G. Roskos, “Radiation field screening in photoconductive antennae studied via pulsed terahertz emission spectroscopy,” *Appl. Phys. Lett.*, vol. 91, no. 23, 2007.

[131] J. Suen, W. Li, Z. Taylor, and E. Brown, “Characterization and modeling of a terahertz photoconductive switch,” *Appl. Phys. Lett.*, vol. 96, no. 14, 2010.

[132] N. Khiabani, Y. Huang, Y.-C. Shen, and S. Boyes, “Theoretical modeling of a photoconductive antenna in a terahertz pulsed system,” *IEEE Trans. Antennas Propag.*, vol. 61, no. 4, 2013.

[133] I. Malhotra, P. Thakur, S. Pandit, K. R. Jha, and G. Singh, “Analytical framework of small-gap photoconductive dipole antenna using equivalent circuit model,” *Optical and Quantum Electronics*, vol. 49, no. 10, p. 334, 2017.

[134] J. T. Darrow, X.-C. Zhang, D. H. Auston, and J. D. Morse, “Saturation properties of large-aperture photoconducting antennas,” *IEEE J. Quantum Electron.*, vol. 28, no. 6, 1992.

[135] S. Rihani, R. Faulks, H. E. Beere, I. Farrer, M. Evans, D. A. Ritchie, and M. Pepper, “Enhanced terahertz emission from a multilayered low temperature grown GaAs structure,” *Appl. Phys. Lett.*, vol. 96, no. 9, 2010.

[136] G. Arjavalingam, Y. Pastol, J.-M. Halbout, and G. V. Kopcsay, “Broad-band microwave measurements with transient radiation from optoelectronically pulsed antennas,” *IEEE Trans. Microw. Theory Techn.*, vol. 38, no. 5, 1990.

[137] S. Lepeshov, A. Gorodetsky, A. Krasnok, E. Rafailov, and P. Belov, “Enhancement of terahertz photoconductive antenna operation by optical nanoantennas,” *Laser & Photonics Reviews*, 2017.

[138] P. Maraghechi and A. Elezzabi, “Enhanced THz radiation emission from plasmonic complementary Sierpinski fractal emitters,” *Opt. Express*, vol. 18, no. 26, 2010.

[139] Y. Liu, S.-G. Park, and A. M. Weiner, “Enhancement of narrow-band terahertz radiation from photoconducting antennas by optical pulse shaping,” *Opt. Lett.*, vol. 21, no. 21, 1996.

[140] C.-K. Lee, Y.-Y. Lin, G.-R. Lin, C.-L. Wu, T.-H. Wu, C.-J. Chuang, and C.-L. Pan, “Pre-chirped pulse excitation enhanced terahertz radiation,” *IEEE Trans. THz Sci. Technol.*, vol. 6, no. 2, 2016.

[141] I. Synopsys and V. Mountain, “Sentaurus device user guide,” *Version Z-2007.03*, 2010.

[142] S. Selberherr, *Analysis and simulation of semiconductor devices.* Springer Science & Business Media, 2012.

[143] W. Shockley and W. Read Jr, “Statistics of the recombinations of holes and electrons,” *Physical review*, vol. 87, no. 5, 1952.

[144] S. M. Sze and K. K. Ng, *Physics of semiconductor devices.* John wiley & sons, 2006.

[145] D. Caughey and R. Thomas, “Carrier mobilities in silicon empirically related to doping and field,” *Proceedings of the IEEE*, vol. 55, no. 12, 1967.

[146] N. D. Arora, J. R. Hauser, and D. J. Roulston, “Electron and hole mobilities in silicon as a function of concentration and temperature,” *IEEE Trans. Electron Devices*, vol. 29, no. 2, 1982.

[147] D. Pons, P. Mooney, and J. Bourgoin, “Energy dependence of deep level introduction in electron irradiated GaAs,” *J. Appl. Phys.*, vol. 51, no. 4, 1980.

[148] D. Pons, A. Mircea, and J. Bourgoin, “An annealing study of electron irradiation-induced defects in GaAs,” *J. Appl. Phys.*, vol. 51, no. 8, 1980.

[149] R. Wallis, A. Zylbersztejn, and J. Besson, “Pressure dependence of the energy levels of irradiation-induced defects in GaAs,” *Appl. Phys. Lett.*, vol. 38, no. 9, 1981.

[150] M. Tani, K.-S. Lee, and X.-C. Zhang, “Detection of terahertz radiation with low-temperature-grown GaAs-based photoconductive antenna using 1.55 μm probe,” *Appl. Phys. Lett.*, vol. 77, no. 9, 2000.

[151] V. A. Godyak, R. B. Piejak, and B. M. Alexandrovich, “Electrical characteristics of parallel-plate RF discharges in argon,” *IEEE Trans. Plasma Sci.*, vol. 19, no. 4, 1991.

[152] J. T. Verdeyen, *Laser electronics.* Prentice Hall,, 1995.

[153] Z. Piao, M. Tani, and K. Sakai, “Carrier dynamics and terahertz radiation in photoconductive antennas,” *Jpn. J. Appl. Phys.*, vol. 39, no. 1R, 2000.

[154] I. Strzalkowski, S. Joshi, and C. Crowell, “Dielectric constant and its temperature dependence for GaAs, CdTe, and ZnSe,” *Appl. Phys. Lett.*, vol. 28, no. 6, 1976.

[155] M. Beaudoin, A. DeVries, S. Johnson, H. Laman, and T. Tiedje, “Optical absorption edge of semi-insulating GaAs and InP at high temperatures,” *Appl. Phys. Lett.*, vol. 70, no. 26, 1997.

[156] B. G. Prevo, E. W. Hon, and O. D. Velev, “Assembly and characterization of colloid-based antireflective coatings on multicrystalline silicon solar cells,” *J. Mater. Chem.*, vol. 17, no. 8, 2007.

[157] J. Yang, F. Luo, T. S. Kao, X. Li, G. W. Ho, J. Teng, X. Luo, and M. Hong, “Design and fabrication of broadband ultralow reflectivity black Si surfaces by laser micro/nanoprocessing,” *Light Sci. Appl.*, vol. 3, no. 7, 2014.

[158] X. Ropagnol, F. Blanchard, T. Ozaki, and M. Reid, “Intense terahertz generation at low frequencies using an interdigitated ZnSe large aperture photoconductive antenna,” *Appl. Phys. Lett.*, vol. 103, no. 16, 2013.

[159] X. Ropagnol, X. Chai, S. M. Raeis-Zadeh, S. Safavi-Naeini, M. Kirouac-Turmel, M. Bouvier, C.-Y. Côté, M. Reid, M. A. Gauthier, and T. Ozaki, “Influence of Gap Size on Intense THz Generation From ZnSe Interdigitated Large Aperture Photoconductive Antennas (October 2016),” *IEEE J. Sel. Topics Quantum Electron.*, vol. 23, no. 4, 2017.

[160] C. A. Balanis, *Advanced engineering electromagnetics*. John Wiley & Sons, 1999.

[161] N. Gorobets and Y. Y. Ovsyannikova, “Wave processes in the near-field zone of large aperture antenna,” in *9th International Kharkiv Symposium on Physics and Engineering of Microwaves, Millimeter and Submillimeter Waves (MSMW)*, 2016, pp. 1–3.

[162] W. Nakwaski, “Effective masses of electrons and heavy holes in GaAs, InAs, A1As and their ternary compounds,” *Physica B: Condensed Matter*, vol. 210, no. 1, 1995.

[163] A. Mitonneau, A. Mircea, G. Martin, and D. Pons, “Electron and hole capture cross-sections at deep centers in gallium arsenide,” *Revue de physique appliquée*, vol. 14, no. 10, 1979.

[164] S.-G. Park, A. Weiner, M. R. Melloch, C. Sider, J. Sider, and A. J. Taylor, “High-power narrow-band terahertz generation using large-aperture photoconductors,” *IEEE J. Quantum Electron.*, vol. 35, no. 8, 1999.

[165] M. S. Shur, *Handbook series on semiconductor parameters*. World Scientific, 1996, vol. 1.

[166] B. R. Bennett, R. A. Soref, and J. A. Del Alamo, “Carrier-induced change in refractive index of InP, GaAs and InGaAsP,” *IEEE J. Quant. Electron.*, vol. 26, no. 1, pp. 113–122, Jan. 1990.

[167] M. Beck, H. Schäfer, G. Klatt, J. Demsar, S. Winnerl, M. Helm, and T. Dekorsy, “Impulsive terahertz radiation with high electric fields from an amplifier-driven large-area photoconductive antenna,” *Opt. Express*, vol. 18, no. 9, 2010.

[168] W. Shi, L. Hou, and X. Wang, “High effective terahertz radiation from semi-insulating-GaAs photoconductive antennas with ohmic contact electrodes,” *J. Appl. Phys.*, vol. 110, no. 2, 2011.

[169] B. Salem, D. Morris, Y. Salissou, V. Aimez, S. Charlebois, M. Chicoine, and F. Schiettekatte, “Terahertz emission properties of arsenic and oxygen ion-implanted GaAs based photoconductive pulsed sources,” *Journal of Vacuum Science & Technology A: Vacuum, Surfaces, and Films*, vol. 24, no. 3, 2006.

[170] M. Tani, K. Yamamoto, E. S. Estacio, C. T. Que, H. Nakajima, M. Hibi, F. Miyamaru, S. Nishizawa, and M. Hangyo, "Photoconductive emission and detection of terahertz pulsed radiation using semiconductors and semiconductor devices," *J Infrared Millim Terahertz Waves*, vol. 33, no. 4, 2012.

[171] O. D. Jefimenko, "Solutions of Maxwell's equations for electric and magnetic fields in arbitrary media," *Am. J. Phys.*, vol. 60, no. 10, 1992.

[172] J. A. Heras, "Radiation fields of a dipole in arbitrary motion," *Am. J. Phys.*, vol. 62, no. 12, 1994.

[173] Afaf M. Abd El-Hameed, "Analytical study of pulsed laser irradiation on some materials used for photovoltaic cells on satellites," *NRIAG Journal of Astronomy and Geophysics*, vol. 4, pp. 256–265, Oct. 2015.

[174] L. Hou and W. Shi, "An LT-GaAs terahertz photoconductive antenna with high emission power, low noise, and good stability," *IEEE Trans. Electron Devices*, vol. 60, no. 5, 2013.

[175] V. Pačebutas, A. Bičiūnas, S. Balakauskas, A. Krotkus, G. Andriukaitis, D. Lorenc, A. Pugžlys, and A. Baltuška, "Terahertz time-domain-spectroscopy system based on femtosecond Yb: fiber laser and GaBiAs photoconducting components," *Appl. Phys. Lett.*, vol. 97, no. 3, 2010.

[176] Matthew N. O. Sadiku, *Numerical Techniques in Electromagnetics with Matlab.* CRC Press, 2011.